UC Santa Barbara
UC Santa Barbara Electronic Theses and Dissertations

Title
MOCVD Emitter Regrowth Technology for Scaling InGaAs/InP HBTs to Sub-100nm Emitter Width

Permalink
https://escholarship.org/uc/item/61p442zf

Author
Choudhary, Prateek

Publication Date
2015

Peer reviewed|Thesis/dissertation

eScholarship.org Powered by the California Digital Library
University of California

UNIVERSITY of CALIFORNIA
Santa Barbara

MOCVD Emitter Regrowth Technology for Scaling InGaAs/InP HBTs to Sub-100nm Emitter Width

A Dissertation submitted in partial satisfaction
of the requirements for the degree

Doctor of Philosophy
in
Electrical and Computer Engineering

by

Prateek Choudhary

Committee in Charge:

Professor Mark J. W. Rodwell, Chair
Professor John E. Bowers
Professor Umesh K. Mishra
Professor Chris Palmstrom

March 2016

The Dissertation of Prateek Choudhary is approved.

Professor John E. Bowers

Professor Umesh K. Mishra

Professor Chris Palmstrom

Professor Mark J. W. Rodwell, Committee Chair

November 2015

MOCVD Emitter Regrowth Technology for Scaling InGaAs/InP HBTs to Sub-100nm Emitter Width

Copyright © 2016

by

Prateek Choudhary

Dedicated to my family who showed me:

There is no spoon.

To Shivira for her patience and support.

To Chris & Bugra: This PhD would not have been fun without them.

To Mrs. Alinda Holla: She encouraged me when it mattered most.

Curriculum Vitæ

Prateek Choudhary

Personal

Dec. 1987 — Born in Sundergarh, Orissa, India.

Education

2015	Ph.D. in Electrical and Computer Engineering, University of California, Santa Barbara.
2012	M.S. in Electrical and Computer Engineering, University of California, Santa Barbara .
2010	B.S. in Electrical and Computer Engineering, University of Texas at Austin.
2010	B.S. in Physics (Departmental Honors), University of Texas at Austin.

Awards

2013-2014	IBM PhD Fellowship.
2009	Best Student Poster Presentation, University of Texas at Austin Physics Open House.
2009	NASA Group Achievement Award - "For outstanding contributions to the US SHARAD radar sounder processing, analysis and visualization capabilities".
2009-2010	National Instruments Endowed Scholarship for Excellence.

Publications

[1] **P Choudhary**, C-Y Huang, JC Rode, HW Chiang, MJW Rodwell, Sub-Micron InGaAs/InP DHBTs using MOCVD Selective Emitter Regrowth with DC Current Gain of 28, *in progress for IEEE Electron Device Trans. (2015)*

[2] **P. Choudhary**, J.W. Holt, S. Kempf, D. Young, Modeling and analysis of surface topographic effects on the orbital radar sounding of Mars, *in preparation for IEEE Geoscience and Remote Sensing (2016)*

[3] **P Choudhary**, C-Y Huang, JC Rode, HW Chiang, MJW Rodwell, InGaAs/InP DHBTs using MOCVD Selective Emitter Regrowth, Indium Phosphide and Related Materials (2015)

[4] C-Y Huang, **P Choudhary**, S Lee, S Kraemer MJW Rodwell, 12 nm-gate-length ultrathin-body InGaAs/InAs MOSFETs with 8.3*105 Ion/Off, Device Research Conference (2015)

[5] JC Rode, HW Chiang, **P Choudhary**, V Jain MJW Rodwell, Indium Phosphide Heterobipolar Transistor Technology Beyond 1-THz Bandwidth, IEEE Electron Devices Transactions, Vol PP, Issue 99 (2015)

[6] JC Rode, HW Chiang, **P Choudhary**, V Jain MJW Rodwell, An InGaAs/InP DHBT with simultaneous ft/fmax 404/901 GHz and 4.3V breakdown voltage, IEEE Electron Devices Society, Vol 3, Issue 1 (2014)

[7] HW Chiang, JC Rode, **P Choudhary**, MJW Rodwell, Lateral carrier diffusion and current gain in THz InGaAs/InP DHBTs, J. Appl Physics, 115 (2014)

[8] H-W Chiang, J Rode, **P Choudhary**, MJW Rodwell, Surface transport and DC current gain in InGaAs/InP HBTs DHBTs for THz applications, Device Research Conference (2014)

[9] MJW Rodwell, S Lee, C-Y Huang, D Elias, V Chobpattanna, J Rode, H-W Chiang, **P Choudhary**, R Maurer, M Urteaga, B Brar, AC Gossard, S Stemmer, Nanometer InP electron devices for VLSI and THz applications, Device Research Conference (2014)

[10] M.J. Rodwell, J. Rode, H. Chiang, **P Choudhary**, T. Reed, E. Bloch, S. Daneshgar, B. Brar, H. Park, A.C. Goassard, B. Thibeault, W. Mitchell, M. Urteaga, Z. Griffith, J. Hacker, M. Seo, THz Indium Phosphide Bipolar Transistor Technology, Compound Semiconductor IC Symposium (2012)

[11] J.J. Plaut, J.W. Holt, J. W. Head, Y. Gim, **P Choudhary**, D. M. Baker, A. Kress, and the SHARAD Team, Thick ice deposits in deuteronilus mensae, mars: regional distribution from radar sounding., Lunar and Planetary Science Conference (2010)

[12] S. Christian, J.W. Holt, **P Choudhary**, K. Fishbaugh, Correlating high resolution radar reflectors with visible layering of the northern polar layered deposits, Mars, Lunar and Planetary Science Conference (2010)

[13] I.B. Smith, J. W. Holt, D. Mohrig, W. Kim, **P Choudhary**, Quantitative Radar Stratigraphy of the Uppermost North Polar Layered Deposits, Mars, and Processes Controlling Spiral Trough Migration, Lunar and Planetary Science Conference (2010)

[14] N.B. Karlsson, J.W. Holt, R.C.A Hindmarsh, **P Choudhary**, Internal Layering of Gemina Lingula, North Polar Layered Deposits, Mars, and the Case for Ice Flow, Lunar and Planetary Science Conference (2010)

[15] T.C. Brothers, J.W. Holt, S. Christian, **P Choudhary**, Investigating Subsurface Geomorphology of the Basal Unit of Planum Boreum, Mars with SHARAD to Constrain Early Erosional Processes, Lunar and Planetary Science Conference (2010)

[16] J.W. Holt, A. Safaeinili, J.J. Plaut, J.W. Head, R.J. Phillips, R. Seu, S.D. Kempf, **P Choudhary**, D.A. Young, N.E. Putzig, D. Biccari, and Y. Gim, Radar Sounding Evidence for Buried Glaciers in the Southern Mid-Latitudes of Mars, Science, vol. 322 (2008)

Abstract

MOCVD Emitter Regrowth Technology for Scaling InGaAs/InP HBTs to
Sub-100nm Emitter Width

by

Prateek Choudhary

By scaling semiconductor thicknesses, lithographic dimensions, and contact resistivities, the bandwidth of InGaAs/InP Hetero-junction Bipolar Transistors (HBTs) has reached 550/1100 GHz $f_{\mathrm{t}}/f_{\mathrm{max}}$ at 128 nm emitter width (w_{E}). Primary challenges faced in scaling the emitter width are: developing high aspect ratio emitter metal process for $w_{\mathrm{E}} < 100nm$, reducing base contact resistivity $\rho_{\mathrm{b,c}}$, and maintaining high DC current gain β.

The existing W/TiW emitter process for RF HBTs cannot scale below 100 nm. Process modules for scaling the emitter width to 60 nm are demonstrated. High aspect ratio trenches are etched into a sacrificial Si layer and then filled with metal via Atomic Layer Deposition (ALD). Metals with high melting points are chosen to withstand high emitter current densities (J_{E}) at elevated junction temperatures without suffering from electromigration or thermal decomposition and is thus manufacturable. ALD deposition of TiN, Pt, and Ru are explored.

Novel base epi designs are proposed for reducing Auger recombination current ($I_{\mathrm{B,Auger}}$). A dual doping layer in the base is proposed with a higher doping in the upper 5 nm of the base for lower $\rho_{\mathrm{b,c}}$ and a lower doping in the remainder of the base for reducing $I_{\mathrm{B,Auger}}$. Presence of a quasi-electric field ($\triangle E_{\mathrm{C}}$) in the upper

doping grade accelerates electrons away from the region towards the collector, thus further reducing $I_{\mathrm{B,Auger}}$.

Selective regrowth of the emitter semiconductor via Metal-Organic Chemical Vapour Deposition (MOCVD) is proposed for decoupling the extrinsic base region under the base metal from the intrinsic region under the emitter-base junction, for increasing β,f_{t}, and improving $\rho_{\mathrm{b,c}}$. Carbon p-dopants in the InGaAs base are passivated by H^+ during regrowth. Annealing to reactivate carbon induces surface damage and increases base sheet resistance ($R_{\mathrm{b,sh}}$) and $\rho_{\mathrm{b,c}}$. Process techniques for minimizing $R_{\mathrm{b,sh}}$ and $\rho_{\mathrm{b,c}}$ in an emitter regrowth process are demonstrated and compared. $\rho_{\mathrm{b,c}}$ of 5.5 $\Omega.\mu m^2$ on p-InGaAs is demonstrated on Transmission Line Measurement (TLM) structures after regrowth and anneal, by protecting the semiconductor surface with tungsten. This is comparable to 2.9 $\Omega.\mu m^2$ measured on TLM structures that do not undergo regrowth and anneal.

Feasibility of emitter regrowth is demonstrated on Large Area Devices (LADs) with SiO_2 as regrowth mask, and W cap during anneal. Emitter-regrowth and non-regrowth devices of identical dimensions and epi design are compared. Emitter-regrown HBTs yield higher β of 28 as compared to 13 for non-regrowth devices. Benefits of emitter regrowth cannot be ascertained on LADs due to high series resistance and large gap spacings between base metal and emitter-base junction.

A process flow is proposed for scaling regrown HBTs to 60 nm emitter widths. The process incorporates ALD emitter metal technology that is demonstrated in the first half of the dissertation. New epi designs for regrown-emitter HBTs are optimized for maximizing β, f_{t}. Scaling regrown-emitter HBTs is essential for realizing their benefit over non-regrowth HBTs.

Contents

Curriculum Vitæ **v**
. . . . v

Abstract **viii**

List of Tables **xiii**

List of Figures **xv**

1 Introduction **1**
References 5

2 HBT Theory **7**
2.1 Device Structure 7
2.1.1 Principle of Operation 7
2.1.2 HBT Emitter Design 11
2.1.3 HBT Base Design 15
2.1.4 HBT Collector Design 17
2.1.5 HBT Equivalent Circuit Model 19
2.2 HBT RF Performance and Scaling 21
2.3 DC Current Gain β 23
2.3.1 Schockley-Read-Hall and Radiative Recombination Current (I_{SRH},I_{rad}) 25
2.3.2 Auger Recombination Current (I_{Auger}) 25
2.3.3 Lateral Diffusion Current (I_{Diff}) 27
2.3.4 Surface Recombination and Conduction Current ($I_{\mathrm{srf,rec}}$, $I_{\mathrm{srf,cond}}$) 28
2.3.5 DC Current Gain β with HBT Scaling 29
2.4 Base Contact Technology 29

2.4.1 Lift-Off Pt/Ti/Pd/Au Contacts . . . 30
2.4.2 Refractory Metal Contacts . . . 30
2.4.3 Blanket Pt/Ru Metal Contacts . . . 32
References . . . 34

3 RF HBT Improvements **37**
3.1 Reducing Thermal Shock For Improved Yield . . . 37
3.2 Blanket Iridium Base Contacts . . . 39
3.3 Epitaxial Design For $J_{\mathrm{E}} > 40mA/\mu m^2$ . . . 41
3.4 Reducing Auger Recombination . . . 43
3.5 Atomic Layer Deposition of Emitter Metal . . . 44
3.5.1 ALD Emitter Challenges . . . 47
3.5.2 ALD Emitter Preliminary Results . . . 53
References . . . 54

4 MOCVD Emitter Regrowth **56**
4.1 Device Structure . . . 56
4.2 Base Diffusion Current ($I_{\mathrm{b,diff}}$) Suppression . . . 59
4.3 Reduction Of Auger Recombination In The Base . . . 60
4.4 Increase in f_{t} . . . 60
4.5 Regrowth as a Viable Technology . . . 61
4.6 Self-Aligned Emitter Regrowth HBT Process . . . 64
References . . . 67

5 Experimental Results and Analysis **69**
5.1 Carbon Passivation of p-InGaAs Base . . . 69
5.2 Large Area Device HBT Emitter Regrowth Process . . . 71
5.3 HBT 68Q4 - Oxide Protective Cap . . . 73
5.3.1 Device Structure and Process Feature . . . 73
5.3.2 TEM Analysis . . . 74
5.3.3 DC Characteristics . . . 75
5.4 Ohmic Contacts To p-InGaAs After Regrowth . . . 77
5.5 Buried W as Regrowth Mask . . . 79
5.6 HBT 70R4 - InP Protective Cap . . . 82
5.6.1 Device Structure and Process Feature . . . 82
5.6.2 TEM Analysis . . . 84
5.6.3 Issues and Improvements . . . 85
5.7 HBT 74 Q4 - W Annealing Cap . . . 87
5.7.1 Device Structure and Process Feature . . . 87
5.7.2 TEM Analysis . . . 89

5.7.3 Transistor DC Characteristics 91
5.8 W Base Contact Yield 93
References 96

6 Conclusion **97**
6.1 Accomplishments 97
6.1.1 Improving RF HBT Design and Process 97
6.1.2 Process Development For $W_{\mathrm{E}} < 100nm$ 99
6.1.3 MOCVD Selective Emitter Regrowth of HBT LADs 100
6.2 Future Work 101
6.2.1 Alternate Base Contact Technologies 101
6.2.2 Pulse InP Regrowth Cap 102
6.2.3 Epitaxial Design For Emitter Regrowth 103
6.2.4 Scaling HBTs for RF Performance 104
References 105

A HBT 64 Equivalent Circuit Model **106**
References 108

B UCSB W/TiW Emitter Metal Process **109**
References 111

List of Tables

2.1 Typical emitter epi design of an RF HBT at w_{E} of 100nm. 11
2.2 Typical base epi design of an RF HBT at w_{E} of 100nm. 15
2.3 Typical collector epi design of an RF HBT at w_{E} of 100nm. 18
2.4 Scaling laws of HBTs: the required change for improving f_τ and $f_{\max}$ by a factor of γ. 22
2.5 Scaling effect on base current components, as a function of parameter scaling for an increase in f_τ and $f_{\max}$ by a factor of γ. No current spreading in the base, and a uniformly doped base is assumed. . . 29

3.1 Optimized emitter epi design for J_{E} of 50 mA/μm^2 43

4.1 Potential epi design of the extrinsic and intrinsic base in an RF HBT with regrown emitter. 58
4.2 Energy barrier and quasi-electric field $\vec{\varepsilon}_{\mathrm{Quasi}}$ that suppress $I_{\mathrm{b,diff}}$ in each of the proposed regrowth base designs. 60
4.3 Base access resistance comparison for the proposed regrowth designs, compared with a non-regrowth device HBT 64C fabricated at UCSB with a 20nm base [2]. Emitter width of 100 nm is assumed 61

5.1 Hall hole carrier concentration of p-InGaAs films after various processing and anneal conditions. 70
5.2 Epitaxial structure of HBT 68. The emitter-base junction is formed at the Emitter-Intrinsic base interface, and the extrinsic base lies on either side of this junction, on top of the intrinsic base. 73
5.3 Measured contact resistivity to p-InGaAs on TLM test structures for various process samples. Hall carrier concentration of $1{*}10^2 cm^{-3}$ was measured on all samples before processing. Samples A and B indicate that SiO_2 is an insufficient cap and damages the surface. 79

5.4 Epitaxial structure of HBT 70. The emitter-base junction is formed at the Emitter-Intrinsic base interface, and the extrinsic base lies on either side of this junction, on top of the intrinsic base. 83
5.5 Epitaxial structure of HBT74. The emitter-base junction is formed at the Emitter-Intrinsic base interface, and the extrinsic base lies on either side of this junction, on top of the intrinsic base. 88

6.1 Proposed epitaxial structure of RF HBT with emitter regrowth. The emitter-base junction is formed at the emitter-intrinsic base interface, and the extrinsic base lies on either side of this junction, on top of the intrinsic base. 104

A.1 Epitaxial structure of HBT 64. 106

List of Figures

2.1 A simplified schematic of a BJT is shown on the left. The corresponding band diagram is shown on the right with the fermi level E_{F}, conduction band E_{C}, and valence band E_{V} labeled accordingly. 8
2.2 Band diagram of a BJT in forward-active mode illustrating majority carrier drift-diffusion. 9
2.3 Band diagram of an abrupt InP/InGaAs HBT in forward-active mode. There exists a diffusion barrier $\triangle E_{\mathrm{V}}$ for holes diffusing from base to emitter. 11
2.4 Band diagram of a graded InP/InGaAs HBT in forward-active mode with the space charge region in the emitter graded from InP to InGaAs. The diffusion barrier is now $\triangle E_{\mathrm{G}}$ for holes diffusing from base to emitter. 12
2.5 Cross-sectional schematic of a UCSB RF HBT. 13
2.6 Cross-sectional TEM image of a UCSB RF HBT. 14
2.7 Band diagram of the emitter region at increasing emitter-base biases. Emitter starvation occurs at sufficiently high J_{E} [1]. 15
2.8 Cross-sectional schematic of distributed RC network in the base-collector region of an HBT. The device is symmetric along the dashed line i.e. only one side of the device is shown. 17
2.9 Hybrid-π equivalent circuit model of a BJT. 20
2.10 Scaling roadmap for InP/InGaAs HBTs [15] 22
2.11 HBT DC current gain β plotted as a function of emitter perimeter/area. Experimental and simulated data points show a drop in β as the emitter width is reduced. [16] 23
2.12 A cross-sectional schematic of an HBT that shows the various base current components. 24

2.13 The three band-to-band Auger processes are shown. The electrons are represented by closed circles and holes by open circles. Arrows indicate electrons transitions [20]. 26
2.14 A cross-sectional TEM image shows the Pt/Ti/Au base contact sinking into the p-InGaAs base. [16]. 31
2.15 A cross-sectional TEM image shows the Ru/Ti/Au base contact with no discernible metal sinking. [7]. 32
2.16 A cross-sectional TEM image shows the Pt/Ru/Ti/Au base contact. The metal sinking depth has been reduced compared to lifted-off base contact technology [7]. 33

3.1 A cross-sectional TEM image of HBT61B. The semiconductor at the InP/InGaAs emitter-base boundary is cracked due to strain. *(Courtesy: Han-Wei Chiang)* 38
3.2 Process flow incorporating the low temperature SiN anchor to provide structural stability. Steps (c) and (f) introduce strain on the high aspect ratio emitter metal as BCB and InP/W have different coefficients of thermal expansion. 39
3.3 Angled SEM image of sample after Ir dry etch. The W/TiW emitter metal has been etched due to insufficient protection during the etch. (a) Emitter (b) Vernier test structures. 40
3.4 Cross-sectional SEM image of test HBT structure after Ir dry etch. The Al_2O_3/SiN composite sidewall protects the W/TiW emitter metal. 41
3.5 Calculated J_{E} as a function of electron Fermi Level (E_{fn}) position relative to conduction band edge (E_{C}) for InP emitter for Boltzmann approximation, FermiDirac distribution function and including a non-zero electron flux reflectance at the heterointerface [10] 42
3.6 (Left) Pulse layer + doping grade profile in the base for low $R_{\mathrm{Base,cont.}}$ [5]. (Right) Dual doping grade profile in the base maintains high doping under base contact for low $R_{\mathrm{Base,cont.}}$, but also introduces $\triangle E_{\mathrm{C}}$ in high doping regions to accelerate electrons away and reduce Auger recombination. 45
3.7 Auger recombination for dual doping grade and pulse doping base designs, plotted as a function of base depth. 46
3.8 Schematics of 256, 128, and 64nm wide emitter metal stacks after emitter metal dry etch. [12] 47
3.9 Process flow for fabricating emitter metal via ALD deposition. HBT fabrication steps after (g) are identical to W/TiW emitter HBT process flow shown in Appendix B. 48

3.10 Cross-sectional SEM images of Si trenches on the same die. The etch rate/depth decreases as the trench width shrinks due to loading effects. 49
3.11 Cross-sectional SEM images of Si trenches that bows outwards in the middle. This leads to a hollow 'teardrop' when ALD TiN is deposited. The deposited TiN film thickness in the trench is nearly half of the thickness in the field. 50
3.12 Cross-sectional SEM images of 70nm wide high aspect ratio Si trenches. 50
3.13 Cross-sectional SEM images Si trenches after blanket ALD TiN deposition. (a) TiN deposition rate inside the trench is lower due to large precursor mean free path. (b) Complete fill-in due to dose and soak process. 51
3.14 Angled SEM image of Pt emitter after blanket Si etch. The emitter region exposed to Si etch has been attacked. 52
3.15 Angled SEM image an ALD Emitter based HBT after device isolation. The base post (BP), collector contact (CC), base contact (BC), and emitter metal are marked. 53

4.1 Cross-sectional schematic of an emitter regrowth structure. 57
4.2 Simplified distributed RC network in the base-collector region. The base gap resistance is a function of the intrinsic as well as extrinsic base sheet resistance. 58
4.3 (a) Electrons scatter at the base-emitter junction and diffuse towards the base metal in the direction XX'. (b) Band diagram shows that electrons diffusing from emitter-base junction -at energy E_{inj}- encounter an energy barrier $\triangle E_{\mathrm{B}}$ in diffusing towards the base metal, thus reducing $I_{\mathrm{B,diff}}$. 59
4.4 Process flow for fabricating emitter regrowth HBTs with a self-aligned emitter metal deposited via ALD. HBT fabrication steps after (g) are identical to W/TiW emitter HBT process flow shown in Appendix B. 65

5.1 Process flow for a Large Area Device (LAD) HBT with emitter regrowth. Steps after (i) are identical to RF HBT process in Appendix B. 72
5.2 Cross-sectional TEM image of HBT 68Q4 and a close-up of the emitter-base interface. It can be seen that the emitter semiconductor does not contact the extrinsic base. 74

5.3 Cross-sectional TEM of the base surface and base contact of HBT 68Q4. The base surface is damaged. 75
5.4 HBT 68Q4 Emitter-Base and Base-Collector diode I-V characteristics. 76
5.5 HBT 68Q4 gummel curve at zero base-collector bias. Collector leakage current I_C at low V_{BE} is due to extremely high R_{bb} 76
5.6 TLM split to determine source of base surface damage. 78
5.7 Cross-sectional SEM of a regrowth window after the buried W has been wet-etched using AZ300MiF. The undercut is visible at the trench corner. The extrinsic base is then digitally etched and the emitter is regrown. 80
5.8 Cross-sectional SEM image of regrowth trench post regrowth. There is growth nucleation in select areas of the window only. This suggests presence of a residual layer at the surface that is inhibiting growth. 81
5.9 Cross-sectional SEM image of buried W regrowth after additional CF_4/O_2 descum. The regrowth morphology is rough and there is voiding in the InGaAs base. 81
5.10 Process flow for emitter regrowth HBT LAD that incorporates an InP cap above the base for minimizing surface damage before base contact metal deposition. The process after (d) is identical to Figure 5.1, except that the W/Ti/Au base metal is deposited prior to ALD oxide and anneal. 83
5.11 Cross-sectional TEM image of HBT70R4. 85
5.12 Cross-sectional TEM image of the emitter regrowth in HBT70R4. The emitter semiconductor has been etched away during the InP cap wet etch. 86
5.13 Cross-sectional TEM image of HBT74Q4. 89
5.14 Cross-sectional TEM image of the base mesa region of HBT74Q4. There is voiding in the base where W/Ti/Au is present on the surface. 90
5.15 Cross-sectional SEM image of the base region after annealing with a W/SiO_2 cap (left) and a W/Ti/Au/SiO_2 cap(right). The p-InGaAs shows voids if Ti/Au is present. 90
5.16 HBT 74Q4 and HBT 74Q1 emitter-base diode characteristics. HBT 74Q1 devices show large variation in R_{par}. Shunt between emitter-base metal is suspected. 92
5.17 HBT 74Q4 and HBT 74Q1 base-collector diode characteristics. HBT74Q1 has high R_{series}. Sub-collector surface contamination prior to contact metal deposition is suspected. 93

5.18 HBT74Q4 and HBT74Q1 gummel curves. The regrown-emitter HBT (74Q4) shows higher β of 28 as compared to 13 for 74Q1, at V_{CB}=0. It is unclear if this is due to higher $R_{\text{BE,series}}$ and lower $R_{\text{BC,series}}$. 94
5.19 HBT 74Q4 and HBT 74Q1 common-emitter characteristics.. . . . 94
5.20 Inverse DC current gain ($1/\beta$) vs HBT emitter periphery to area ration ($P_{\text{jE}}/A_{\text{jE}}$ of HBT 74Q4. 95

A.1 Equivalent circuit model of HBT 64C. $A_{\text{E}} = 0.22\times2.9\ \mu m^2$ 107

B.1 Flow chart for HBT fabrication with blanket W/TiW emitter process [3] 110

Chapter 1

Introduction

InP/InGaAs heterojunction bipolar transistors (HBTs) today exhibit higher bandwidth than RF CMOS, HEMTs, Si/SiGe HBTs, and InGaP/GaAs HBTs at a given lithographic feature size. The electron transit time in HBTs is largely governed by epitaxial thickness since it is a vertical device. Due to this, HBTs deliver high linearity, power-added-efficiency and breakdown simultaneously while delivering high output power [1] [2].

The demand for high frequency transistors is fueled by sub-mm wave radio systems [3], high frequency communication systems [4], and high resolution radar/imaging systems [5] [6]. The unity current and power gain cutoff frequency ($f_{\mathrm{t}}, f_{\mathrm{max}}$) of HBTs has improved rapidly over the years [7] [8]. The fastest HBTs reported to date have $f_{\mathrm{t}}/f_{\mathrm{max}} > 0.52/1.1$ THz at the 130 nm Emitter width [9]. This is exceeded only by InP HEMTs at 25 nm gate length with $f_{\mathrm{t}}/f_{\mathrm{max}} > 0.76/1.42 THz$ [10] [11], though InP DHBTs have demonstrated higher open-circuit breakdown voltage [12].

In InP/InGaAs HBT, electrons emitted from the InP emitter travel through a thin InGaAs base ($w_{\mathrm{Base}} \ll \lambda_{\mathrm{e}}$) at high velocities due to a low electron effective mass (InGaAs: $0.045m_0$). Electron velocity through the InP collector is in excess of their Fermi velocity due to large Γ-L valley separation in the InP conduction band [13]. The band alignment at the InP-InGaAs emitter-base allows for the base doping to be $> 1 * 10^{20} cm^{-3}$. Cutoff frequency of HBTs is increased by reducing the base-collector epitaxial thicknesses to reduce transit delays, and lithographic reduction of the emitter and base-collector junction width. Parasitic resistances, drive current, and transconductance must be maintained as the device is scaled.

In scaling HBTs to emitter widths ≈130 nm, the primary challenges faced are in developing process flows for high aspect ratio emitter metal [14], reducing base contact resistivity $\rho_{\mathrm{b,c}}$ [15], and maintaining high DC current gain β [16].

The focus of this dissertation is twofold: To provide a manufacturable process for further lithographic shrinking of the emitter width for higher RF performance, and to develop methods to increase DC current gain β as the emitter width reduces.

Process modules for scaling the emitter width to 60 nm are demonstrated. Instead of etching high aspect ratio emitter metal pillars out of a blanket sputtered film [14], a trench is etched into a sacrificial Si layer and is filled with metal via ALD similar to CVD W filling of vias [18]. The process is designed to withstand high emitter current densities (J_{E}) at elevated junction temperatures without suffering from electromigration or thermal decomposition and is thus manufacturable.

MOCVD regrowth of the emitter semiconductor is proposed for decoupling

the extrinsic base region under the base metal from the intrinsic region under the emitter-base junction, for increasing β, f_t, and $\rho_{b,c}$. Emitter regrowth of InP/InGaAs HBTs is demonstrated on Large Area Devices (LADs), and a maximum β of 28 is observed on LADs of emitter area 0.8x4μm^2. A process flow is proposed for scaling regrown HBTs to < 100 nm emitter widths. The process incorporates the ALD emitter technology that is demonstrated in the first half of the dissertation.

Chapter 2 discusses the theory behind HBT design and scaling for increasing RF performance. Reasons for decrease in DC current gain β with emitter scaling, and existing challenges with current base contact technology are explained. Chapter 3 describes the designs and processes that were developed for improving RF HBT yield and base contact technology, and increasing emitter current density J_E. An ALD metal based emitter technology process module is proposed and 60nm wide TiN emitters are demonstrated. Chapter 4 proposes selective emitter regrowth via MOCVD for increasing β by decreasing base diffusion ($I_{B,diff.}$) and Auger current ($I_{B,Auger}$), and increasing f_t/f_{max} by enabling further reduction in base thickness without degrading base contact resistance. Methods for reactivating base carbon doping post regrowth are proposed, and a process flow for RF HBT with regrown emitter semiconductor is proposed which incorporates the 'ALD Emitter' emitter technology demonstrated in 3. Chapter 5 shows experimental results of LADs where the emitter semiconductor is regrown via MOCVD. Successful reactivation of the p-InGaAs carbon dopant, and working transistors are demonstrated. A maximum β of 28 is measured on HBT 74Q4 with emitter area of 0.8x4μm^2, and β_{bulk} of 96 is extracted from the sample. The design for

74Q4 uses a 4nm extrinsic base doped from 12-11x10$^{19}cm^{-3}$ and a 16 nm intrinsic base doped from 11-7x10$^{19}cm^{-3}$.

Scaling of regrown-emitter HBTs is required for realizing the benefits of this design as compared to a non-regrowth HBTs. If base leakage currents and base surface damage is minimized at small device dimensions, then InP/InGaAs emitter regrowth HBTs would provide a forward path that is superior to traditional non-regrowth devices.

References

[1] J. S. Yuan, SiGe, GaAs, and InP Heterojunction Bipolar Transistors.. Wiley, 1999.

[2] K Honjo, Applications of HBTs, Solid-State Electronics, Volume 38, Issue 9, September 1995, Pages 1569-1573, ISSN 0038-1101, http://dx.doi.org/10.1016/0038-1101(95)00068-5.

[3] J. Hacker, M. Seo, A. Young, Z. Griffith, M. Urteaga, T. B. Reed, M. J. W.. Rodwell, and M. Field, "THz MMICs based on InP HBT Technology," in . 2010 MTT-S International Microwave Symposium Digest (MTT), May 2010.

[4] E. Bloch, H.-C. Park, T. B. Lu, M. Reed, Z. Griffith, L. A. Johansson, L. A.. Coldren, D. Ritter, and M. J. W. Rodwell, "A 120 GHz InP HBT. phase-lock-loop IC for optical wavelength synthesis," in 2012 MTT-S. International Microwave Symposium Digest (MTT), Jun. 2012.

[5] T. B. Reed, Z. Griffith, P. Rowell, M. Field, and M. J. W. Rodwell, "A 180mW. InP HBT Power Amplifier MMIC at 214 GHz," in IEEE Compound. Semiconductor IC Symposium, Oct. 2013.

[6] Z. Griffith, T. B. Reed, M. J. W. Rodwell, and M. Field, "A 220 GHz. Solid-State Power Amplifier MMIC with 26.8 dB S_{21} Gain, and. 55.5 mW P_{out} at 17.0 dB Compressed Gain ," in 2013. International Microwave Symposium, Jun. 2013.

[7] M. J. W. Rodwell, M. Urteaga, T. Mathew, D. Scotts, D. Mensa, Q. Lee,. J. Guthrie, Y. Betser, S. C. Martin, R. P. Simth, S. Jaganathan, S. Krishnan,. S. I. Long, L. Pullela, B. Agarwal, U. Bhattacharya, L. Samoska, and. M. Dahlström, "Submicron scaling of HBTs," IEEE Trans. Electron. Devices, vol. 48, p. 2606, Nov. 2001.

[8] M. J. W. Rodwell, M. Le, and B. Brar, "InP Bipolar ICs: Scaling Roadmaps,. Frequency Limits, Manufacturable Technologies," Proc. IEEE, vol. 92,. pp. 271–286, Feb. 2008.

[9] M. Urteaga, R. Pierson, P. Rowell, V. Jain, E. Lobissor, and M. J. W. Rodwell,. "130 nm InP DHBTs with f_{τ} >0.52 THz and. $f_{\max}$ >1.1 THz," in 69th IEEE Device Research Conference,. Jun. 2011.

[10] Lai, R.; Mei, X.B.; Deal, W.R.; Yoshida, W.; Kim, Y.M.; Liu, P.H.; Lee, J.; Uyeda, J.; Radisic, V.; Lange, M.; Gaier, T.; Samoska, L.; Fung, A., "Sub 50

nm InP HEMT Device with Fmax Greater than 1 THz," in Electron Devices Meeting, 2007. IEDM 2007. IEEE International , vol., no., pp.609-611, 10-12 Dec. 2007

[11] Deal, W.R., "InP HEMT for sub-millimeter wave space applications: Status and challenges," in Infrared, Millimeter, and Terahertz waves (IRMMW-THz), 2014 39th International Conference on , vol., no., pp.1-3, 14-19 Sept. 2014

[12] Rode, J.C.; Chiang, H.-W.; Choudhary, P.; Jain, V.; Thibeault, B.J.; Mitchell, W.J.; Rodwell, M.J.W.; Urteaga, M.; Loubychev, D.; Snyder, A.; Wu, Y.; Fastenau, J.M.; Liu, A.W.K., "An InGaAs/InP DHBT With Simultaneous f_t/f_{max} 404/901 GHz and 4.3 V Breakdown Voltage," in Electron Devices Society, IEEE Journal of the , vol.3, no.1, pp.54-57, Jan. 2015

[13] I. Vurgaftman, J. Meyer, and L. Ram-Mohan, "Band parameters for III V. compound semiconductors and their alloys," J. Appl. Phys., vol. 89,. p. 5815, Jun. 2001.

[14] V. Jain, InP DHBTs in a Refractory Emitter Process for THz Electronics.. Ph.D. Thesis, University of California, Santa Barbara, Santa. Barbara, Ca, U.S.A., 2011.

[15] J. Rode, IC Fabrication Technology for Highly Scaled THz DHBTs.. Ph.D. Thesis, University of California, Santa Barbara, Santa. Barbara, Ca, U.S.A., 2015.

[16] H. Chiang, Design and Fabrication of Sub-100nm Base-Emitter Junctions of THz InP DHBTs.. Ph.D. Thesis, University of California, Santa Barbara, Santa Barbara, Ca, U.S.A., 2014...

[17] . Lateral carrier diffusion and current gain in terahertz InGaAs/InP double-heterojunction bipolar transistors. Chiang, Han-Wei and Rode, Johann C. and Choudhary, Prateek and Rodwell, Mark J. W., Journal of Applied Physics, 115, 034513 (2014)

[18] Pei-Ing Lee, John Cronin, and Carter Kaanta. Chemical Vapor Deposition of Tungsten (CVD W) as Submicron Interconnection and Via Stud. J. Electrochem. Soc. 1989 136(7): 2108-2112

Chapter 2

HBT Theory

This chapter introduces the basic principles of operation of a BJT/HBT, and discusses the epitaxial design and essential device parameters of a modern RF HBT. An in-depth analysis of DC current gain β and p-InGaAs contact technology is presented for the next generation of RF HBTs.

2.1 Device Structure

This section describes the principle of operation for a basic BJT, and the benefits of using an HBT instead of a BJT.

2.1.1 Principle of Operation

A Bipolar Junction Transistor (BJT) consists of two p-n diodes joined back to back to form either a n-p-n or a p-n-p transistor. A schematic of an n-p-n BJT

is shown in Figure 2.1 along with its band diagram at thermal equilibrium. The most common operation mode for a BJT is the forward-active mode, where the emitter-base diode is forward biased and the base-collector diode is reverse biased.

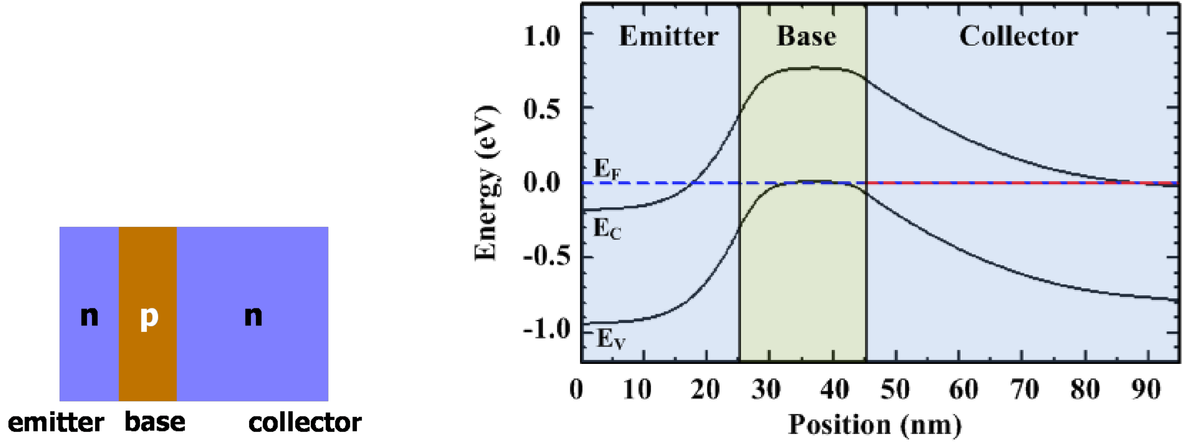

Figure 2.1: A simplified schematic of a BJT is shown on the left. The corresponding band diagram is shown on the right with the fermi level E_{F}, conduction band E_{C}, and valence band E_{V} labeled accordingly.

Figure 2.2 shows the band diagram of a BJT in forward-active mode with electrons and holes drawn for illustrative purposes only. The number of electrons (black circles) diffusing from the emitter to base drops off exponentially with the conduction barrier height along the emitter-base junction (2.1).

$$n_{\mathrm{x=0}} = n_{\mathrm{emitter}} \exp\left(\frac{q(V_{BE} - V_{bi})}{KT}\right) \tag{2.1}$$

The electrons then diffuse towards the base-collector junction. Since the base thickness (w_{B}) is much smaller than the electron diffusion length in the base (λ_{e}), the diffusion profile is given by Eqn 2.2.

$$n_{\mathrm{x}} = n_{\mathrm{x=0}}\left(1 - \frac{x}{w_{\mathrm{B}}}\right) + \frac{J_{\mathrm{C}}}{q v_{\mathrm{s}}} \frac{x}{w_{\mathrm{B}}} \tag{2.2}$$

Figure 2.2: Band diagram of a BJT in forward-active mode illustrating majority carrier drift-diffusion.

There are also holes (white circles) diffusing from the base to emitter, but are far fewer in number since the base p-doping is lower than the emitter n-doping. The majority carrier fermi levels are indicated in each of the three regions.

The 2nd term on the R.H.S. is due to finite velocity of the electrons as they are swept away by the base-collector depletion electric field, where they are collected by the collector terminal. Since $w_{\mathrm{B}} \ll \lambda_{\mathrm{electron}}$, most of the electrons diffuse from the emitter-base to the base-collector junction without recombining with the hole majority carriers in the base i.e. $I_{\mathrm{E}} \approx I_{\mathrm{C}}$.

To summarize, a small change in the base hole current (I_B) leads to a large change in the collector electron current (I_C). Thus, a BJT in forward-active mode amplifies I_B and the amplified current is I_C. A common figure of merit for

a BJT is the DC current gain β which is defined as:

$$\beta = \frac{I_{\mathrm{C}}}{I_{\mathrm{B}}} = \frac{I_{\mathrm{E}} - I_{\mathrm{B}}}{I_{\mathrm{B}}} \tag{2.3}$$

The base current (I_B) consists of holes that recombine with electrons diffusing along the base, as well as holes diffusing in to the emitter ($I_{E,hole}$). The latter hole diffusion current is a parasitic current, and is thus undesirable. A Hetero-junction Bipolar Junction Transistor (HBT) can be used to suppress this hole diffusion current, by increasing the barrier for holes diffusing from the base to emitter. Thus, $I_{E,electron}/I_{E,hole}$ for the device increases exponentially as this barrier increases. Figure 2.3 shows the band diagram of an HBT with an abrupt hetero-junction at the emitter-base interface under forward-active mode. Note that while the hole diffusion barrier has increased by $\triangle E_{\mathrm{V}}$, there is no change in the electron diffusion barrier as they diffuse from emitter to base. For this design, $I_{E,electron}/I_{E,hole}$ increases by $exp(\triangle E_{\mathrm{V}})$.

Figure 2.4 shows an HBT with an alloy grade between the emitter-base interface. In this case, the hole diffusion barrier has increased by $\triangle E_{\mathrm{G}}$, and $I_{E,electron}/I_{E,hole}$ by $exp(\triangle E_{\mathrm{G}})$.

Figures 2.5, 2.6 show a cross-sectional schematic and TEM image respectively of a UCSB RF HBT.

The emitter metal must maintain a high aspect ratio to maximize distance between the metal plane and the transistor and thus ensure a clean RF environment. As mentioned in 2.1.3, the gap between the base metal and emitter-base junction is minimized in order to reduce R_{bb}, and the base mesa is undercut in

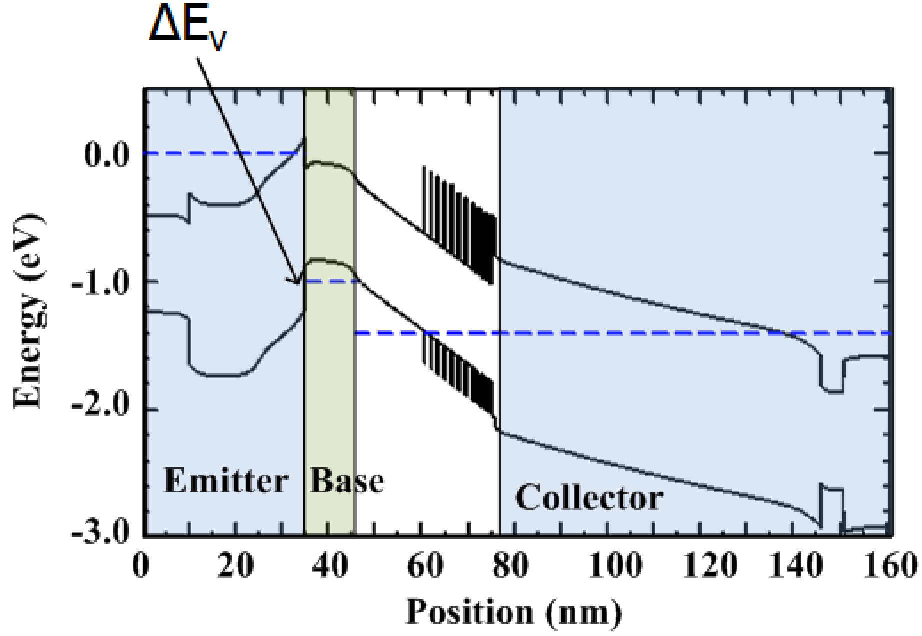

Figure 2.3: Band diagram of an abrupt InP/InGaAs HBT in forward-active mode. There exists a diffusion barrier $\triangle E_{\mathrm{V}}$ for holes diffusing from base to emitter.

order to reduce C_{CB}.

Sections 2.1.2 - 2.1.4 discuss the epitaxial and structural design of the device in further detail.

2.1.2 HBT Emitter Design

A modern RF HBT emitter epitaxial design is shown in Table 2.1.

Layer	Semiconductor	Thickness (Å)	Doping (cm^{-3})
Emitter cap	$\mathrm{In}_{0.53}\mathrm{Ga}_{0.47}\mathrm{As}$	100	8×10^{19}:Si
Emitter	InP	150	5×10^{19}:Si
Emitter	InP	150	3×10^{18}:Si

Table 2.1: Typical emitter epi design of an RF HBT at w_{E} of 100nm.

The top most layer of the emitter is highly doped n-InGaAs for obtaining low

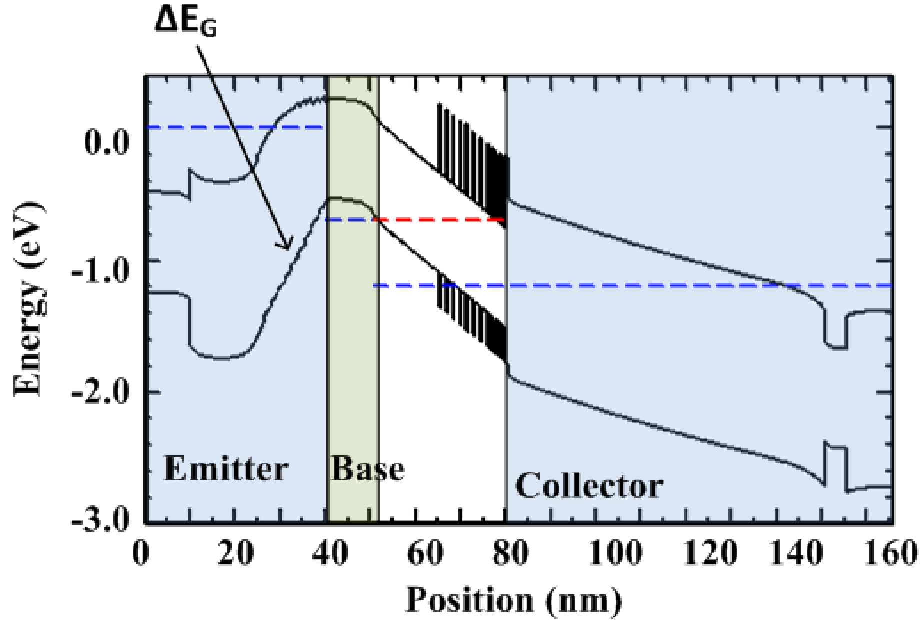

Figure 2.4: Band diagram of a graded InP/InGaAs HBT in forward-active mode with the space charge region in the emitter graded from InP to InGaAs. The diffusion barrier is now $\triangle E_{\mathrm{G}}$ for holes diffusing from base to emitter.

contact resistivity. The emitter access resistance R_{ex} includes the emitter metal contact resistivity as well as the emitter metal resistance. The emitter layer that forms the emitter-base junction is n-InP which suppresses hole diffusion from base to emitter due to the valence band offset $\triangle E_{\mathrm{V}}$. The InP at the emitter base junction has a lower doping n_{de} over a thickness t_{E} in order to optimize emitter-base junction capacitance C_{je} 2.4.

$$C_{\mathrm{je}} = \frac{\epsilon_0 \epsilon_{\mathrm{r}} A_{\mathrm{je}}}{t_{\mathrm{E}}} \tag{2.4}$$

Where ϵ_{r}, A_{je} are the dielectric constant of InP and emitter-base junction area respectively. The lower doped region must be thick enough to minimize C_{je}, but the increase in emitter access resistance R_{ex} due to low space charge must

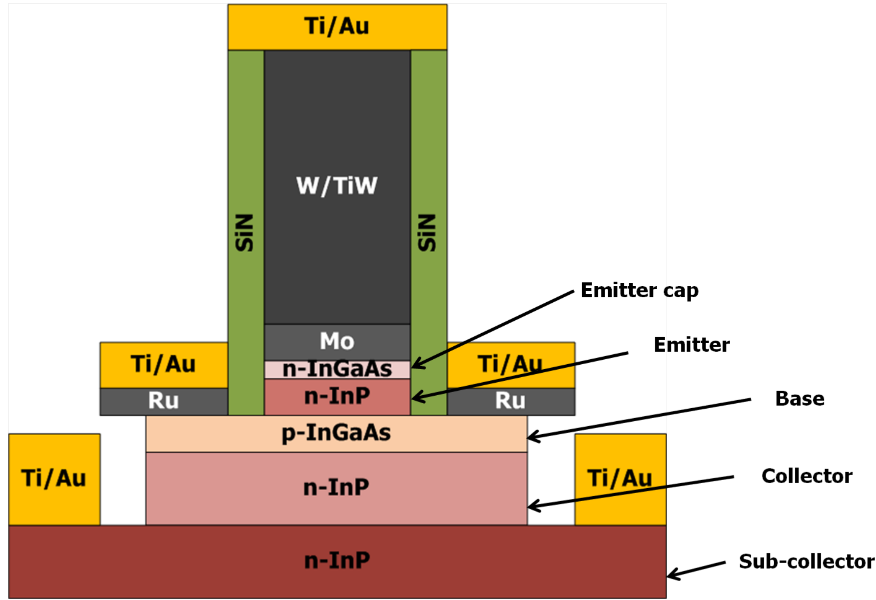

Figure 2.5: Cross-sectional schematic of a UCSB RF HBT.

also be considered. Equation 2.5 shows R_{ex}, which consists of the emitter metal resistance, contact resistance, and emitter space charge resistance due to the lower doped space charge layer.

$$R_{\text{ex}} = R_{\text{em,metal}} + R_{\text{em,cont}} + R_{\text{em,sc}}$$

$$R_{\text{ex}} = R_{\text{sh,em,metal}} \frac{T^2{}_{\text{em,metal}}}{A_{\text{ec}}} + \frac{\rho_{\text{em}}}{A_{\text{ec}}} + \frac{1}{q}\frac{\partial \triangle E_{\text{fn}}}{\partial I_{\text{E}}} \tag{2.5}$$

$R_{\text{sh,em,metal}}$: Emitter metal sheet resistance

$T^2{}_{\text{em,metal}}$: Emitter metal thickness

A_{ec} : Emitter contact area

ρ_{em} : Emitter contact resistivity

$\triangle E_{\text{fn}}$: Drop in electron quasi-Fermi level

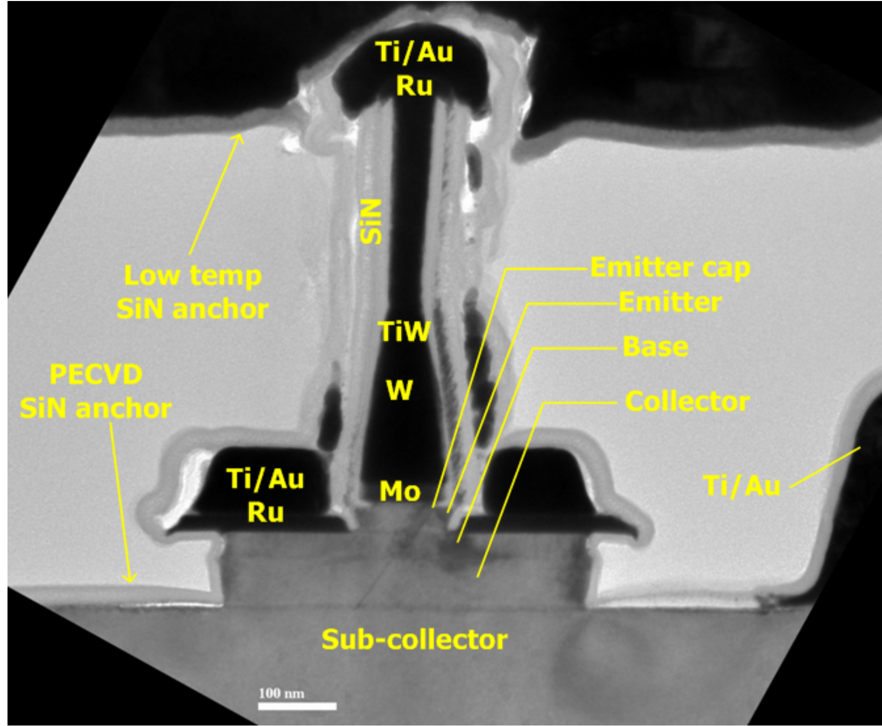

Figure 2.6: Cross-sectional TEM image of a UCSB RF HBT.

$\triangle E_{\text{fn}} = \int_{\text{t}_{\text{dep}}} \frac{J_{\text{E}}}{\mu_{\text{n}}(z)n(z)} dz$

The doping of the space charge region n_{de} must also be high enough to support high emitter current density J_{E} for high frequency operation. It has been empirically shown that the emitter must support twice the collector Kirk current density i.e. $J_{\text{E}} \propto 2J_{\text{C}}$ [1]. Low doping in the space charge region leads to emitter starvation [2] when the mobile electron density exceeds the fixed charge density as shown by 2.7. This shifts the injection point for electrons into the base, thus increasing the effective base thickness (similar to Kirk effect) and reducing J_{E} and transconductance g_{m}:

$$g_{\text{m}} = \frac{\partial I_{\text{C}}}{\partial V_{\text{BE}}} \tag{2.6}$$

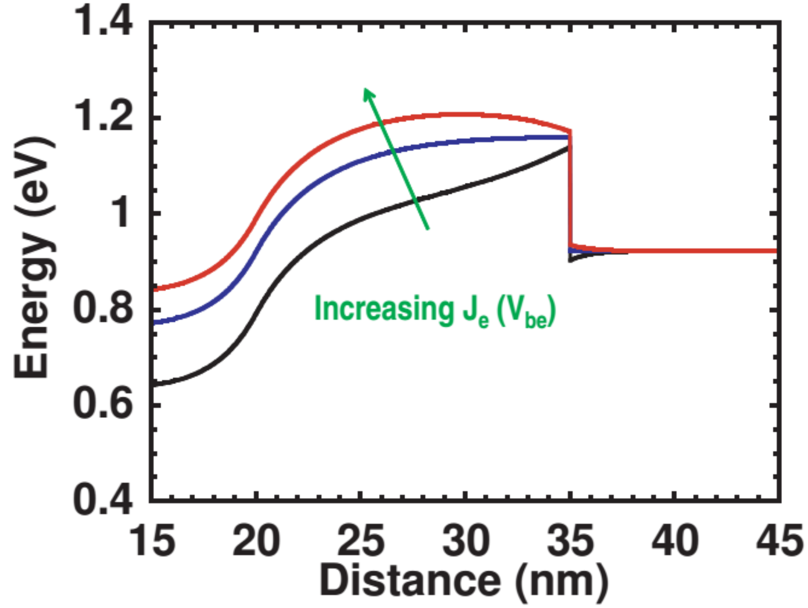

Figure 2.7: Band diagram of the emitter region at increasing emitter-base biases. Emitter starvation occurs at sufficiently high J_E [1].

At high current densities, electron injection is governed by Fermi-Dirac statistics and not Boltzmann statistics. Due to this, J_E no longer increases exponentially with V_{be}, and now has a quadratic dependence. This further leads to g_m degradation [3].

2.1.3 HBT Base Design

A traditional UCSB RF HBT base epitaxial design is shown in Figure 2.2.

Layer	Semiconductor	Thickness (Å)	Doping (cm^{-3})
Base	$In_{0.53}Ga_{0.47}As$	300	$9-5\times10^{19}$:C

Table 2.2: Typical base epi design of an RF HBT at w_E of 100nm.

The base employs a doping grade, where the highest doping is at the emitter-base junction and the lowest at the base-collector. This induces a quasi-electric

field that accelerates electrons towards the base, thus reducing base transit time (τ_b) and minimizing electron-hole recombination in the base. The base transit time τ_b must be computed based on the drift-diffusion model and is given by:

$$\tau_\mathrm{B} = \frac{T_\mathrm{B}^2}{D_\mathrm{n}}\frac{kT}{\Delta E_\mathrm{C}}[1 - \frac{kT}{\Delta E_\mathrm{C}}(1 - exp(-\frac{\Delta E_\mathrm{C}}{kT}))] + \frac{T_\mathrm{B}}{v_\mathrm{exit}}\frac{kT}{\Delta E_\mathrm{C}}(1 - exp(\frac{\Delta E_\mathrm{C}}{kT})) \quad (2.7)$$

This quasi electric field also drives electrons away from the base surface, thus reducing the number of electrons diffusing towards the base contact (Section 2.3.3). This further increases β.

Experimentally, it has been determined that high base doping is required for low ohmic contact resistivity [4] [5]. Thus, it is important for p-InGaAs doping near the emitter-base junction to be as high as possible. Unfortunately, this leads to β degradation due to increased Auger recombination, which is described in further detail in section 2.3.2.

The base access resistance (R_bb) components are explained pictorially in Figure 2.8 and the corresponding equation is shown in Equation 2.8.

$$\begin{aligned} R_\mathrm{bb} &\approx R_\mathrm{be,spread} + R_\mathrm{gap} + R_\mathrm{b,cont.} + R_\mathrm{b,metal} \\ &= \frac{R_\mathrm{sh,em}W_\mathrm{E}}{12L_\mathrm{E}} + \frac{R_\mathrm{sh,gap}W_\mathrm{gap}}{2L_\mathrm{E}} + \frac{\sqrt{R_\mathrm{sh,B,cont.}\rho_\mathrm{B,cont.}}}{2L_\mathrm{E}}coth(\frac{W_\mathrm{B,cont.}}{L_\mathrm{T}}) + \rho_\mathrm{metal}\frac{W_\mathrm{bc}}{6L_\mathrm{E}} \ . \end{aligned} \quad (2.8)$$

The space charge resistance in the base R_gap is dependent on the base sheet resistance and the gap between the emitter-base junction and base metal contact. In RF HBTs, the emitter width has been reduced to 100nm and the gap spacing to 10nm [6] such that R_gap is increasingly becoming a smaller portion of R_bb [7].

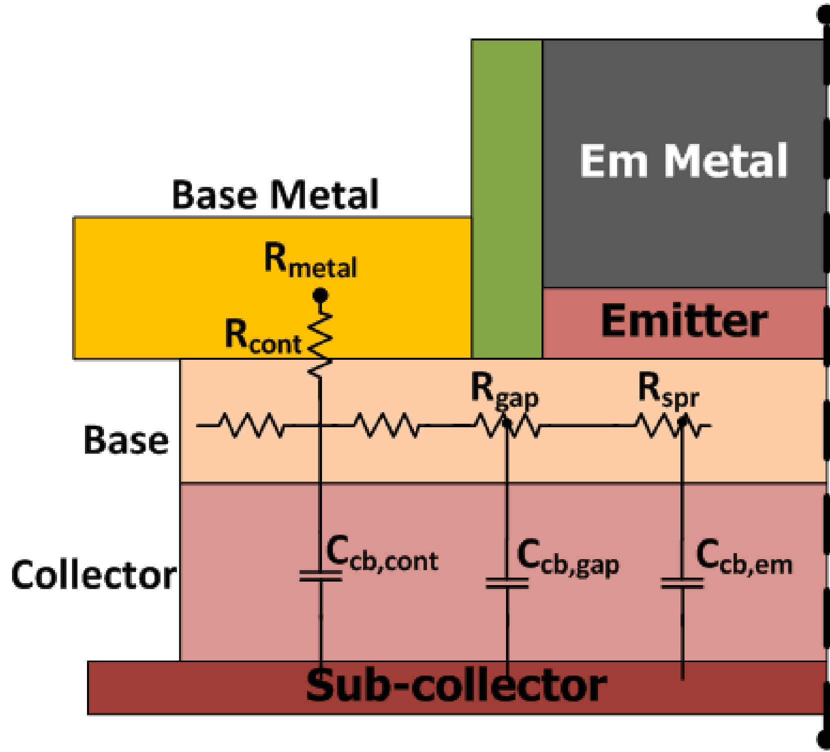

Figure 2.8: Cross-sectional schematic of distributed RC network in the base–collector region of an HBT. The device is symmetric along the dashed line i.e. only one side of the device is shown.

HBT scaling laws (Section 2.2) require that the base metal width $w_{\text{metal,bc}}$ also shrink for higher f_{max} which increases R_{metal}. Consequently, the metal thickness needs to be increased as HBTs are scaled down [7].

2.1.4 HBT Collector Design

A traditional UCSB RF HBT collector epitaxial design is shown in Table 2.3.

The collector design is chosen to minimize any barriers for electrons travelling from the base to the sub-collector. An InGaAs/InAlAs chirped superlattice is used to smooth out the InGaAs/InP conduction band discontinuity. To min-

Layer	Semiconductor	Thickness (Å)	Doping (cm^{-3})
Setback	$In_{0.53}Ga_{0.47}As$	95	1×10^{17}:Si
B-C grade	-	120	1×10^{17}:Si
δ-doping	InP	30	5×10^{18}:Si
Collector	InP	455	1×10^{17}:Si
Sub-collector	InP	75	2×10^{19}:Si
Sub-collector	$In_{0.53}Ga_{0.47}As$	75	4×10^{19}:Si
Sub-collector	InP	3000	1×10^{19}:Si
Etch stop	$In_{0.53}Ga_{0.47}As$	35	undoped
Substrate	InP	-	undoped

Table 2.3: Typical collector epi design of an RF HBT at w_{E} of 100nm.

imize quantum reflections due to the superlattice, an n-InGaAs setback layer is introduced before it to increase the electrons kinetic energy. The superlattice introduced a quasi-electric field which is countered by a pulse doping after it on the collector side [8].

The collector doping needs to be low, such that it is fully depleted in forward active mode with zero base-collector bias. This minimizes base-collector capacitance C_{cb} by maximizing space-charge width, and also minimizes change in C_{cb} as V_{cb} is modulated. Figure 2.8 shows a physical interpretation of C_{cb}.
The collector doping also needs to be high enough to support a desired Kirk collector current density $J_{\mathrm{Kirk,c}}$ i.e. the collector current density when the electric field at the base side of the collector is zero (Equation 2.9) [9].

$$J_{\mathrm{C,Kirk}} = q n_{\mathrm{C}} v_{\mathrm{e,sat}} \tag{2.9}$$

Where n_{C}, $v_{\mathrm{e,sat}}$ are the collector electron concentration and saturation velocity respectively.
The transit time for electrons traveling across the collector in the Kirk regime is

given by Equation 2.10, since they traverse the majority of the collector without scattering due to a large $\Gamma - L$ separation [10] [11].

$$\tau_{\mathrm{C}} = \frac{\Delta Q_{\mathrm{C}}}{\Delta I_{\mathrm{C}}} = \int_0^{T_{\mathrm{C}}} \frac{1 - x/T_{\mathrm{C}}}{v(x)}\, dx = \frac{T_{\mathrm{C}}}{2v_{\mathrm{eff.}}} , \tag{2.10}$$

As the collector is designed for higher $J_{\mathrm{Kirk,c}}$ and consequently higher f_{t}, the collector thickness T_{c} must decrease to ensure total depletion and this reduces the device breakdown voltage V_{ce}. Thus, there is a fundamental trade-off between cutoff frequency and breakdown voltage.

The collector access resistance R_{cc} includes the collector contact resistance $R_{\mathrm{c,contact}}$, the lateral resistance between the base-collector mesa and the collector contact $R_{\mathrm{c,gap}}$ and the spreading resistance in the intrinsic region under the base-collector mesa $R_{\mathrm{c,intrinsic}}$. Thus, R_{cc} is

$$\begin{aligned} R_{\mathrm{CC}} &\approx R_{\mathrm{C,intrinsic}} + R_{\mathrm{C,gap}} + R_{\mathrm{C,cont.}} \\ &= \frac{R_{\mathrm{sh,C}} W_{\mathrm{mesa}}}{12 L_{\mathrm{E}}} + \frac{R_{\mathrm{sh,C}} W_{\mathrm{C,gap}}}{2 L_{\mathrm{E}}} + \frac{\rho_{\mathrm{C,cont.}}}{2 L_{\mathrm{t}} L_{\mathrm{e}}} \end{aligned} \tag{2.11}$$

2.1.5 HBT Equivalent Circuit Model

Figure 2.9 shows the equivalent circuit model of a BJT using the hybrid-π model [12]. The respective terminal resistances and capacitances have been described previously.

R_{be} is the differential resistance between the base-emitter that is dependent on the bias point:

$$R_{\mathrm{be}} = \left.\frac{\partial V_{\mathrm{be}}}{\partial I_{\mathrm{C}}}\right|_{\mathrm{V_{be}}} \tag{2.12}$$

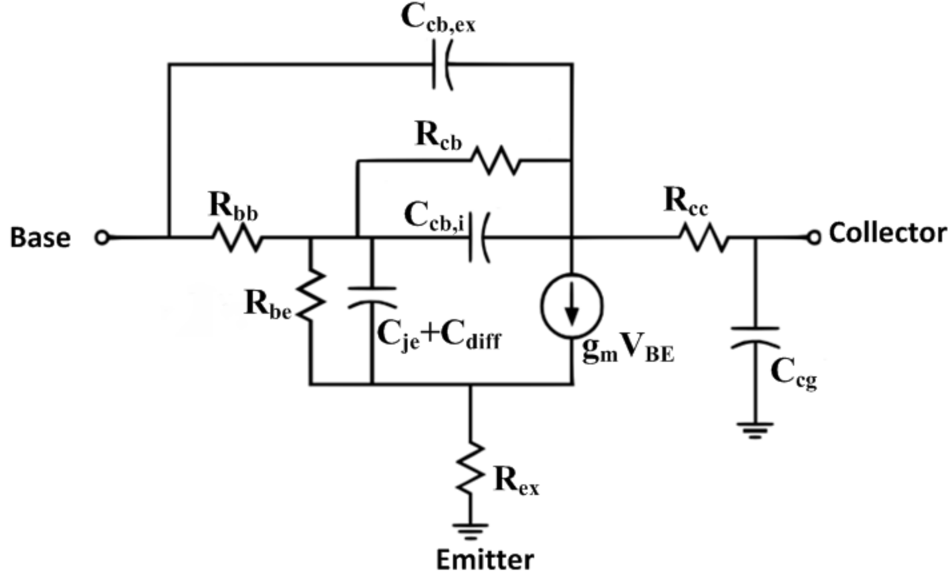

Figure 2.9: Hybrid-π equivalent circuit model of a BJT.

If we assume that β is independent of V_{be} i.e. $\partial\beta/\partial V_{\mathrm{be}} = 0$, and β is large enough that the emitter and collector currents are approximately equal, then the resistance can be re-written as:

$$R_{\mathrm{be}} = \frac{\beta}{g_{\mathrm{m}}} \tag{2.13}$$

There exists an additional capacitance C_{diff} at the base-emitter junction due to carrier charge storage in forward bias.

$$C_{\mathrm{diff}} = \frac{\partial I_{\mathrm{E}}}{\partial V_{\mathrm{be}}}(\tau_{\mathrm{b}} + \tau_{\mathrm{c}}) = g_{\mathrm{m}}(\tau_{\mathrm{b}} + \tau_{\mathrm{c}}) \tag{2.14}$$

R_{cb} is associated with the base-collector junction, and is used to accurately fit Y_{21} from s parameter measurements [7].

2.2 HBT RF Performance and Scaling

The two important figures of merit for evaluating the RF performance of HBTs are the current gain cut-off frequency f_{t}, and the power gain cut-off frequency f_{max}. f_{t} is the frequency at which the current gain of the device drops below unity i.e. the time it takes for an electron to travel from the emitter to the collector. f_{t} is given by:

$$\frac{1}{2\pi f_{\tau}} = \tau_{\mathrm{EC}} = \tau_{\mathrm{B}} + \tau_{\mathrm{B}} + \frac{\eta kT}{qI_{\mathrm{E}}} C_{\mathrm{je}} + (R_{\mathrm{EX}} + R_{\mathrm{C}} + \frac{\eta kT}{qI_{\mathrm{E}}}) C_{\mathrm{CB}} \;, \tag{2.15}$$

f_{max} is the frequency at which the unilateral Mason's gain becomes unity i.e. it is the maximum frequency of oscillation in a circuit where only only active device is present [13]. It is given by:

$$f_{\mathrm{max}} = \sqrt{\frac{f_{\tau}}{8\pi (RC)_{eff.}}} \tag{2.16}$$

In order to increase the $f_{\mathrm{t}}/f_{\mathrm{max}}$ of a transistor, the time delays $(\tau_{\mathrm{b}}, \tau_{\mathrm{c}})$ must be reduced by shrinking the device vertically, and the RC charging delays must be reduced by shrinking the device laterally and reducing access resistances. To first order, the scaling laws for various HBT design parameters are listed in table 2.4 for increasing RF performance.

The base contact resistivity is related to the base doping such that $\rho_{\mathrm{B,cont.}} \propto {N^{-2/3}}_{\mathrm{A,cont.}}$ as the doping levels are highly degenerate [14] [4].
Using these scaling laws, it is possible to make a scaling roadmap for HBTs, that lists the specific design parameters required in a device for achieving certain RF

Parameters		Requirement
Base thickness	T_B	$\gamma^{-1/2}$
Collector thickness	T_C	γ^{-1}
B-C mesa width	W_{BM}	γ^{-2}
B-E junction width	W_E	γ^{-2}
Emitter current density	J_E	γ^{2}
Specific emitter contact resistivity	$\rho_{E,cont.}$	γ^{-2}
Specific base contact resistivity	$\rho_{B,cont.}$	$\approx \gamma^{-2}$
Base sheet resistance	$R_{B,sh.}$	$\gamma^{-1/2}$
Base doping under contact	$N_{A,cont.}$	γ^{3}

Table 2.4: Scaling laws of HBTs: the required change for improving f_τ and f_{max} by a factor of γ.

performance [15]. Such a roadmap is shown in figure 2.10.

Design	Emitter	256	128	64	32	Width (nm)
		8	4	2	1	Access ρ (Ω·μm²)
	Base	175	120	60	30	Contact width (nm)
		10	5	2.5	1.25	Contact ρ (Ω·μm²)
	Collector	106	75	53	37.5	Thickness (nm)
Performance	Current density	9	18	36	72	mA/μm²
	Breakdown voltage	4	3.3	2.75	2-2.5	V
	f_τ	520	730	1000	1400	GHz
	f_{max}	850	1300	2000	2800	GHz

Figure 2.10: Scaling roadmap for InP/InGaAs HBTs [15]

The primary challenges faced in achieving higher RF performance in HBTs today are development of process flows for narrower emitter widths, and achieving low base contact resistance to p-InGaAs [1] [16] [7] [4]. Section 2.4 provides a brief outline of the work done at UCSB for achieving low base contact resistivity, and details the problems associated with the current technology.

Furthermore, it has been shown experimentally, and verified via simulations that the DC current gain β drops as HBT emitter widths are scaled down for higher RF performance [18]. Although not listed in the roadmap above, an HBT requires high β in order to be used in power amplifiers, digital-analog converters, and mixers. The following section details the factors that degrade β, as shown by [16] and explores the design space for improving β.

2.3 DC Current Gain β

It has been observed experimentally that β decreases as the emitter width is scaled down. Figure 2.11 shows this [16].

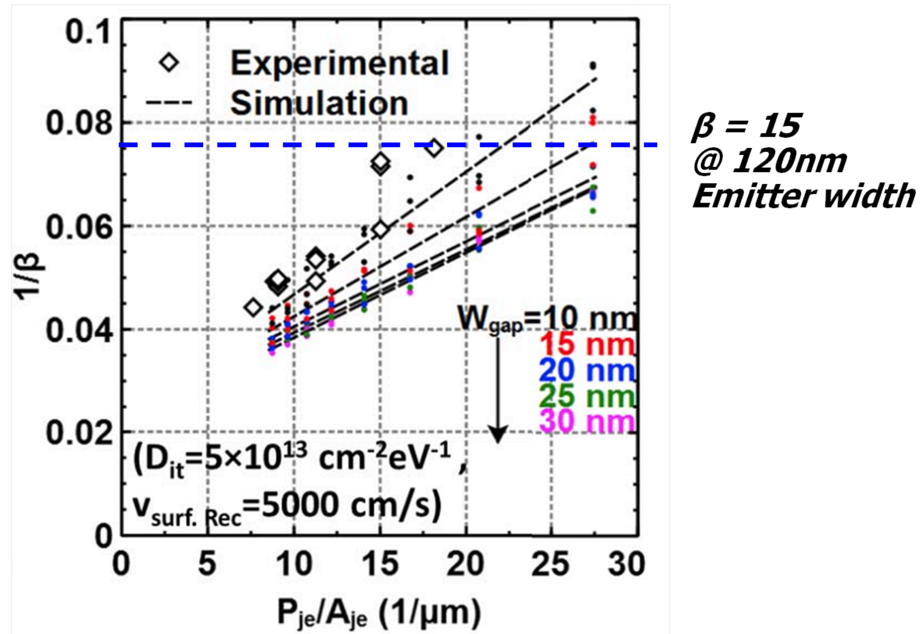

Figure 2.11: HBT DC current gain β plotted as a function of emitter perimeter/area. Experimental and simulated data points show a drop in β as the emitter width is reduced. [16]

A decrease in β implies an increase in I_B/I_E as the emitter width is scaled. It

is instructive to look at the relation between β and the base current components as:

$$\begin{aligned} \frac{1}{\beta} &\propto (I_{SRH} + I_{Rad} + I_{Auger} + I_{Diff} + I_{srf,cond} + I_{srf,rec}) \\ &\propto (\frac{1}{\beta_{SRH}} + \frac{1}{\beta_{Rad}} + \frac{1}{\beta_{Auger}} + \frac{1}{\beta_{Diff}} + \frac{1}{\beta_{srf,cond}} + \frac{1}{\beta_{srf,rec}})^{-1} \end{aligned} \tag{2.17}$$

Figure 2.12 shows the various base current components. The physical explanation for the current components and their respective scaling factors are discussed in the following sub-sections, as well potential methods of decreasing them and increasing β.

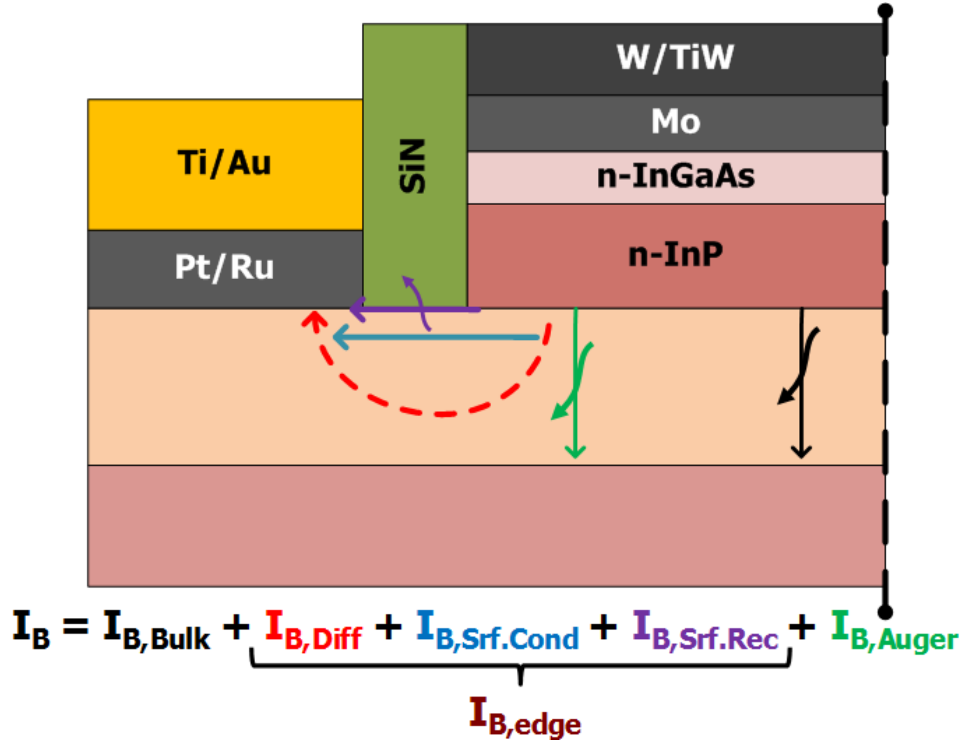

Figure 2.12: A cross-sectional schematic of an HBT that shows the various base current components.

2.3.1 Schockley-Read-Hall and Radiative Recombination Current (I_{SRH},I_{rad})

As the electrons traverse the base, they recombine with the hole majority carriers base on Shockley-Read-Hall (SRH) statistics [19]. The rate of recombination for the carriers is given by:

$$R_{\mathrm{SRH}} = C_{\mathrm{SRH}}(np - {n_{\mathrm{i}}}^2) \tag{2.18}$$

where n_{i} is the intrinsic carrier concentration, and C_{SRH} is the SRH recombination coefficient.

It is clear that R_{SRH} increases for HBTs designed for higher cut-off frequencies (Table 2.5, 2.4), but the area of recombination decreases due to lateral and vertical scaling.

Since InGaAs is a direct bandgap semiconductor, the electrons can also able to recombine directly with a hole and emit photons. The radiative recombination rate has a similar expression to 2.18, except that C_{SRH} is replaced by C_{rad} [16].

2.3.2 Auger Recombination Current (I_{Auger})

Auger recombination is a recombination process involving three or more states in the in the conduction and valence band. The process in InGaAs is depicted in Figure 2.13 [20].

It has been shown by [21] that the Auger recombination rate can be written

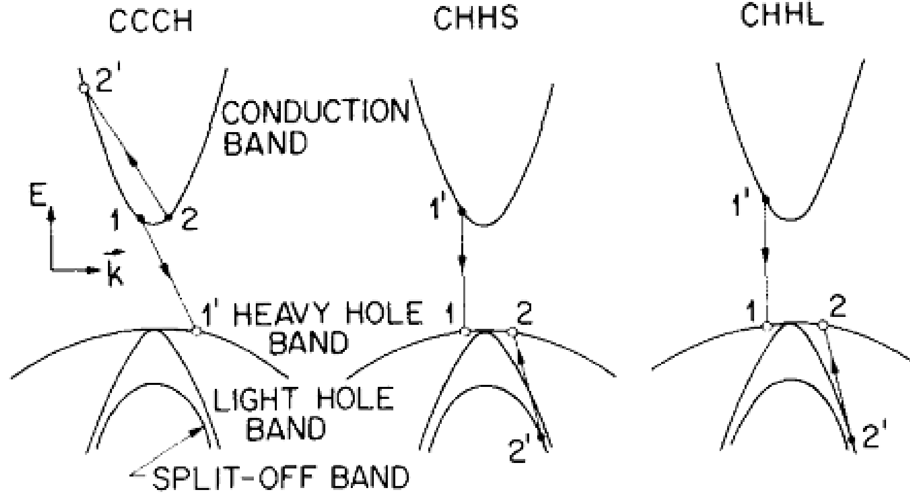

Figure 2.13: The three band-to-band Auger processes are shown. The electrons are represented by closed circles and holes by open circles. Arrows indicate electrons transitions [20].

empirically as:

$$R_{\text{Auger}} = C_{\text{Auger,n}} n^2 p + C_{\text{Auger,p}} n p^2 \tag{2.19}$$

where $C_{\text{Auger,n}}, C_{\text{Auger,p}}$ are the Auger coefficients. In HBTs, the base is heavily p-doped and the injected electrons are minority carriers i.e. p≫n so $C_{\text{Auger,n}}$ can be neglected.

Auger recombination has a quadratic dependence to the base doping, and scales by γ^6 as HBTs are designed for an increase in cut-off frequency by a factor of γ (Table 2.5, 2.4). Auger recombination will contribute significantly to base recombination current in next generation HBTs [16] [1]. An analytic expression for J_{Auger} can be written as:

$$J_{\text{Auger}} = qC_{\text{Auger,p}} \int_0^{w_{\text{B}}} n(x)p(x)^2 dx \tag{2.20}$$

For a doping graded base with a quasi-electric field $\triangle E_{\mathrm{C}}$, the electron concentration at any given point in the base based on the drift-diffusion model is:

$$n(x) = \frac{kTw_{\mathrm{B}}}{\triangle E_{\mathrm{C}}}[\frac{-J_{\mathrm{n}}}{qD_{\mathrm{n}}} + (\frac{-J_{\mathrm{n}}}{qD_{\mathrm{n}}} + \frac{\triangle E_{\mathrm{C}} n(w_{\mathrm{B}})}{kTw_{\mathrm{B}}})e^{\frac{-\triangle E_{\mathrm{C}}}{kTw_{\mathrm{B}}}(w_{\mathrm{B}}-x)}] \tag{2.21}$$

The hole concentration at any point is given by the base doping at that point, and can thus be engineered during growth. [1] explores different base design for reducing Auger recombination while maintaining a high base doping at the emitter-base junction for low base contact resistivity. Section 4.3 improves upon this to further reduce Auger recombination in the base while maintaining low base contact resistivity.

2.3.3 Lateral Diffusion Current (I_{Diff})

The electron carrier profile in the base as they travel to the collector can be computed using Equation 2.21. However this does not take in to account the electrons that diffuse laterally towards the base contact. [18] shows that I_{Diff} is highest in the gap between the base-emitter junction and the base metal contact, and negligible everywhere else. Thus, I_{Diff} scales with the emitter periphery.
Since I_{Diff} is dominated by edge electrons, it increases as the emitter current density J_{E} is increased for faster cut-off frequency (Table 2.5, 2.4).
The doping grade induced quasi-electric field accelerates electrons away from the base surface and reduces I_{Diff}. I_{Diff} is also inversely proportional to the gap spacing between base-emitter junction and base metal as that decreases the diffusion profile slope. While the base doping grade and gap spacing can be increased to

suppress $R_{\text{base,sh}}$, it may also lead to higher base sheet resistance and higher R_{bb}.

2.3.4 Surface Recombination and Conduction Current ($I_{\text{srf,rec}}$, $I_{\text{srf,cond}}$)

The surface gap region in the base contains donor-like trap states that carry positive charge when they capture holes [22]. This charge pins the surface Fermi level of InGaAs at 0.5 eV below the conduction band, and thus induces a depletion region that acts as a channel for electrons traveling from base-emitter junction to base metal [18]. The electrons at the surface can also recombine with the surface states, generating surface recombination current $I_{\text{srf,rec}}$:

$$I_{\text{srf,SRH}} = qn_{\text{s}}(x)v_{\text{srf,rec}} \tag{2.22}$$

where $v_{\text{srf,rec}}$ is the surface recombination velocity of electrons. The density of trapped electrons n_{s} depends on J_{E}, field in the surface depletion region, surface depletion depth, and the scattering function that scatters electrons into the surface channel.

The surface currents $I_{\text{srf,cond}}$, $I_{\text{srf,rec}}$ can be decreased by increasing surface base doping and thus decreasing surface depletion depth. Decreasing the surface trap state density via surface passivation would also reduce the surface currents [23] [24].

2.3.5 DC Current Gain β with HBT Scaling

As emitter width is scaled and base doping increased for higher RF performance, β decreases as the edge base current components do not decrease in proportion to the emitter current, and the I_{Auger} increase is quadratic with the base doping.

Table 2.5 shows the scaling laws for these current components as a function of emitter and base mesa width, base doping, and base thickness as devices are scaled for an increase in cut-off frequencies by a factor of γ.

Parameters	Scaling Requirement	Scaling Effect On Current Components			
		$I_{\text{B,Bulk}}$	$I_{\text{B,Diff}}$	$I_{\text{B,Srf}}$	$I_{\text{B,Auger}}$
$P_{\text{E}}/A_{\text{E}} \approx 1/w_{\text{E}}$	γ^{-2}	γ^{-2}	γ^{0}	γ^{0}	γ^{-2}
$P_{\text{BM}}/A_{\text{BM}}$	γ^{-2}	γ^{0}	γ^{0}	γ^{0}	γ^{0}
J_{E}	γ^{2}	γ^{2}	γ^{2}	$\approx\gamma^{2}$	$\approx\gamma^{2}$
N_{A}	γ^{3}	γ^{3}	γ^{0}	-	γ^{6}
T_{B}	γ^{-1}	γ^{-1}	γ^{0}	γ^{0}	γ^{-1}

Table 2.5: Scaling effect on base current components, as a function of parameter scaling for an increase in f_{τ} and f_{max} by a factor of γ. No current spreading in the base, and a uniformly doped base is assumed.

From the table, it is clear that the base current does not decrease proportionally as the emitter width is scaled for faster cut-off frequencies. Section 3.4 and 4 discuss ways in which β can be increased.

2.4 Base Contact Technology

As discussed in Section 2.2, achieving low base contact resistivity for high RF performance is currently one of the biggest challenges. At UCSB, various base contact technologies have been developed previously, each with their own pros and cons. This section summarizes the work done previously. The limitations of these

technologies is used as a motivation for a part of this dissertation and is discussed in chapter 4.

2.4.1 Lift-Off Pt/Ti/Pd/Au Contacts

Lift-Off Pt or Pd contacts are common in InGaAs devices [25] [5], as they yield contact resistivities $< 100\Omega.\mu m^2$ on p-InGaAs at $> 10^{19} cm^{-3}$ doping [4].

Figure 2.14 shows a cross-sectional TEM image of an HBT with lifted off Pt/Ti/Pd/Au contacts [26].

This technology has the advantage that it requires minimal number of fabrication steps, and uses chemically inert metals that are not attacked by subsequent process chemistry.

However, Pt reacts/diffuses with p-InGaAs [27] and thus the top 6 nm of the base is consumed by metal. The metal no longer contacts the highest doping p-InGaAs as the base has a linear doping grade from the emitter to collector side. Furthermore, lift-off technology introduces photoresist contamination on the p-InGaAs surface which increases base contact resistivity [7].

2.4.2 Refractory Metal Contacts

Surface contamination of the base surface can be minimized by blanket deposition of the base contact metal as soon as the emitter semiconductor is etched away. Furthermore, a refractory metal contact can be used to minimize metal reaction and sinking into the base semiconductor. Previous work has shown that blanket refractory metal contacts can be used to obtain $<1\ \Omega.\mu m^2$ contact resistivities on test structures [28]. Figure 2.15 shows a cross-sectional TEM of an

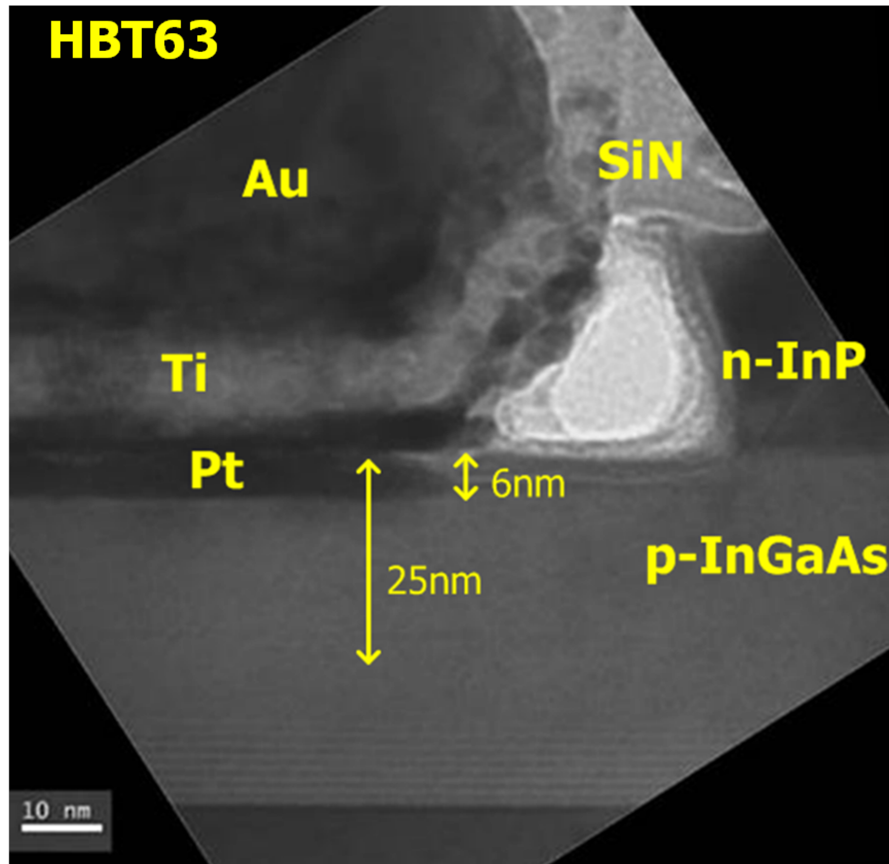

Figure 2.14: A cross-sectional TEM image shows the Pt/Ti/Au base contact sinking into the p-InGaAs base. [16].

RF HBT with a ruthenium base contact. It can be seen that there is no discernible sinking of the metal contact into the InGaAs base. Ti/Au metal pads were lifted off in subsequent steps.

However, it has not been possible to reproduce low contact resistivity on RF HBTs [7]. Section 3.2 details some work that has been done on refractory base contact technology.

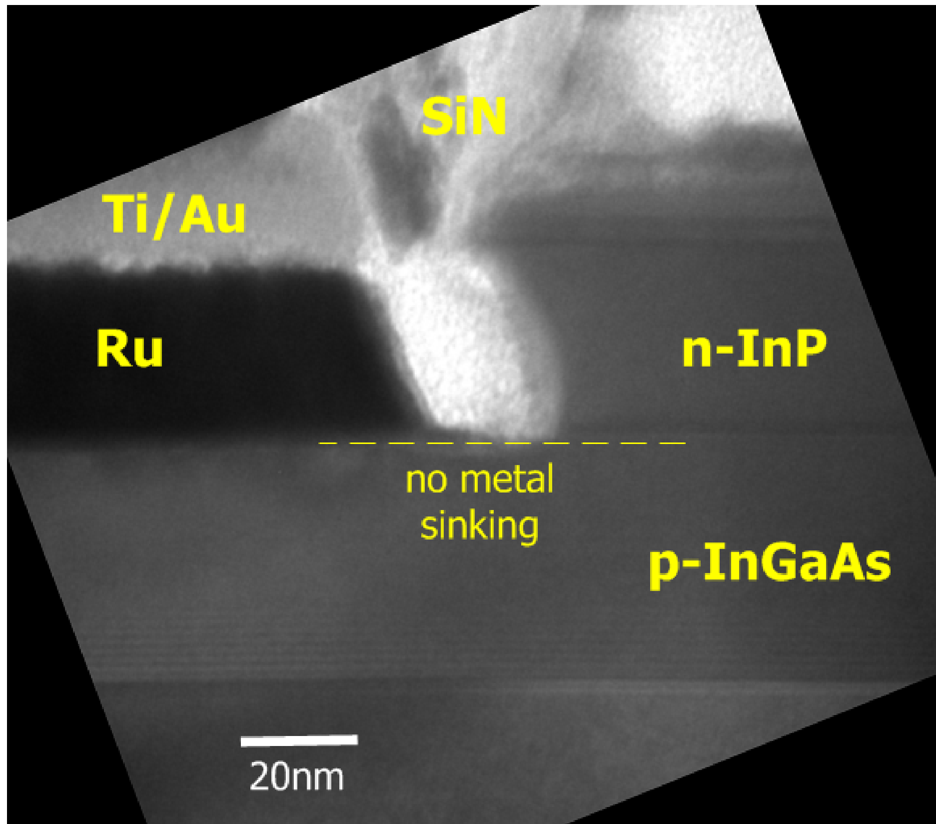

Figure 2.15: A cross-sectional TEM image shows the Ru/Ti/Au base contact with no discernible metal sinking. [7].

2.4.3 Blanket Pt/Ru Metal Contacts

[6] [7] show a blanket base metal contact that uses Pt as the contact metal, and Ru as a refractory metal barrier above it to prevent Ti diffusion into the base. Figure 2.16 shows a cross-sectional TEM of such an RF HBT.

It has been possible to achieve contact resistivity of 3 $\Omega.\mu m^2$ on RF HBTs using blanket Pt/Ru contacts. However, the technology still suffers from contact metal sinking, although the sinking depth has been reduced compared to lifted-off Pt/Ti/Pd/Au contacts.

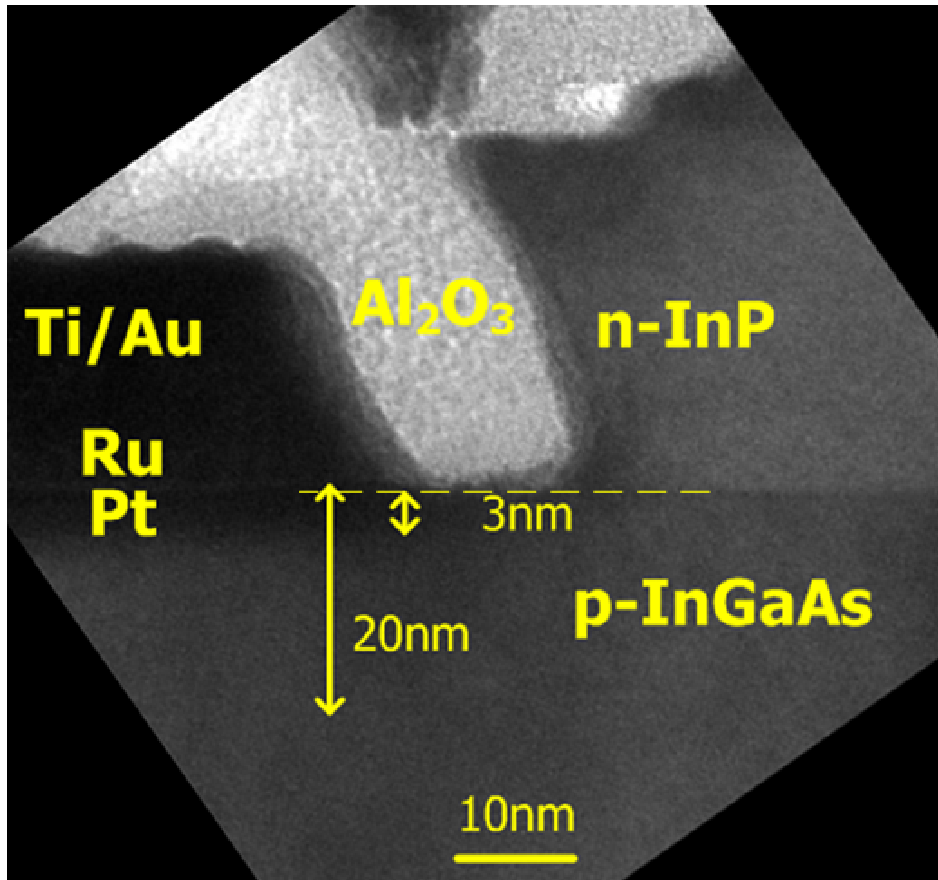

Figure 2.16: A cross-sectional TEM image shows the Pt/Ru/Ti/Au base contact. The metal sinking depth has been reduced compared to lifted-off base contact technology [7].

References

[1] V. Jain, InP DHBTs in a Refractory Emitter Process for THz Electronics.. Ph.D. Thesis, University of California, Santa Barbara, Santa. Barbara, Ca, U.S.A., 2011.

[2] Rodwell, Mark J.W.; Urteaga, M.; Mathew, T.; Scott, D.; Mensa, Dino; Lee, Q.; Guthrie, J.; Betser, Y.; Martin, S.C.; Smith, R.P.; Jaganathan, S.; Krishnan, S.; Long, S.I.; Pullela, R.; Agarwal, B.; Bhattacharya, U.; Samoska, L.; Dahlstrom, M., "Submicron scaling of HBTs," in Electron Devices, IEEE Transactions on , vol.48, no.11, pp.2606-2624, Nov 2001

[3] Jain, V.; Rodwell, Mark J.W., "Transconductance Degradation in Near-THz InP Double-Heterojunction Bipolar Transistors," in Electron Device Letters, IEEE , vol.32, no.8, pp.1068-1070, Aug. 2011. doi: 10.1109/LED.2011.2157451

[4] A. Baraskar, A. C. Gossard, and M. J. W. Rodwell, "Lower limits to metal-semiconductor contact resistance: Theoretical models and experimental data," J. Appl. Phys., vol. 114, p. 154516, Oct. 2013.

[5] J. Lin, S. Yu, and S. Mohney, "Characterization of low-resistance ohmic contacts to n-and p-type InGaAs," Journal of Applied Physics, vol. 114, no. 4, p. 044504, 2013.

[6] Rode, J.C.; Chiang, H.-W.; Choudhary, P.; Jain, V.; Thibeault, B.J.; Mitchell, W.J.; Rodwell, M.J.W.; Urteaga, M.; Loubychev, D.; Snyder, A.; Wu, Y.; Fastenau, J.M.; Liu, A.W.K., "An InGaAs/InP DHBT With Simultaneous f_t/f_{max} 404/901 GHz and 4.3 V Breakdown Voltage," in Electron Devices Society, IEEE Journal of the , vol.3, no.1, pp.54-57, Jan. 2015

[7] J. Rode, IC Fabrication Technology for Highly Scaled THz DHBTs.. Ph.D. Thesis, University of California, Santa Barbara, Santa. Barbara, Ca, U.S.A., 2015.

[8] Z. Griffith, Ultra High Speed InGaAs / InP DHBT Devices and Circuits.. Ph.D. Thesis, University of California, Santa Barbara, Santa. Barbara, Ca, U.S.A., 2005.

[9] Kirk, C.T., Jr., "A theory of transistor cutoff frequency (fT) falloff at high current densities," in Electron Devices, IRE Transactions on , vol.9, no.2, pp.164-174, March 1962

[10] T. Ishibashi, Influence of electron velocity overshoot on collector transit. times of HBTs, Electron Devices, IEEE Transactions on, vol. 37, pp. 2103. 2105, Sep. 1990.

[11] S. Laux and W. Lee, Collector signal delay in the presence of velocity overshoot, Electron Device Letters, IEEE, vol. 11, pp. 174176, Apr. 1990.

[12] Giacoletto, L.J., "Diode and transistor equivalent circuits for transient operation," in Solid-State Circuits, IEEE Journal of , vol.4, no.2, pp.80-83, Apr 1969

[13] Mason, S.J., "Power Gain in Feedback Amplifier," in Circuit Theory, Transactions of the IRE Professional Group on , vol.CT-1, no.2, pp.20-25, June 1954

[14] Full band calculations of the intrinsic lower limit of contact resistivity. Maassen, J. and Jeong, C. and Baraskar, A. and Rodwell, M. and Lundstrom, M., Applied Physics Letters, 102, 111605 (2013)

[15] M. J. W. Rodwell, M. Le, and B. Brar, “InP Bipolar ICs: Scaling Roadmaps,. Frequency Limits, Manufacturable Technologies,” Proc. IEEE, vol. 92,. pp. 271–286, Feb. 2008.

[16] H. Chiang, Design and Fabrication of Sub-100nm Base-Emitter Junctions of THz InP DHBTs.. Ph.D. Thesis, University of California, Santa Barbara, Santa Barbara, Ca, U.S.A., 2014...

[17] . Lateral carrier diffusion and current gain in terahertz InGaAs/InP double-heterojunction bipolar transistors. Chiang, Han-Wei and Rode, Johann C. and Choudhary, Prateek and Rodwell, Mark J. W., Journal of Applied Physics, 115, 034513 (2014)

[18] Lateral carrier diffusion and current gain in terahertz InGaAs/InP double-heterojunction bipolar transistors. Chiang, Han-Wei and Rode, Johann C. and Choudhary, Prateek and Rodwell, Mark J. W., Journal of Applied Physics, 115, 034513 (2014)

[19] W. Shockley and W. T. Read, Jr., Statistics of the Recombinations of Holes and Electrons, Physical Review, vol. 87, pp. 835–841, Sep. 1952.

[20] N. K. Dutta and R. J. Nelson, The case for Auger recombination in $\mathrm{In_{1-x}Ga_xAs_yP_{1-y}}$," J. Appl. Phys., vol. 53, pp. 74–92, Jan. 1982.

[21] L. A. Coldren and S. W. Corzine, Diode Lasers and Photonic Integrated Circuits.. Wiley Series in Microwave abd Optical Engineering, 1995.

[22] H. Hasegawa, "Fermi Level Pinning and Schottky Barrier Height Control at Metal-Semiconductor Interfaces of InP and Related Materials," Jpn. J. Appl. Phys., vol. 38, p. 10981102, Feb. 1999.

[23] C. L. Hinkle, M. Milojevic, B. Brennan, A. M. Sonnet, F. S. Aguirre-Tostado, G. J. Hughes, E. M. Vogel, and R. M. Wallace, "Detection of Ga suboxides and their impact on III-V passivation and Fermi-level pinning," Appl. Phys. Lett., vol. 94, p. 162101, Apr. 2009.

[24] V. Chobpattana, J. Son, J. J. M. Law, R. Engel-Herbert, C. Y. Huang, and S. Stemmer, "Nitrogen-passivated dielectric/InGaAs interfaces with sub-nm equivalent oxide thickness and low interface trap densities," Appl. Phys. Lett., vol. 102, pp. 022907–1–022907–3, Jan. 2013.

[25] E. F. Chor, W. K. Chong, and C. H. Heng, "Alternative (Pd,Ti,Au) contacts to (Pt,Ti,Au) contacts for $In_{0.53}Ga_{0.47}As$," J. Appl. Phys., vol. 84, pp. 2977–2979, Sep. 1998.

[26] Jain, V.; Rode, J.C.; Han-Wei Chiang; Baraskar, A.; Lobisser, E.; Thibeault, Brian J.; Rodwell, M.; Urteaga, M.; Loubychev, D.; Snyder, A.; Wu, Y.; Fastenau, J.M.; Liu, W.K., "1.0 THz fmax InP DHBTs in a refractory emitter and self-aligned base process for reduced base access resistance," in Device Research Conference (DRC), 2011 69th Annual , vol., no., pp.271-272, 20-22 June 2011

[27] Chor, E.F.; Malik, R.J.; Hamm, R.A.; Ryan, R., "Metallurgical stability of ohmic contacts on thin base InP/InGaAs/InP HBT's," in Electron Device Letters, IEEE , vol.17, no.2, pp.62-64, Feb. 1996

[28] Ultralow resistance, nonalloyed Ohmic contacts to n-InGaAs Baraskar, Ashish K. and Wistey, Mark A. and Jain, Vibhor and Singisetti, Uttam and Burek, Greg and Thibeault, Brian J. and Lee, Yong Ju and Gossard, Arthur C. and Rodwell, Mark J. W., Journal of Vacuum Science and Technology B, 27, 2036-2039 (2009)

Chapter 3

RF HBT Improvements

Next generation HBTs require improved process flows for further lateral scaling of device dimensions, lower base contact resistivities, and higher β. This chapter discusses work that has been done to improve the mentioned parameters. Improved epitaxial designs for higher emitter current density J_{E} and process flow improvements for reduced thermal shock and increased yield are also discussed.

3.1 Reducing Thermal Shock For Improved Yield

As emitter widths are scaled to 100 nm, the high aspect ratio emitter metal stack becomes sensitive to physical stress that is induced during fabrication. Shear stress is introduced when the device is planarized using benzocyclobutene (BCB). Figure 3.1 shows a cross-sectional TEM of an HBT where the emitter semiconductor is cracking due to the added stress.

To increase structural support to the emitter metal stack, a 30 nm SiN layer was deposited via Plasma Enhanced Chemical Vapour Deposition (PECVD) prior

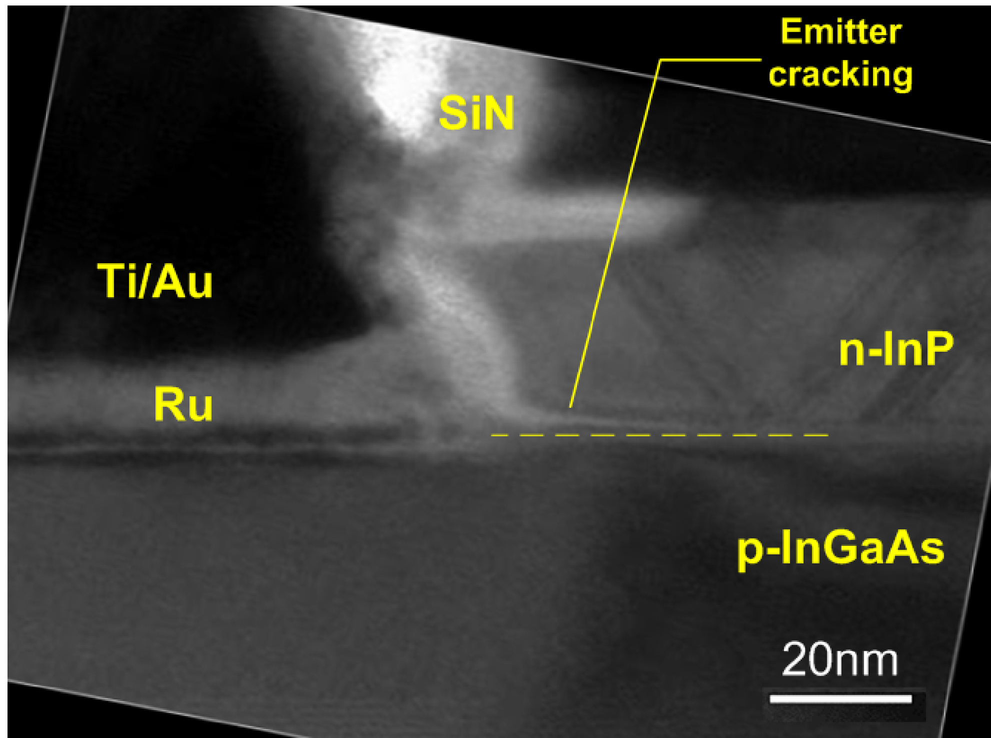

Figure 3.1: A cross-sectional TEM image of HBT61B. The semiconductor at the InP/InGaAs emitter-base boundary is cracked due to strain. *(Courtesy: Han-Wei Chiang)*

to BCB planarization [1]. An anchoring layer is also required for supporting the exposed emitter, base, and collector metal after planarization. However, PECVD SiN is deposited at 250°C which introduces further stress in the BCB as its coefficient of expansion is different from InP. A low temperature sputtered SiN recipe was developed, to anchor the device post planarization. The anchor is visible in the cross-sectional TEM image in Figure 2.6, and the process flow is illustrated in Figure 3.2.

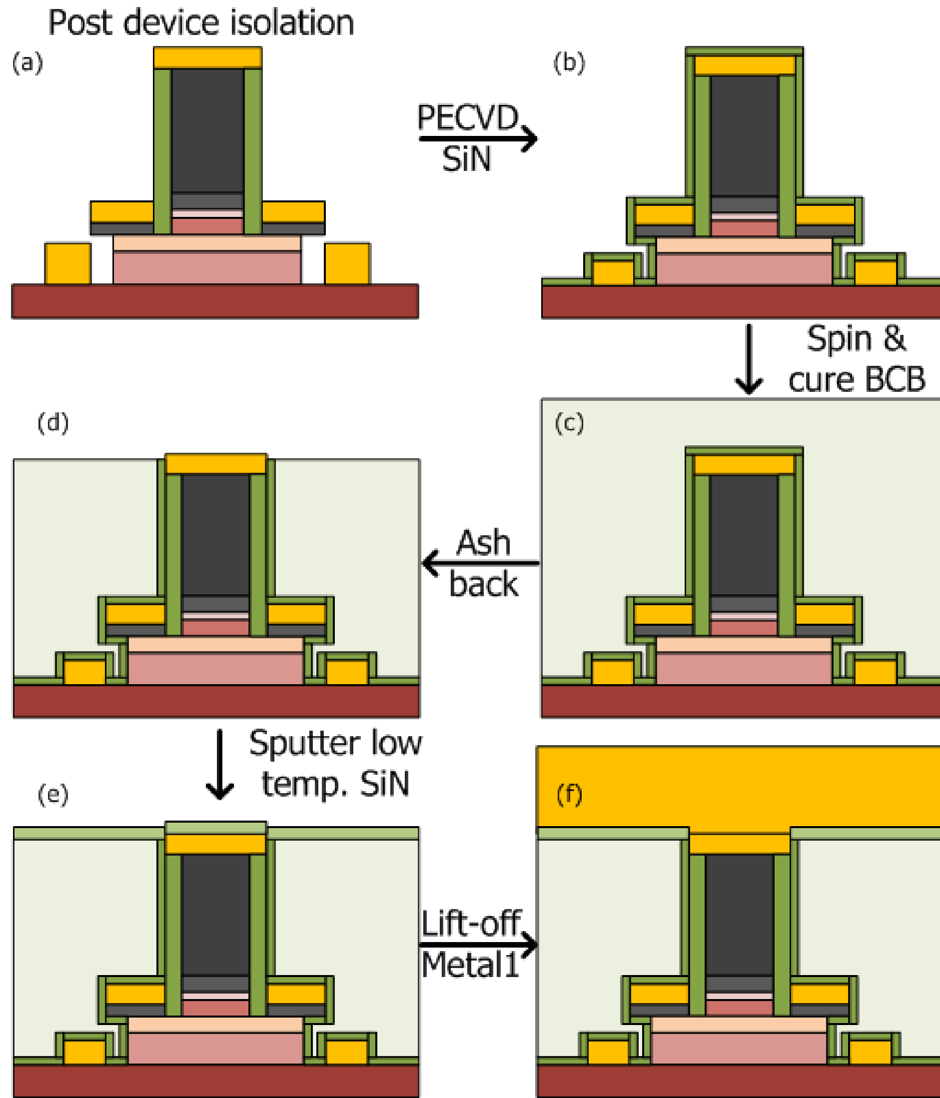

Figure 3.2: Process flow incorporating the low temperature SiN anchor to provide structural stability. Steps (c) and (f) introduce strain on the high aspect ratio emitter metal as BCB and InP/W have different coefficients of thermal expansion.

3.2 Blanket Iridium Base Contacts

Refractory metal base contacts have the advantage of low base contact resistivity as well as minimal metal sinking depth [2] [3] (Section 2.4.2). It has been

shown on test structures previously that Iridium contacts to p-InGaAs yield sub-$\Omega.\mu m^2$ contact resistivity at a doping of $2{*}10^{20} cm^{-3}$ [3]. This section shows a process flow that was developed for integrating Ir base contacts into an RF HBT process.

The process for a refractory base contact metal requires blanket metal deposition, and it must be etched away from the field prior to base mesa wet etch. Iridium is the most corrosion resistant metal known [4], and thus requires a high power SF_6/Ar plasma etch to remove it from the field. Since this would also attack the emitter metal and gap region between emitter and base metal, it is important to protect them during etch. Figure 3.3 shows an angled SEM image of HBT emitter metal and test structures that have been etched away due to incomplete protection.

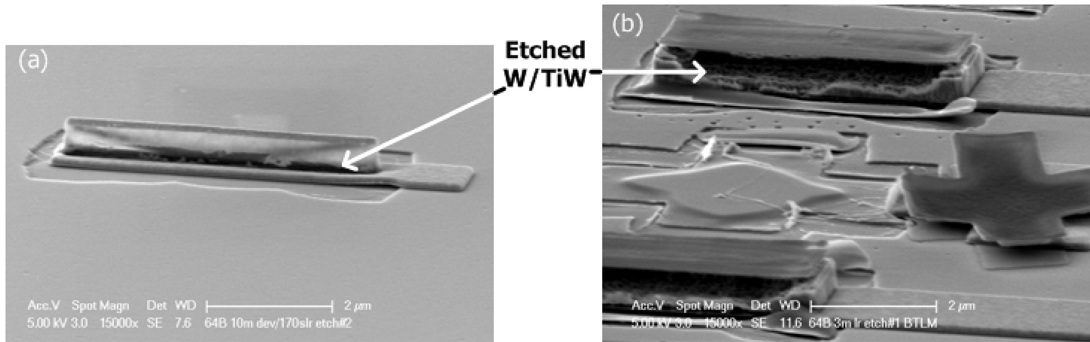

Figure 3.3: Angled SEM image of sample after Ir dry etch. The W/TiW emitter metal has been etched due to insufficient protection during the etch. (a) Emitter (b) Vernier test structures.

A dual sidewall process was developed, where blanket Al_2O_3 was deposited via Atomic Layer Deposition (ALD) followed by blanket SiN via PECVD. The SiN was subsequently etched using a CF_4/O_2 anisotropic dry etch to form a SiN sidewall and the Al_2O_3 was wet etched using dilute HF to expose the Ir. The

active device was then protected by resist via electron-beam lithography, and the field was dry etched using SF_6/Ar to expose the p-InGaAs. Figure 3.4 shows a cross-sectional SEM of a test HBT structure after blanket Ir etch.

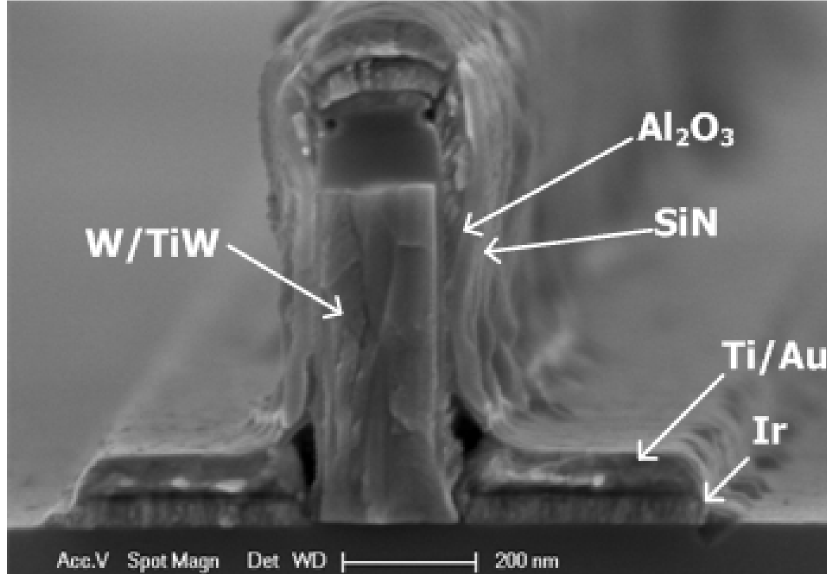

Figure 3.4: Cross-sectional SEM image of test HBT structure after Ir dry etch. The Al_2O_3/SiN composite sidewall protects the W/TiW emitter metal.

3.3 Epitaxial Design For $J_{\mathrm{E}} > 40mA/\mu m^2$

The emitter current density J_{E} scales proportionally with the $f_{\mathrm{t}}/f_{\mathrm{max}}$ requirements of HBTs, as mentioned in section 2.2. The emitter and collector epitaxial design must be revised for each generation so that they may support the increased current densities without suffering from space-charge screening effects such as Kirk or emitter starvation [5].

With increasing J_{E}, the electric field in the space-charge region decreases and eventually reverses which moves the injection point of electrons further into the

emitter as shown in Figure 2.7. This increases the effective base width w_{B}, and also decreases J_{E} as $(\triangle E_{\mathrm{Fn}} - \triangle E_{\mathrm{C}})$ at the injection point goes down.

J_{E} is determined by the position of the electron fermi level at the injection point i.e. at the InP/InGaAs emitter-base heterojunction. The electron current density can be computed as a function of the fermi level and assuming fermi velocity as [6] [7] [8] [9]:

$$J = \frac{qm^*}{2\pi^2\hbar^3}\int_0^\infty E.f(E)dE \tag{3.1}$$

There is also a finite transmission probability for electrons at the heterojunction which reduces J_{E}. [10] incorporates this and this is shown in Figure 3.5.

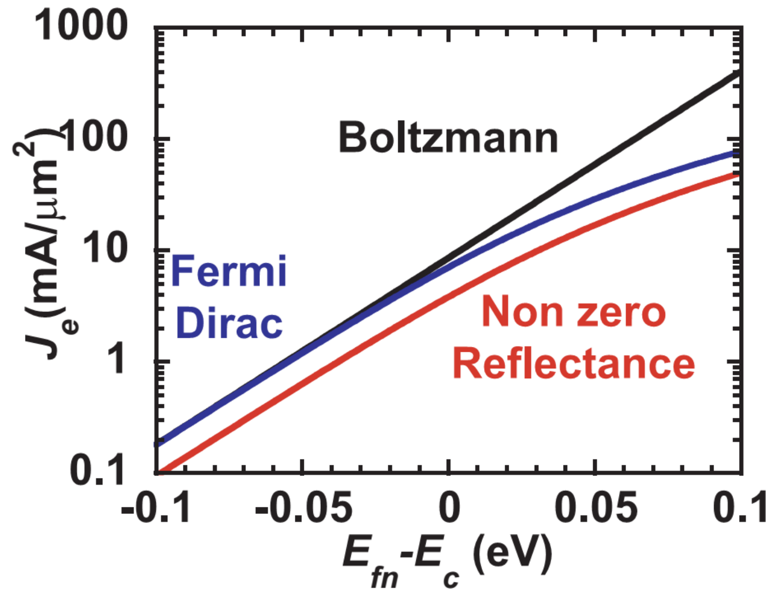

Figure 3.5: Calculated J_{E} as a function of electron Fermi Level (E_{fn}) position relative to conduction band edge (E_{C}) for InP emitter for Boltzmann approximation, FermiDirac distribution function and including a non-zero electron flux reflectance at the heterointerface [10]

The drop in $E_{\mathrm{fn}} - E_{\mathrm{C}}$ along the emitter space-charge region reduces electron

state density, and thus the space charge region must be optimized to reduce this barrier. Based on Figure 3.5, an emitter current density of 40 mA/μ^2 requires the electron Fermi level E_{fn} to be ≈0.85eV above the conduction band. The emitter epitaxial design shown in Table 3.1 is designed for a maximum emitter current density of 50 mA/μm^2.

Layer	Semiconductor	Old/**New** Thickness (Å)	Old/**New** Doping (cm^{-3})
Emitter cap	$In_{0.53}Ga_{0.47}As$	100/**100**	8/**8**×10^{19}:Si
Emitter	InP	150/**80**	4/**4**×10^{19}:Si
Emitter	InP	150/**50**	3/**7**×10^{19}:Si

Table 3.1: Optimized emitter epi design for J_{E} of 50 mA/μm^2

The above analysis assumes zero change in the electron Fermi level E_{fn} along the space-charge region and also neglects barrier modulation effects [10]. Thus, the maximum available J_{E} may be lower.

It is important to note that this reduces the thickness of the InP layers, thus the hole diffusion current from base to emitter is expected to increase due to a steeper diffusion profile.

3.4 Reducing Auger Recombination

As discussed in section 2.3.2, Auger recombination in the base starts to be a larger portion of the base current as the base doping increases, thus reducing β. While the base doping must be lowered to reduce Auger recombination, it must be high enough at the surface to yield low $R_{\mathrm{b,contact}}$ and have a low $R_{\mathrm{b,sh}}$. [5] suggests using a highly doped pulse layer at the emitter-base junction (Figure 3.6) which reduces $R_{\mathrm{b,contact}}$ while maintaining low Auger recombination in the remainder of

the base semiconductor.

However, there exists no quasi-electric field in the pulse doped layer, which increases the base transit time τ_b and net Auger recombination as the electron density in the pulse region is higher than it would be if a quasi-electric field was present.

A new dual-grade base design is proposed where the top 5 nm of the base employs a doping grade such that the base contact resistivity is low for a contact that sinks <5 nm. The second doping grade has a lower doping to lower Auger recombination. Since the pulse doping is replaced by a doping grade, the electrons traverse the region faster, reducing net Auger recombination.

Figure 3.6 shows the doping design. Figure 3.7 plots the Auger recombination rate along the base for both the pulse and dual grade designs. A dual grade reduces net Auger recombination. This analysis assumes a constant electron current throughout the base. Values are based on extracted electron saturation velocity and Auger coefficients and are used as a qualitative tool only [11] [5].

3.5 Atomic Layer Deposition of Emitter Metal

The emitter width w_E is often used as a metric for HBT technology nodes as it is the smallest lithographic feature in an HBT process flow. The emitter capacitance (C_{je}, C_{be})) must be decreased and J_E increased in order to increase f_t, and consequently f_{max}. The emitter metal aspect ratio must be large to minimize parasitic capacitances between the the device and metal layers, and must also have a steep vertical profile to allow self-aligned deposition of base contacts for

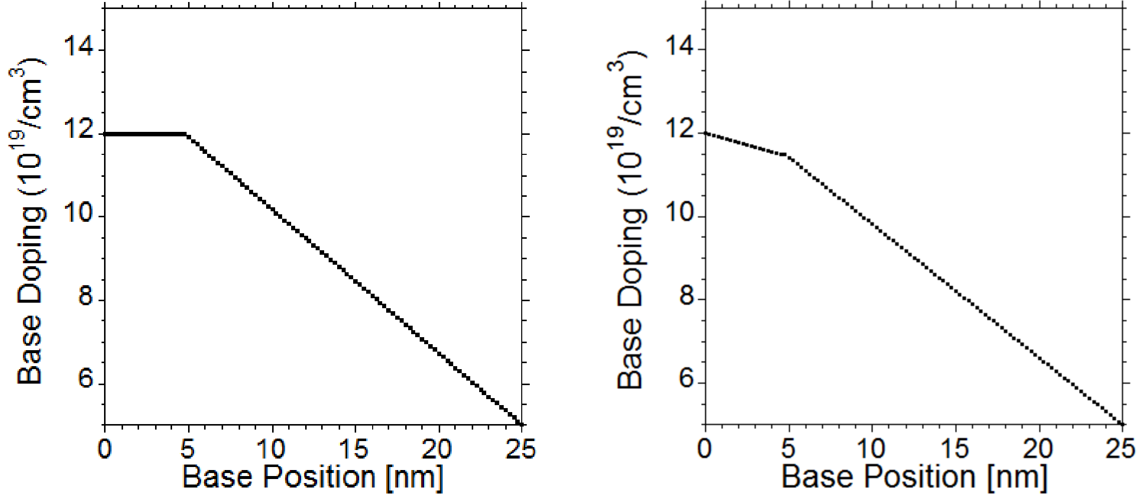

Figure 3.6: (Left) Pulse layer + doping grade profile in the base for low $R_{\text{Base,cont.}}$ [5]. (Right) Dual doping grade profile in the base maintains high doping under base contact for low $R_{\text{Base,cont.}}$, but also introduces $\triangle E_{\text{C}}$ in high doping regions to accelerate electrons away and reduce Auger recombination.

minimal $R_{\text{b,gap}}$.

The existing emitter technology at UCSB for w_{E}=100 nm uses a blanket sputtered refractory metal process, where blanket W/TiW layers are deposited. The emitter region is protected and the metal is etched away in the field [5] [12] [1] (Appendix B). This process benefits from using refractory metals as the emitter metal can now handle large current densities. The vertical etch employed to define the emitter metal is not perfectly anisotropic, and laterally etches the emitter metal as well. Due to this, the fabricated emitter width w_{E} does not match the designed emitter width $w_{\text{E,design}}$ such that: [12]:

$$w_{\text{E}} = w_{\text{E,design}} \pm 30nm \tag{3.2}$$

While this is acceptable for a 100 nm wide emitter, it is not possible to use this

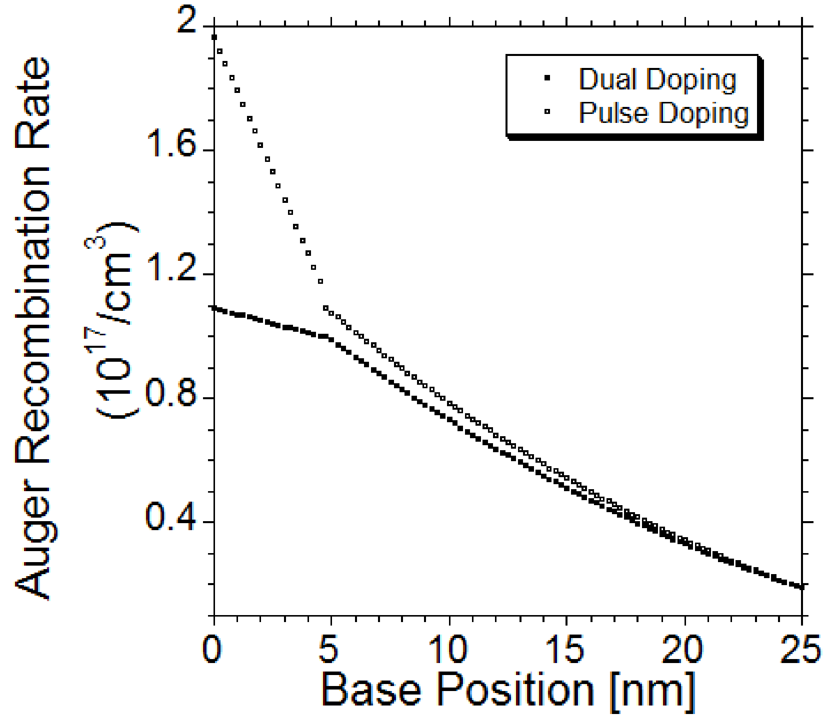

Figure 3.7: Auger recombination for dual doping grade and pulse doping base designs, plotted as a function of base depth.

technology for the 60 nm node. A 30 nm variation in emitter width would degrade the emitter metal structural integrity, and cause a large variation in emitter access resistance R_{ex}. Figure 3.8 depicts the problem as the W/TiW emitter process is scaled to smaller emitter widths [12].

A new process flow is shown in Figure 3.9 which allows for high aspect ratio emitter metal with $w_{\mathrm{E}} \leq 100nm$, and supports high J_{E}. A refractory metal emitter contact is deposited via e-beam deposition, the metal is capped using ALD Al_2O_3 and a thick polycrystalline Si film is sputtered on top. The emitter is patterned on top of the Si using positive electron beam resist, and the Si is etched away using a Bosch Deep Si RIE tool. The Al_2O_3 is wet etched away and a blanket

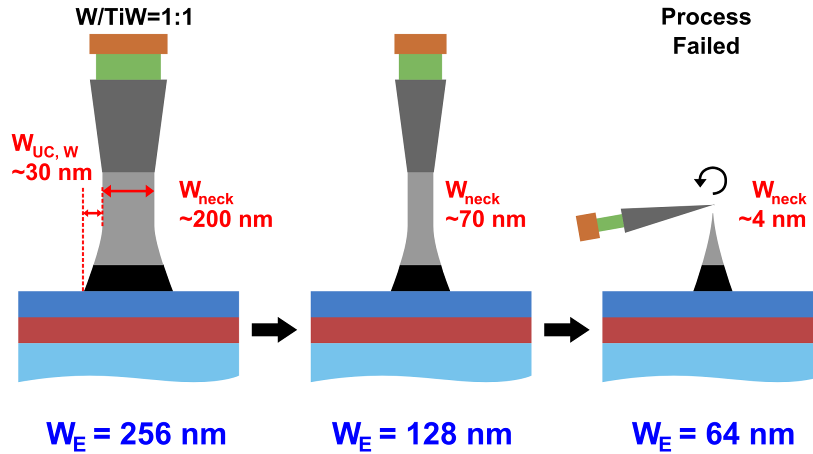

Figure 3.8: Schematics of 256, 128, and 64nm wide emitter metal stacks after emitter metal dry etch. [12]

layer of refractory metal is deposited using ALD. The deposition is conformal due to ALD, and fills the trench completely due to the vertical etch profile. The metal and Si layers are then blanket etched away to leave standing emitter metal. The refractory contact metal is then etched away and a SiN sidewall is deposited for structural support.

ALD TiN was used for developing the process flow, due to its high melting point. Pt and Ru ALD films were also explored, and are discussed in the next section.

3.5.1 ALD Emitter Challenges

The aspect ratio and vertical profile of the emitter is dependent on the Si etch profile. The Bosch Si Deep RIE etcher uses $SF_6/C_2F_8/Ar$ chemistry to obtain high aspect ratio trenches. C_2F_8 polymerizes the Si which reduces the etch rate. SF_6/Ar etches the Si, as well as the Si polymer. Since this is an anisotropic dry

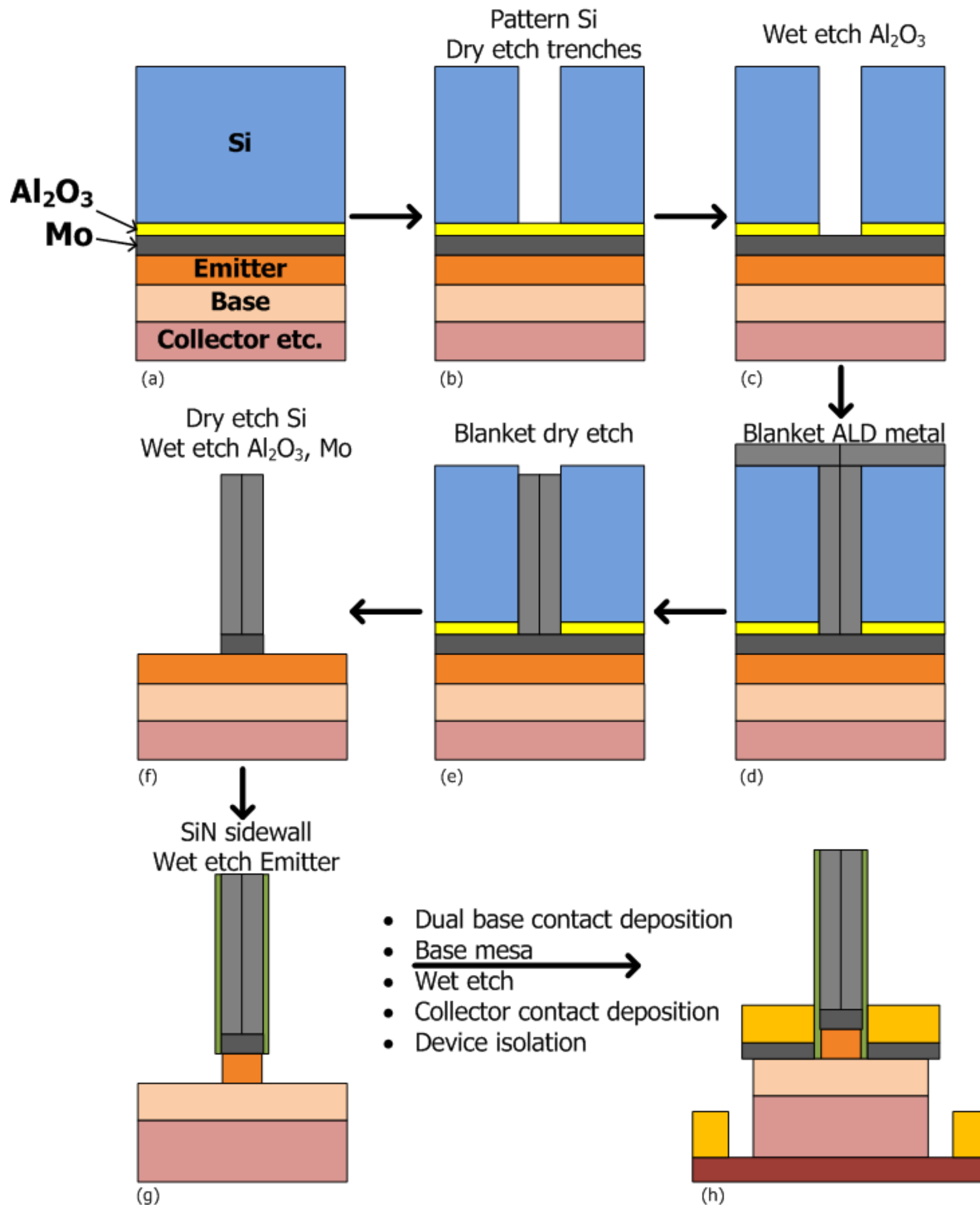

Figure 3.9: Process flow for fabricating emitter metal via ALD deposition. HBT fabrication steps after (g) are identical to W/TiW emitter HBT process flow shown in Appendix B.

etch, the SF_6/Ar etches the bottom more than the sides. Thus, the DRIE can be used to obtain highly vertical trenches at high aspect ratio.

As the emitter width is scaled, the etch rate slows down non-linearly due to gas and etch by-product loading effects. Figure 3.10 shows two trenches of different emitter width on the same sample. The narrower trench shows a much lower etch rate. This is problematic as the etch mask is no longer sufficient for a longer dry etch. An ALD alumina hard mask was employed to enable longer DRIE etching times.

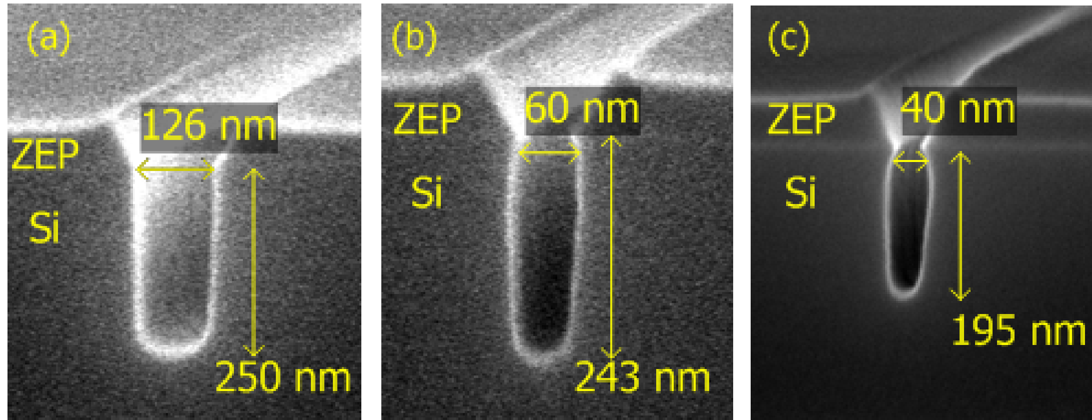

Figure 3.10: Cross-sectional SEM images of Si trenches on the same die. The etch rate/depth decreases as the trench width shrinks due to loading effects.

Furthermore, the sidewall profile for <50nm width trenches bows outwards (Figure 3.11).

The etch rate was increased by decreasing the C_2F_8 flow to decrease polymerization, and increasing SF_6/Ar flow for increased etch rate. It was discovered that the etch rate for <70nm trenches decreases as a function of etch time. A uniform etch rate w.r.t. etch time was observed by splitting the etch into 2 min etches, and purging the chamber between etches. This confirms the hypothesis that >70nm trenches suffer from excessive gas and etch byproduct loading effects. Optimizing the gas ratios and splitting etch times yields vertical, high aspect ratio trench

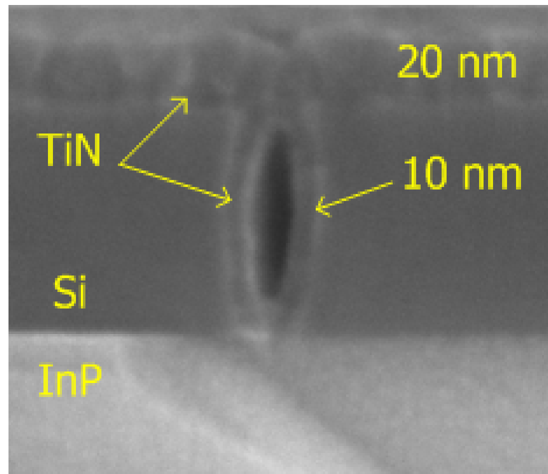

Figure 3.11: Cross-sectional SEM images of Si trenches that bows outwards in the middle. This leads to a hollow 'teardrop' when ALD TiN is deposited. The deposited TiN film thickness in the trench is nearly half of the thickness in the field.

profiles as shown in Figure 3.12.

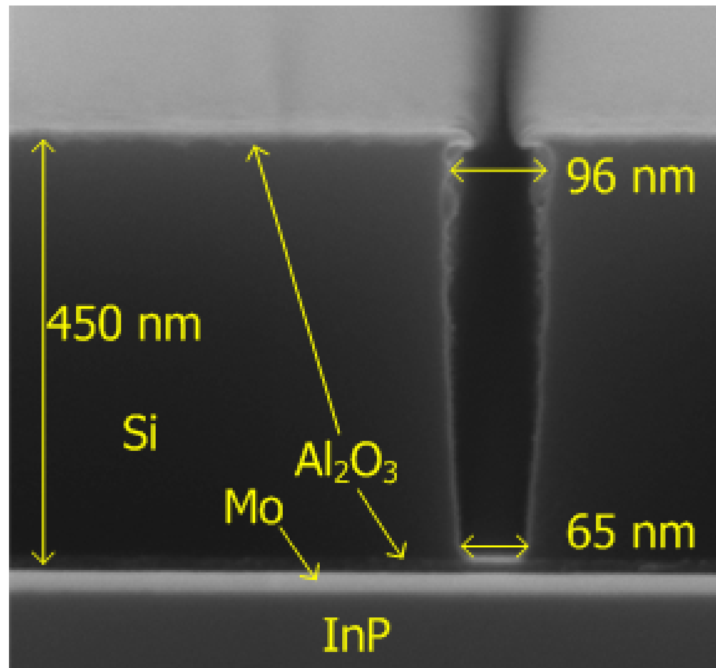

Figure 3.12: Cross-sectional SEM images of 70nm wide high aspect ratio Si trenches.

Initial tests with ALD metal deposition yielded incomplete fill-in as shown in Figure 3.13. The precursor molecule mean free path in vacuum is large enough that fewer molecules access all parts of the trench. Thus, the deposition rate inside the trench is lower.

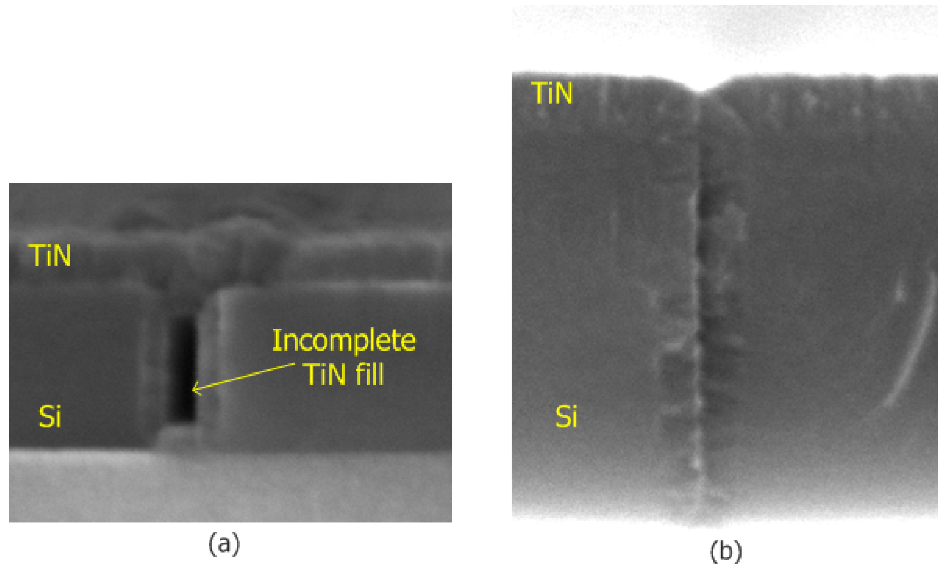

Figure 3.13: Cross-sectional SEM images Si trenches after blanket ALD TiN deposition. (a) TiN deposition rate inside the trench is lower due to large precursor mean free path. (b) Complete fill-in due to dose and soak process.

Increasing precursor dose time and "soaking" it in the chamber for 10 seconds after dose led to perfectly conformal deposition. This shows that the ALD precursors were initially unable to coat the inside of the trench due to its high aspect ratio and small width.

TiN was initially used as it can be deposited via ALD, has high electrical conductivity and melting point. However, the resistivity of films deposited in the UCSB cleanroom was 1200 $\Omega.nm$. The emitter metal resistivity must be >400 $\Omega.nm$ for metal access resistance to be below 1 Ω.

ALD Pt was explored as an alternative due to its low resistivity of 40 $\Omega.nm$, and was successfully deposited on test structures. However, the blanket Si dry etch also etches Pt. Figure 3.14 shows an angled SEM image of a Pt emitter after the Si has been etched away in the field. A portion of the emitter has been protected by Ti/Au and thus the full emitter cross-section is visible under it. However, emitter metal outside of the capped region has been etched.

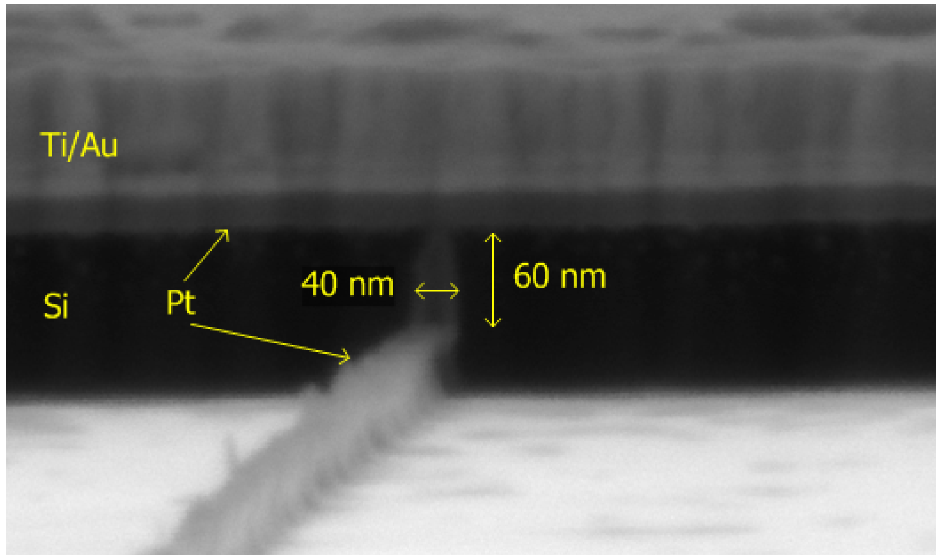

Figure 3.14: Angled SEM image of Pt emitter after blanket Si etch. The emitter region exposed to Si etch has been attacked.

ALD Ru is reported to have low resistivity of $60\Omega.nm$ [14], is etch resistant and also has a high melting point. However, we were unable to develop this process at UCSB as Ru requires chamber pressure of >750mT for precursor adhesion and subsequent seed layer formation. The Oxford Instruments FlexAL Atomic Layer Deposition system at UCSB is designed for a maximum chamber pressure of 250mT only.

3.5.2 ALD Emitter Preliminary Results

ALD based emitters were successfully fabricated on test structures using TiN and is shown in Figure 3.15. RF HBTs using TiN ALD emitters were also fabricated. However, the emitter terminal was open in electrical measurements. TiN forms an oxide layer which is was not etched prior to base metal deposition, and this is suspected as the cause for open contacts.

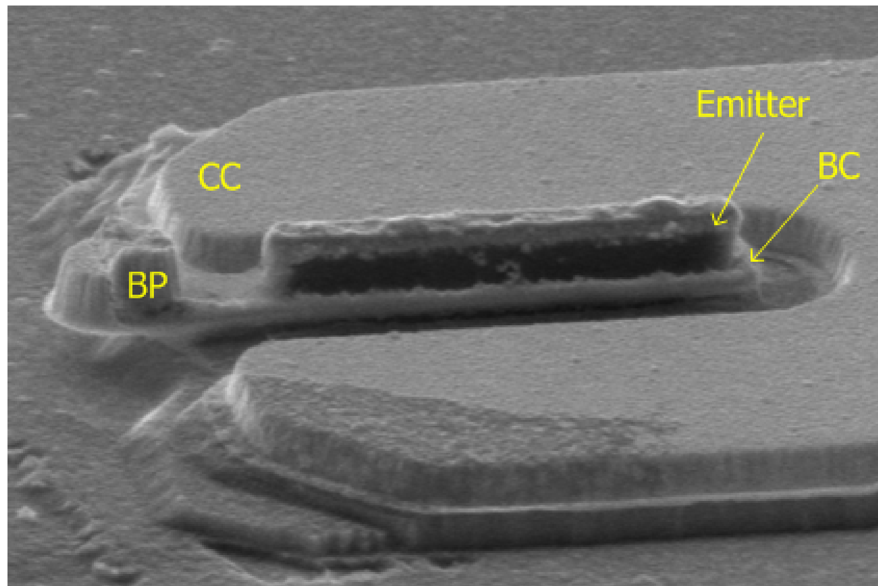

Figure 3.15: Angled SEM image an ALD Emitter based HBT after device isolation. The base post (BP), collector contact (CC), base contact (BC), and emitter metal are marked.

References

[1] J. Rode, IC Fabrication Technology for Highly Scaled THz DHBTs.. Ph.D. Thesis, University of California, Santa Barbara, Santa. Barbara, Ca, U.S.A., 2015.

[2] Ultralow resistance, nonalloyed Ohmic contacts to n-InGaAs Baraskar, Ashish K. and Wistey, Mark A. and Jain, Vibhor and Singisetti, Uttam and Burek, Greg and Thibeault, Brian J. and Lee, Yong Ju and Gossard, Arthur C. and Rodwell, Mark J. W., Journal of Vacuum Science and Technology B, 27, 2036-2039 (2009)

[3] A. Baraskar, A. C. Gossard, and M. J. W. Rodwell, “Lower limits to metal-semiconductor contact resistance: Theoretical models and experimental data,” J. Appl. Phys., vol. 114, p. 154516, Oct. 2013.

[4] Emsley, J. (2003). ”Iridium”. Nature’s Building Blocks: An AZ Guide to the Elements. Oxford, England, UK: Oxford University Press. pp. 201204. ISBN 0-19-850340-7

[5] V. Jain, InP DHBTs in a Refractory Emitter Process for THz Electronics.. Ph.D. Thesis, University of California, Santa Barbara, Santa. Barbara, Ca, U.S.A., 2011.

[6] M. J. W. Rodwell, M. Le, and B. Brar, “InP Bipolar ICs: Scaling Roadmaps,. Frequency Limits, Manufacturable Technologies,” Proc. IEEE, vol. 92,. pp. 271–286, Feb. 2008.

[7] C. Chang and S. Sze, Carrier transport across metal-semiconductor barriers, Solid-State Electronics, vol. 13, no. 6, pp. 727740, 1970.

[8] N. Machida, Y. Miyamoto, and K. Furuya, Charging time of double-layer. emitter in heterojunction bipolar transistor based on transmission formalism, Japanese Journal of Applied Physics, vol. 45, no. 35, pp. L935L937,. 2006.

[9] N. Machida, Y. Miyamoto, and K. Furuya, Minimum emitter charging time. for heterojunction bipolar transistors, in Indium Phosphide and Related Materials Conference Proceedings, 2006 International Conference on, pp. 325. 328, 2006.

[10] Jain, V.; Rodwell, Mark J.W., ”Transconductance Degradation in Near-THz InP Double-Heterojunction Bipolar Transistors,” in Electron Device Letters, IEEE , vol.32, no.8, pp.1068-1070, Aug. 2011. doi: 10.1109/LED.2011.2157451

[11] A comparison of minority electron transport in In0.53Ga0.47As and GaAs. Kaneto, T. and Kim, K. W. and Littlejohn, M. A., Applied Physics Letters, 63, 48-50 (1993)

[12] H. Chiang, Design and Fabrication of Sub-100nm Base-Emitter Junctions of THz InP DHBTs.. Ph.D. Thesis, University of California, Santa Barbara, Santa Barbara, Ca, U.S.A., 2014...

[13] . Lateral carrier diffusion and current gain in terahertz InGaAs/InP double-heterojunction bipolar transistors. Chiang, Han-Wei and Rode, Johann C. and Choudhary, Prateek and Rodwell, Mark J. W., Journal of Applied Physics, 115, 034513 (2014)

[14] Aaltonen, T., Aln, P., Ritala, M. and Leskel, M. (2003), Ruthenium Thin Films Grown by Atomic Layer Deposition. Chem. Vap. Deposition, 9: 4549. doi: 10.1002/cvde.200290007

Chapter 4

MOCVD Emitter Regrowth

As discussed in section 2.2, the DC current gain β decreases as HBTs are scaled for higher cutoff frequencies. The primary reason for β drop are an increase in $\frac{I_{\mathrm{B,edge}}}{I_{\mathrm{B}}}$ with w_{E} scaling, and an increase in $\frac{I_{\mathrm{B,Auger}}}{I_{\mathrm{B}}}$ with higher base doping as mentioned in section 2.3. Alternative base designs have been explored for mitigating Auger recombination (Section 3.4) but it is expected to remain a concern as high base doping is essential for low R_{bb}.

This chapter proposes a new HBT structure that aims to reduce $\frac{I_{\mathrm{B,edge}}}{I_{\mathrm{B}}}$ and $\frac{I_{\mathrm{B,Auger}}}{I_{\mathrm{B}}}$ for RF HBTs, and increase cutoff frequency by reducing τ_{b}. Theoretical calculations for improved HBT characteristics are presented, and selective regrowth of the emitter semiconductor via MOCVD is proposed as a viable technology.

4.1 Device Structure

The proposed device structure is shown in Figure 4.1 where the p-InGaAs region under the base metal contact is decoupled from the p-InGaAs region under

the emitter-base junction. The base region under the base metal contact is called the "extrinsic base". It can be highly doped for low $R_{\mathrm{b,contact}}$ without increasing Auger recombination, and can also be made thicker than the base metal contact sinking depth (5nm) so that it is no longer an issue. The base region under the emitter-base junction is known as the "intrinsic base". Such a structure is employed in SiGe BICMOS HBTs where the SiGe based intrinsic and extrinsic base, and Si emitter semiconductor is regrown [1].

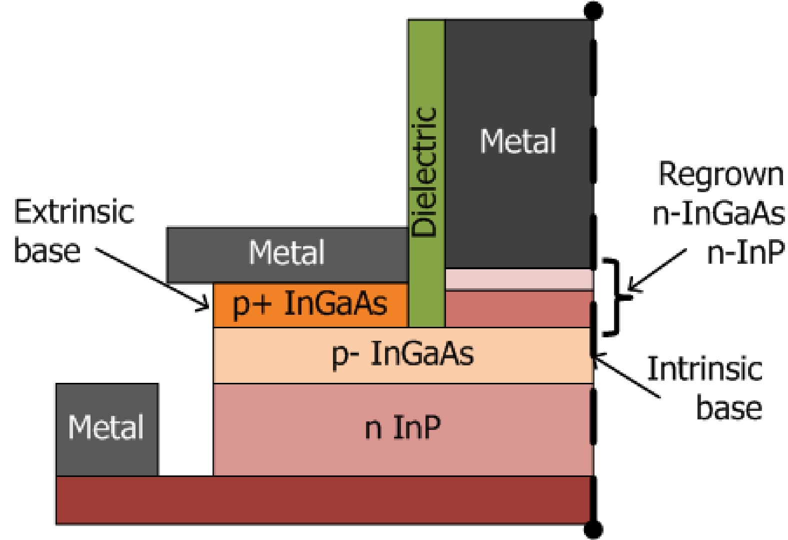

Figure 4.1: Cross-sectional schematic of an emitter regrowth structure.

Table 4.1 shows three potential extrinsic and intrinsic base designs for an emitter regrown HBT. The following sections in this chapter will compare the benefits of each of these designs in terms of β and cutoff frequency. The emitter and collector design is assumed to be identical to a non-regrowth HBT, as discussed in section 2.1.

Figure 4.2 shows a simplified RC network in the base-collector region. Note that a conventional HBT structure denotes lateral base resistance as $R_{\mathrm{b,sh}}$, but

Layer	Semiconductor	Thickness (Å)	p-Doping ($10^{19} cm^{-3}$)		
			A	B	C
Extrinsic Base	$In_{0.53}Ga_{0.47}As$	80	14-11	14	14
Intrinsic Base	$In_{0.53}Ga_{0.47}As$	120	9-5	9-5	7

Table 4.1: Potential epi design of the extrinsic and intrinsic base in an RF HBT with regrown emitter.

in a regrowth structure the lateral resistance must be broken down in to intrinsic and extrinsic base lateral sheet resistance $R_{\mathrm{b,intr,sh}}$ and $R_{\mathrm{b,extr,sh}}$ respectively.

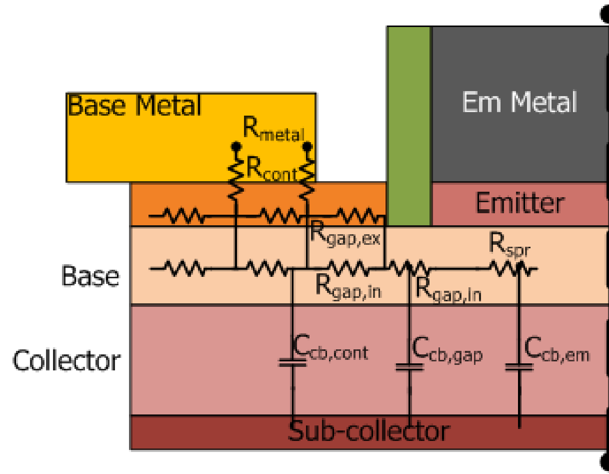

Figure 4.2: Simplified distributed RC network in the base-collector region. The base gap resistance is a function of the intrinsic as well as extrinsic base sheet resistance.

A simplified form for the lateral base resistance can be written as:

$$R_{\mathrm{b,lateral}} = \rho_{\mathrm{b,intr,sh}} \frac{w_{\mathrm{E}}}{12 L_{\mathrm{E}}} + \rho_{\mathrm{b,sh}} \frac{w_{\mathrm{gap}}}{2 L_{\mathrm{E}}} \tag{4.1}$$

where $\rho_{\mathrm{b,sh}}$ is $\rho_{\mathrm{b,intr,sh}}$ and $\rho_{\mathrm{b,extr,sh}}$ in parallel. This implies that as w_{E} is scaled, the first term in equation 4.1 becomes negligible and thus the doping in the intrinsic base can be lowered without significant penalty. This serves to reduce Auger recombination in the base.

4.2 Base Diffusion Current ($I_{\mathrm{b,diff}}$) Suppression

As discussed in section 2.3, the base diffusion current $I_{\mathrm{b,diff}}$ consists of electrons diffusing from the emitter-base junction towards the base contact metal.

Figure 4.3 shows the band diagram for a regrowth HBT in the direction XX', which is the path taken by electrons diffusing towards the base contact. There now exists a barrier $\triangle E_{\mathrm{B}}$ in the conduction band for electrons diffusing from the base-emitter junction to the base metal. The edge electron diffusion current would reduce according to 4.2.

$$I_{\mathrm{b,diff}} \propto \exp \triangle E_{\mathrm{B}} \tag{4.2}$$

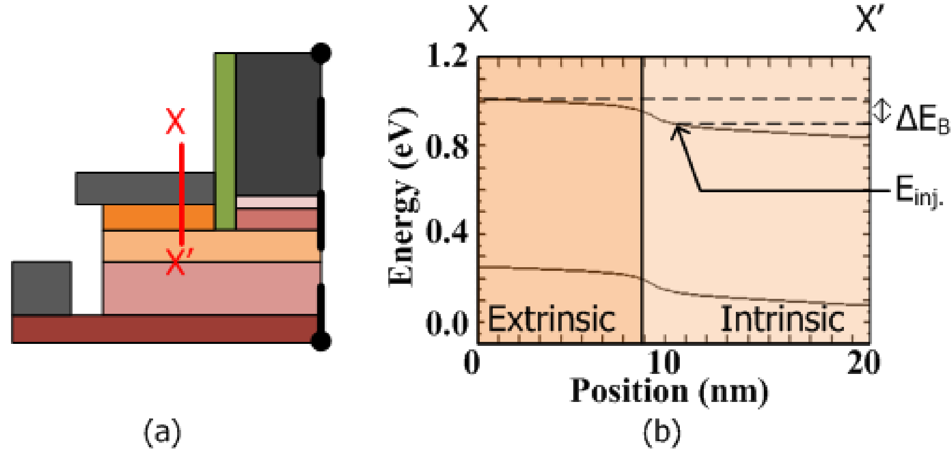

Figure 4.3: (a) Electrons scatter at the base-emitter junction and diffuse towards the base metal in the direction XX'. (b) Band diagram shows that electrons diffusing from emitter-base junction -at energy E_{inj}- encounter an energy barrier $\triangle E_{\mathrm{B}}$ in diffusing towards the base metal, thus reducing $I_{\mathrm{B,diff}}$.

Figure 4.2 compares the conduction band barrier for each of the three regrowth designs. The presence of a doping grade in design A induces an additional quasi-

electric field $\vec{\varepsilon}_{\text{Quasi}}$ that inhibits electron transport to the base contact.

Design	Energy Barrier (meV)	$\vec{\varepsilon}_{\text{Quasi}}$
A	53	3.7×10^4
B	53	-
C	78	-

Table 4.2: Energy barrier and quasi-electric field $\vec{\varepsilon}_{\text{Quasi}}$ that suppress $I_{\text{b,diff}}$ in each of the proposed regrowth base designs.

4.3 Reduction Of Auger Recombination In The Base

Auger recombination occurs in the intrinsic base as electrons travel from the emitter-base junction towards the base-collector. In the regrowth structure, the intrinsic base doping can be lower than the doping in a conventional HBT structure, because the base metal contact is now contacting the extrinsic base instead.

The Auger recombination profile along the intrinsic base can be calculated for each of the proposed designs, similar to section 3.4.

4.4 Increase in f_{t}

For a regrowth structure, the lateral base sheet resistance needs to be considered separately under the emitter-base junction and under the extrinsic base region. As the thickness and doping of the extrinsic base are largely determined by process considerations, it can be made thicker and with high doping. As shown

in 4.1, this allows for the intrinsic base doping and thickness to be reduced and the unity-gain cut-off frequency f_t to be increased.

Table 4.3 shows multiple regrowth epi designs at 100 nm w_E and compares their respective f_t, f_{max} using equations 2.15 and 2.16. The base access resistance R_{bb} is computed using 2.8 for conventional HBTs, and modified according to section 4.1 for regrowth HBTs. All resistance, and capacitance values are taken from values extracted from RF HBTs fabricated at UCSB [2]. A detailed list of variables and their values can be found in Appendix A.

Design	$R_{b,spread}(\Omega)$	$R_{b,gap}(\Omega)$	$R_{b,contact}(\Omega)$	$\tau_b(fs)$	f_t (GHz)	f_{max} (GHz)
A	8.6	4.2	24.5	48	577	1379
B	7.75	3.9	24.2	48	577	1406
C	7.75	3.9	24.2	48	577	1406
HBT64C	4.8	4.3	24.6	80	517	1374

Table 4.3: Base access resistance comparison for the proposed regrowth designs, compared with a non-regrowth device HBT 64C fabricated at UCSB with a 20nm base [2]. Emitter width of 100 nm is assumed

The regrowth designs show an improvement in cutoff frequency due to a thinner intrinsic base and lower base transit time (τ_b). In spite of a thinner intrinsic base, all base resistance components except for $R_{b,spread}$ show comparable values to HBT 64C. However, $R_{b,spread}$ for regrowth and non-regrowth designs converge as the emitter width scales further.

4.5 Regrowth as a Viable Technology

The regrowth HBT structure can be grown either by regrowing the extrinsic base around the emitter [3], or by regrowing the emitter after etching a gap in the extrinsic base [4]. This section explores the viability of each approach based on

capabilities of existing growth technologies.

Base regrowth of the extrinsic base region has three advantages over emitter regrowth. Firstly, the regrowth interface is not in the active emitter-base depletion region unlike emitter regrowth. Secondly, the emitter metal can be formed prior to base regrowth, thus allowing for blanket base regrowth without the need for any additional lithography steps. Thirdly, the base regrowth width does not scale as the emitter width is scaled for higher RF performance. The extrinsic regrowth p-InGaAs must have high doping $>1*10^{20}cm^{-3}$ and have good crystalline growth for low R_{bb}.

Using MBE to regrow highly doped p-InGaAs extrinsic base around dummy refractory metal emitters have yielded poor morphology growth [5] which leads to higher R_{bb}, and is a source of interference when using e-beam lithography for subsequent steps [6].

MOCVD base regrowth is not a viable option as the UCSB Thomas Swan 2 MOCVD reactor uses Zn as a p-dopant and is unable to grow p-InGaAs with a doping higher than $2*10^{19}cm^{-3}$.

Emitter regrowth of the emitter-base junction allows more freedom in choosing the emitter metal, as the emitter metal is deposited after regrowth and is not exposed to regrowth conditions. Fine control of the regrown semiconductor doping profile is required for growth of the various emitter layers, and the growth morphology must be smooth.

MBE regrowth of the InP emitter and InAs emitter cap has been demonstrated previously [7]. Though the technology yields RF HBTs at 700nm emitter width, it is unable to scale to to the 100nm node. The MBE regrowth is non-selective

and grows on the sidewalls of the regrowth window, thus limiting the minimum regrowth window width. The regrowth is poly-crystalline which adds to R_{ex} and this is exacerbated as emitter width shrinks. Lastly, the process for MBE emitter regrowth requires that the emitter metal be aligned to the regrowth which adds significant complexity to the device process flow.

This work proposes selective MOCVD regrowth of the emitter semiconductor using a self-aligned process flow. It has previously been demonstrated at UCSB that silicon doped n-type InP/InGaAs regrown via MOCVD has excellent morphology, low contact resistance, and is selective with no growth on oxide masks [8] [9]. A viable HBT technology that utilizes MOCVD emitter regrowth must be able to scale $\leq 100nm$, maintain low R_{ex}, R_{bb}, R_{cc}, and use a self-aligned emitter metal process.

A major challenge with MOCVD regrowth is that it introduces hydrogen at high temperatures. The H^{+} bonds with carbon p dopant in the p-InGaAs and passivates it. Reactivating the carbon doping in the base post-regrowth is critical for the process to be successful. It has been shown that the hydrogen can be removed and the carbon reactivated by annealing samples at 500°C for >10min under N_2 ambient [10]. However, it was discovered that this damages the p-InGaAs surface. Section 5 discusses the source of this damage, its implications, and the steps taken to minimize the damage to yield working transistors.

4.6 Self-Aligned Emitter Regrowth HBT Process

This section proposes a process flow for RF HBTs using MOCVD emitter regrowth, that can be scaled to w_{E} $\leq$100 nm. Process modules from the ALD emitter process (Section 3.5) have been integrated with MOCVD emitter regrowth such that the emitter metal is self-aligned to the emitter regrowth. Furthermore, the emitter metal technology can be scaled to emitter widths $\leq$100nm. Figure 4.4 shows the proposed process flow.

The extrinsic base is protected using a blanket ALD SiO_2 layer and then blanket Si is sputtered on top. Trenches for the emitter regrowth are patterned and etched using e-beam lithography and Si Deep RIE etch respectively. This is identical to the process described in 3.5. The SiO_2 layer is wet etched. [8] showed that 2-3nm of InGaAs can be etched in a controlled manner by oxidizing the surface using ozone, and then removing the oxide by using dilute HCl. This self limiting "digital" etch is used to etch the extrinsic base and expose the top of the intrinsic base. The exposed surface is treated with dil HCl, and n-InP/n-InGaAs emitter semiconductor is regrown via MOCVD. Blanket Ru is deposited on the samples using ALD, and then blanket etched away such that Ru is remaining in the emitter trench only. The Si and SiO_2 are etched away to expose the extrinsic base. Dielectric sidewalls are deposited and etched to insulate the emitter metal and provide structural support. The top 3-5nm of the extrinsic base is digitally etched to remove semiconductor that was damaged during sidewall etch. Blanket base contact metal is deposited and base metal pads are subsequently lifted off.

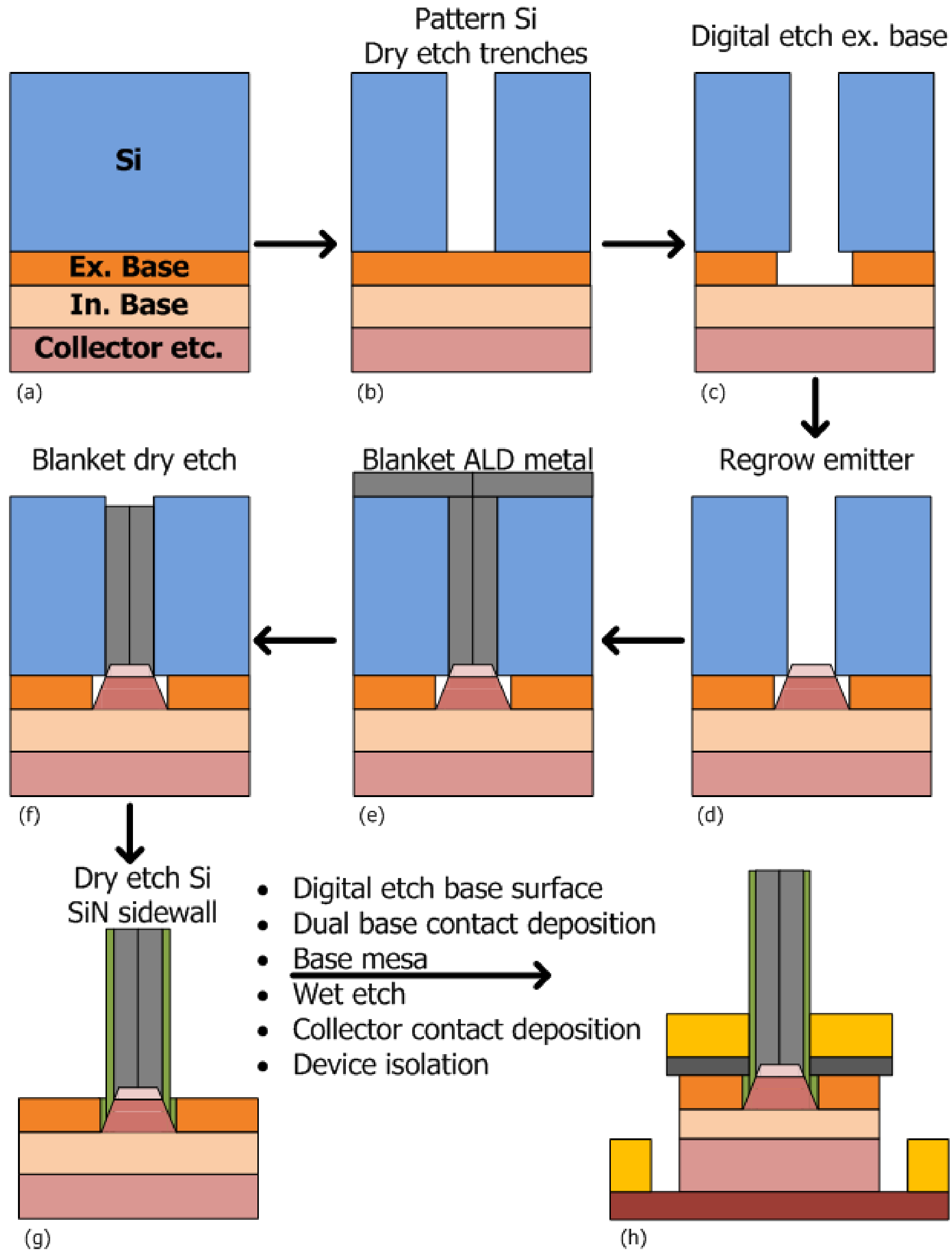

Figure 4.4: Process flow for fabricating emitter regrowth HBTs with a self--aligned emitter metal deposited via ALD. HBT fabrication steps after (g) are identical to W/TiW emitter HBT process flow shown in Appendix B.

The active device region is protected and the base-collector wet-etched down to the sub-collector InGaAs cap. Collector contacts are lifted off and the device is isolated. A PECVD SiN layer is deposited for structural support and the device is planarized via BCB. A low temperature SiN layer is deposited as an anchor (Section 3.1) and the first metal layer is lifted off.

Since the emitter metal is deposited in the trench that was etched as a regrowth window, it is not required to align the emitter metal to the regrowth. This is important as an aligned process increases the process complexity, especially as the emitter width is scaled. Note that the step to anneal the sample and reactivate carbon doping is not mentioned here, as it is discussed in detail in chapter 5.

References

[1] Pekarik, J.J.; Adkisson, J.; Gray, P.; Liu, Q.; Camillo-Castillo, R.; Khater, M.; Jain, V.; Zetterlund, B.; DiVergilio, A.; Tian, X.; Vallett, A.; Ellis-Monaghan, J.; Gross, B.J.; Cheng, P.; Kaushal, V.; He, Z.; Lukaitis, J.; Newton, K.; Kerbaugh, M.; Cahoon, N.; Vera, L.; Zhao, Y.; Long, J.R.; Valdes-Garcia, A.; Reynolds, S.; Lee, W.; Sadhu, B.; Harame, D., "A 90nm SiGe BiCMOS technology for mm-wave and high-performance analog applications," in Bipolar/BiCMOS Circuits and Technology Meeting (BCTM), 2014 IEEE , vol., no., pp.92-95, Sept. 28 2014-Oct. 1 2014

[2] J. Rode, IC Fabrication Technology for Highly Scaled THz DHBTs.. Ph.D. Thesis, University of California, Santa Barbara, Santa. Barbara, Ca, U.S.A., 2015.

[3] Shimawaki, H.; Amamiya, Y.; Furuhata, Naoki; Honjo, K., "High-fmax AlGaAs/InGaAs and AlGaAs/GaAs HBT's with p+/p regrown base contacts," in Electron Devices, IEEE Transactions on , vol.42, no.10, pp.1735-1744, Oct 1995

[4] Fu, S.L.; Park, S.; Hsin, Y.M.; Ho, M.C.; Chin, T.P.; Yu, P.L.; Tu, C.W.; Asbeck, P.M., "GaInP/GaAs HBTs with selectively regrown emitter and wide bandgap extrinsic base," in Device Research Conference, 1994. 52nd Annual , vol., no., pp.91-92, 1994

[5] A. Baraskar, (Development of Ultra-Low Resistance Ohmic Contacts for InGaAs/InP HBTs.. PhD thesis. University of California, Santa Barbara, Santa. Barbara, Ca, U.S.A., 2011.

[6] Nonalloyed and alloyed lowresistance ohmic contacts with good morphology for GaAs using a graded InGaAs cap layer. Mehdi, I. and Reddy, U. K. and Oh, J. and East, J. R. and Haddad, G. I., Journal of Applied Physics, 65, 867-869 (1989)

[7] D. Scott, (Indium Phosphide Heterojunction Bipolar Transistors with Emitter Regrowth by Molecular Beam Epitaxy.. PhD thesis.

[8] S. Lee, C. Y. Huang, A. D. Carter, D. C. Elias, J. J. M. Law, V. Chobpattana, S. Krmer, B. J. Thibeault, W. Mitchell, S. Stemmer, A. C. Gossard, and. M. J. W. Rodwell, Record Extrinsic Transconductance (2.45 mS/m at VDS. = 0.5 V) InAs/In0.53GaAs Channel MOSFETs Using MOCVD Source-Drain. Regrowth, Symposium on VLSI Technology, T246, 2013.

[9] C-Y. Huang, (III-V Ultra-Thin-Body InGaAs/InAs MOSFETs for Low Standby Power Logic Applications.. PhD thesis.

[10] Noriyuki Watanabe, Shoji Yamahata, Takashi Kobayashi, Hydrogen removal by annealing from C-doped InGaAs grown on InP by metalorganic chemical vapor deposition, Journal of Crystal Growth, Volume 200, Issues 34, April 1999, Pages 599-602, ISSN 0022-0248

Chapter 5

Experimental Results and Analysis

This chapter lists the challenges faced in reactivating carbon doping in the p-InGaAs base, the fabrication processes explored to minimize base surface damage and base contact resistivity, and the I-V characteristics of HBTs fabricated using MOCVD selective emitter regrowth. The HBTs fabricated were Large Area Devices (LAD) as this allows for rapid prototyping and troubleshooting. The process flow for LADs is also listed.

5.1 Carbon Passivation of p-InGaAs Base

[1] has shown that hydrogen can be removed and carbon doping reactivated in p-InGaAs by annealing in N_2 ambient at 500^oC for 10 min. The hole concentration in the p-InGaAs layers was measured using Hall measurement [2]. The experiment

was repeated at UCSB, using an AET RX6 Rapid Thermal Processor to anneal in a N_2 ambient at 500^oC for 10 min. Figure 5.1 summarizes the results of the annealing study. A 10 nm ALD SiO_2 cap was used to prevent As out-diffusion and chamber contamination.

Process	Film Thickness(nm)	Anneal Chamber/Gas	Hall p-Conc.($10^{19}cm^{-3}$)		
			Before Process	After Regrowth	After Anneal
Regrow n-InP	20	RTA/N_2	10	0.7	5.5
Wet etch InP	200	RTA/N_2	10	0.7	9
No process	20	RTA/N_2	10	-	5.5
	20	MBE/As	10	-	9.5

Table 5.1: Hall hole carrier concentration of p-InGaAs films after various processing and anneal conditions.

It was observed that the hole carrier concentration measured after annealing was a function of the film thickness. ≈55% of the hole concentration was reactivated on a 20nm InGaAs film, vs 90% for a 200nm thick film. This suggests that the p-InGaAs surface is damaged. A high carrier concentration is observed for samples that were annealed in an MBE chamber under As over-pressure. Thus, the surface damage in samples is due to As out-diffusion through the SiO_2 cap. It is unclear if this is during regrowth or anneal. Section 5.4 discusses this in further detail to show that the bulk of surface damage is during the annealing step with an oxide anneal cap.

5.2 Large Area Device HBT Emitter Regrowth Process

Modern HBTs employ base thicknesses of 15-30 nm with a base doping of 9-10*$10^{19} cm^{-3}$ at the emitter-base junction. The regrowth process and anneal shown in 5.1 would lead to a doping of 4.95-5.5*$10^{19} cm^{-3}$ at the base surface after regrowth and anneal. While the doping is not ideal, it is sufficiently high for forming ohmic base contacts [3].

LADs were fabricated using the aforementioned annealing process with an oxide cap, in order to extract the regrown emitter access resistance, and emitter-base diode characteristics. A LAD structure was used as it reduces process complexity and thus allows for rapid prototyping and troubleshooting. Figure 5.1 shows the process flow used for LADs.

Note that this process is different from the self-aligned emitter process in section 4.6. The primary difference being that the regrowth window mask is purely SiO_2 rather than SiO_2/Si, and that the lifted-off emitter metal is aligned to the regrowth window. The emitter width for LADs ranges from 500-4000 nm.

In this process, an ALD SiO_2 cap is deposited as an annealing cap after the regrowth mask is wet-etched away. The sample is annealed to reactivate the carbon doping, and base contacts are lifted off after removing the annealing cap. The remainder of the process is identical to the the self-aligned emitter process.

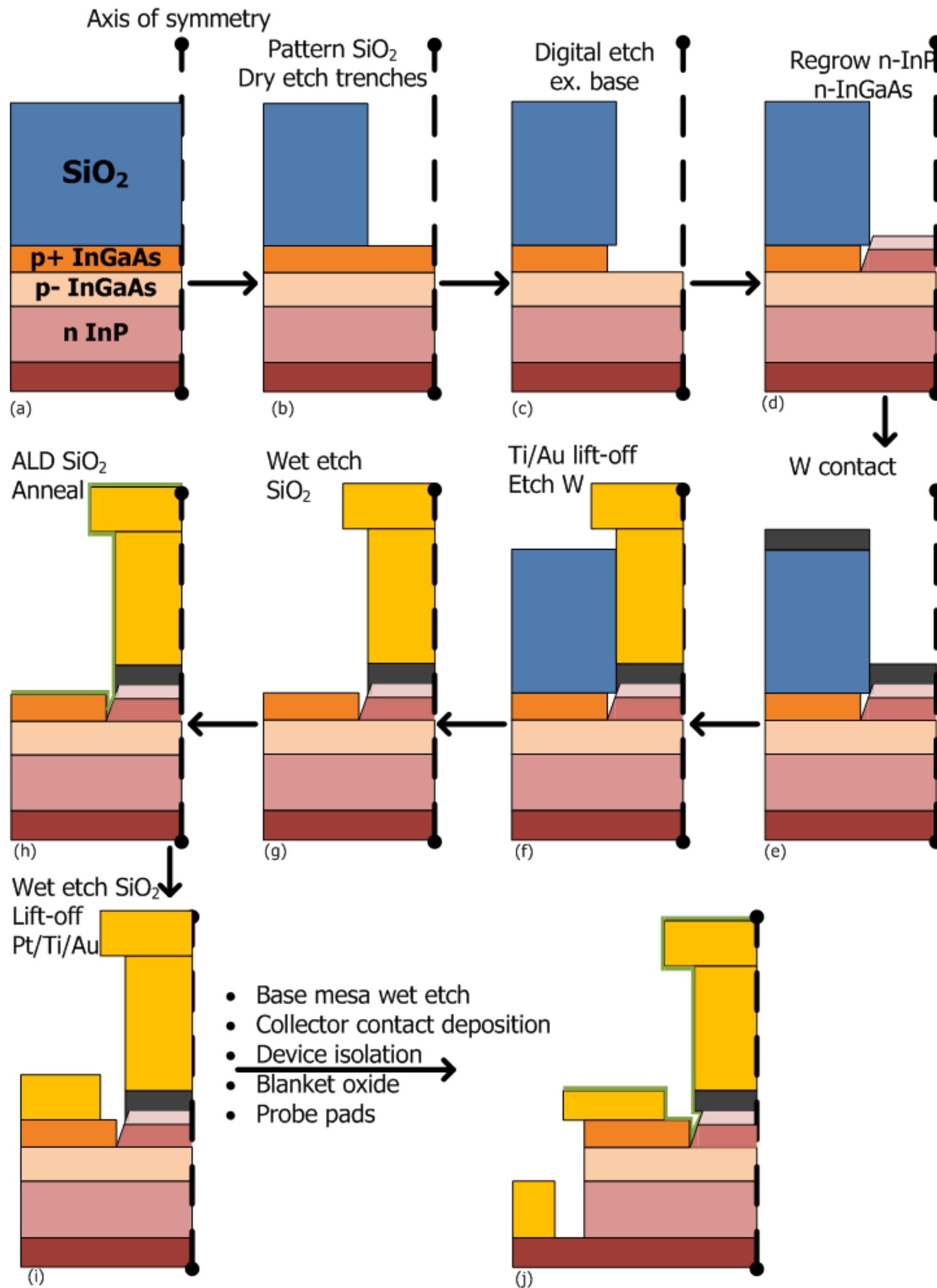

Figure 5.1: Process flow for a Large Area Device (LAD) HBT with emitter regrowth. Steps after (i) are identical to RF HBT process in Appendix B.

5.3 HBT 68Q4 - Oxide Protective Cap

5.3.1 Device Structure and Process Feature

HBT68 utilizes a 15nm extrinsic InGaAs base that is doped 9-6.6*$10^{19}cm^{-3}$, and a 10nm intrinsic base doped from 6.6-5*$10^{19}cm^{-3}$ from emitter to collector. The design employs a 100nm collector structure (setback, superlattice, InP collector) with doping concentration of 5*$10^{16}cm^{-3}$. The detailed epitaxial structure is listed in table 5.2. The emitter structure listed is regrown using MOCVD. Note that the extrinsic base is highlighted in yellow and is not below the emitter-base junction, but to the side. It should be noted that HBT 68 was designed for RF

Layer	Semiconductor	Thickness (Å)	Doping (cm^{-3})
Emitter cap	$In_{0.53}Ga_{0.47}As$	100	8×10^{19}:Si
Emitter	InP	50	5×10^{19}:Si
Emitter	InP	150	3×10^{18}:Si
Extrinsic Base	$In_{0.53}Ga_{0.47}As$	150	$9 - 6.6 \times 10^{19}$:C
Intrinsic Base	$In_{0.53}Ga_{0.47}As$	100	$6.6 - 5 \times 10^{19}$:C
Setback	$In_{0.53}Ga_{0.47}As$	135	5×10^{16}:Si
B-C grade	-	165	5×10^{16}:Si
δ-doping	InP	30	3.6×10^{18}:Si
Collector	InP	670	5×10^{16}:Si
Sub-collector	InP	75	2×10^{19}:Si
Sub-collector	$In_{0.53}Ga_{0.47}As$	75	4×10^{19}:Si
Sub-collector	InP	3000	1×10^{19}:Si
Etch stop	$In_{0.53}Ga_{0.47}As$	35	undoped
Substrate	InP	-	undoped

Table 5.2: Epitaxial structure of HBT 68. The emitter-base junction is formed at the Emitter-Intrinsic base interface, and the extrinsic base lies on either side of this junction, on top of the intrinsic base.

HBTs at the 100nm emitter width node, and thus there is no clear doping step between the intrinsic and extrinsic base.

5.3.2 TEM Analysis

Figure 5.2 shows a cross sectional TEM of a 500 nm wide emitter. The emitter metal (W/Ti/Au) is misaligned with respect to the regrowth window by 100 nm. Thus, the base metal to the right is closer to the emitter-base junction. A close-up of the edge of the emitter-base junction shows that the emitter semiconductor does not grow on the extrinsic base and has a 54° angle, characteristic of the (111)B facet.

The overhang in the emitter metal is designed to allow for self aligned base metal deposition without needing an emitter sidewall. It is seen that the base and emitter metal do not connect as intended.

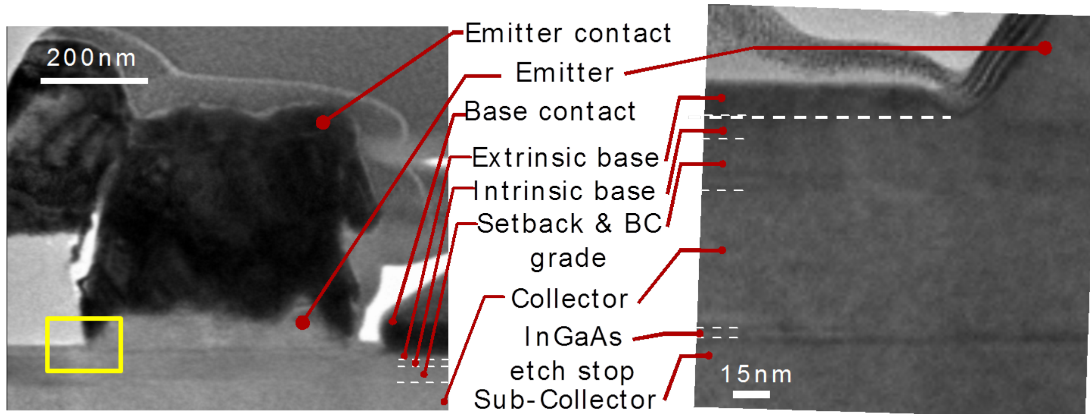

Figure 5.2: Cross-sectional TEM image of HBT 68Q4 and a close-up of the emitter-base interface. It can be seen that the emitter semiconductor does not contact the extrinsic base.

Figure 5.3 shows a closeup of the left base contact. The surface of the base is rough and has been damaged during fabrication. Since the surface below the base contact is also rough, the damage can be attributed to regrowth, anneal cap deposition, or the anneal itself.

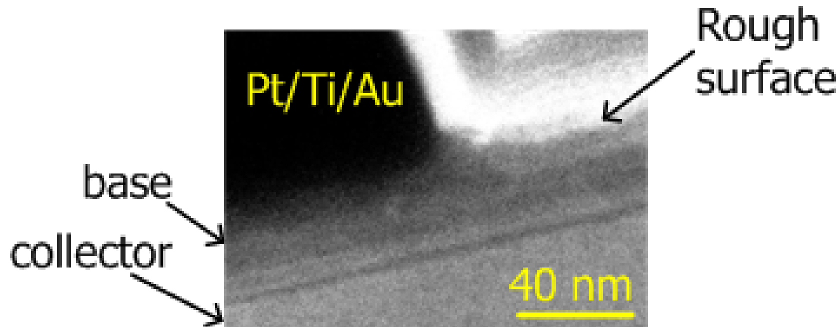

Figure 5.3: Cross-sectional TEM of the base surface and base contact of HBT 68Q4. The base surface is damaged.

5.3.3 DC Characteristics

TLM measurement structures were included in the mask design for measuring emitter, base, and collector contact resistivity. The emitter TLM test structures could not be measured as the semiconductor in the TLM gap spacing was etched during isolation due to poor photoresist adhesion. Base TLM structures indicate contact resistivity of $3500\ \Omega.\mu m^2$. Failure to remove the oxide annealing cap prior to metal deposition is ruled out by the TEM images. The extracted base sheet resistance was measured to be 2470 $\Omega/\square$, up from a sheet resistance of 1248 $\Omega/\square$ measured before regrowth via four-point measurement. Thus, only 50% of the carbon dopants were reactivated during the anneal. A base doping of $4*10^{19}cm^{-3}$ yields contact resistivity $<$100 $\Omega.\mu m^2$ [4], thus the base contacts resistivity should be much lower than measured. Collector contact resistivity was measured to be 34 $\Omega.\mu m^2$.

Figure 5.4-5.5 show the emitter-base diode, base collector diode, and forward-active gummel characteristics of a transistor of emitter area 0.4x8μm^2. The base-collector area is 4.2x11 μm^2.

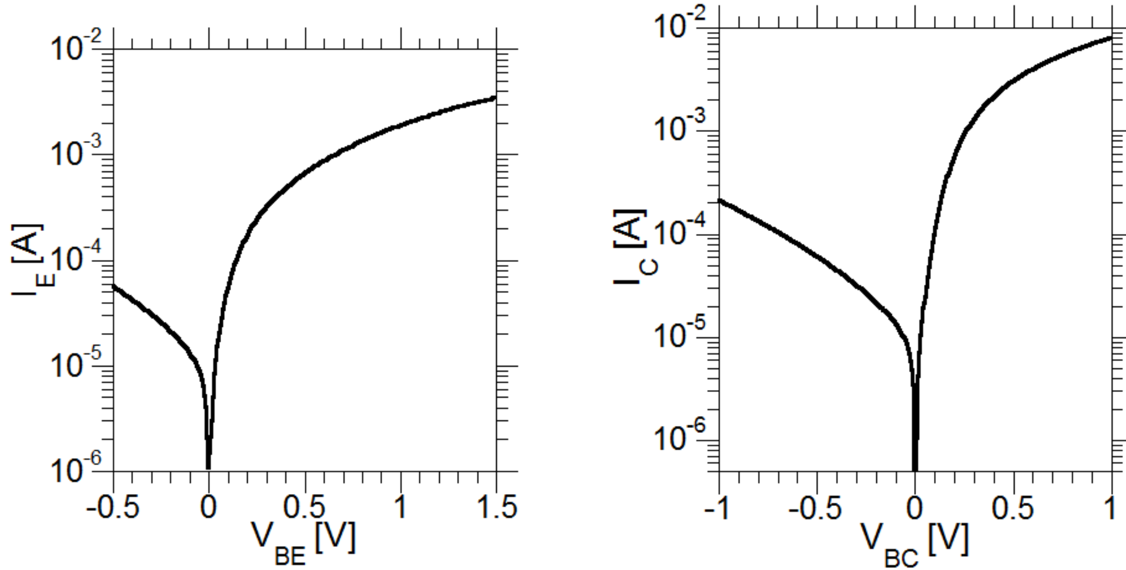

Figure 5.4: HBT 68Q4 Emitter-Base and Base-Collector diode I-V characteristics.

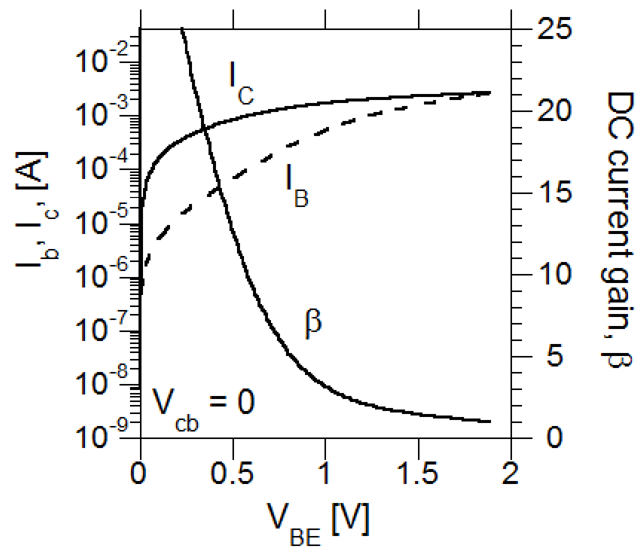

Figure 5.5: HBT 68Q4 gummel curve at zero base-collector bias. Collector leakage current I_{C} at low V_{BE} is due to extremely high R_{bb}

The gummel curve shows an anomalously high β at low V_{BE} that rapidly reduces to 1 as the voltage increases. Moreover, the collector current I_{C} is very large ($\approx$100μA) at V_{BE} <0.2V. This indicates a large lateral base resistance in the device, which leads to a large voltage drop between the base contact and base-emitter junction such that the base-collector junction is forward biased [5]. As V_{BE} increases, the base-collector junction turns on and the base current approaches the collector current to yield β of 1. Consequently, common-emitter curves do not show saturation.

To summarize, the measured base contact resistivity does not correspond to the measured base sheet resistance. The high base sheet resistance prevents the base-emitter diode from turning on in forward-active mode and thus gummel and common-emitter characteristics cannot be measured.

5.4 Ohmic Contacts To p-InGaAs After Regrowth

It is imperative that the base contact resistivity and sheet resistance be reduced in order to measure working HBT characteristics. Section 5.1 shows that the p-InGaAs surface is damaged prior to base metal deposition. This section details experiments that were conducted to minimize this damage and reduce base contact resistivity.

Section 5.3 utilized an oxide cap for protecting the base surface during regrowth as well as during the anneal. Figure 5.6 shows process flow for two samples. The process for sample A explores W as an annealing cap, whereas sample B tests W as a regrowth as well as an annealing cap. In both experiments, W is used as the

contact metal and as a diffusion barrier against Ti/Au that is lifted off above it. A blanket ALD oxide layer is used as an annealing cap to prevent Au migration and As degassing from the InGaAs in the gap spacing. Both samples consist of a 20nm p-InGaAs layer with a carrier concentration of $1*10^{20} cm^{-3}$, grown on a semi-insulating InP substrate.

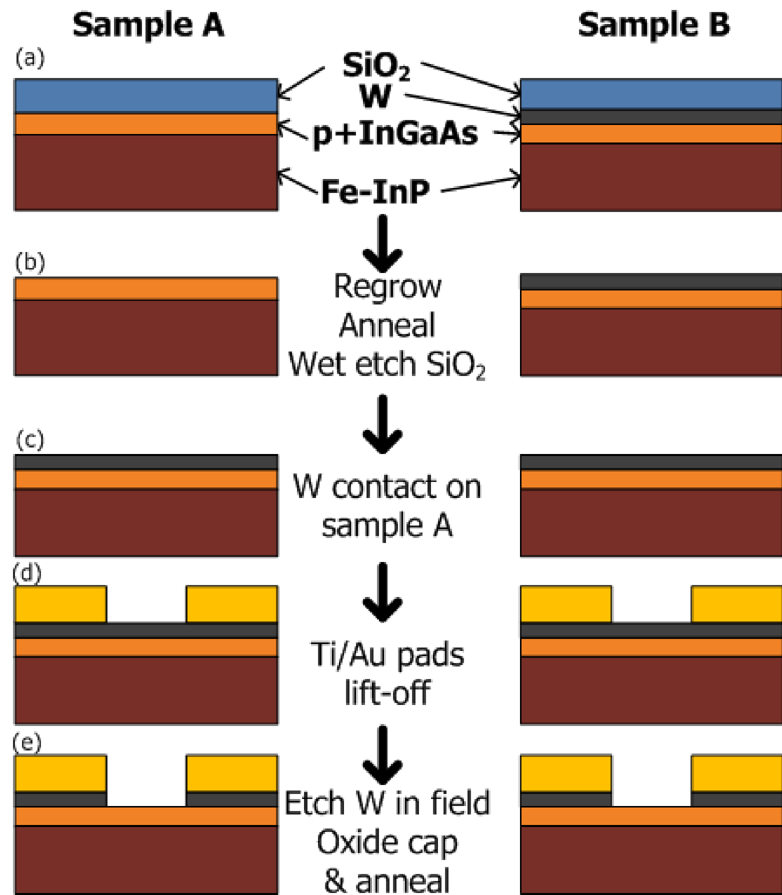

Figure 5.6: TLM split to determine source of base surface damage.

Table 5.3 lists the measured contact resistivity R_{cont} of samples A and B, and HBT68Q4. Contact resistivity of W as a contact metal to p-InGaAs doped at $1*10^{20} cm^{-3}$ is also listed for comparison [4].

Sample	Regrowth Mask	Anneal cap	Contact Metal	$R_{cont.}$ ($\Omega.\mu m^2$)
No regrowth	-	-	W/Ti/Au	2.9
HBT 68Q4	SiO_2	SiO_2	Pt/Ti/Au	rectifying
Sample A	SiO_2	W	W/Ti/Au	18.4
Sample B	W/SiO_2	W	W/Ti/Au	5.5

Table 5.3: Measured contact resistivity to p-InGaAs on TLM test structures for various process samples. Hall carrier concentration of $1*10^2 cm^{-3}$ was measured on all samples before processing. Samples A and B indicate that SiO_2 is an insufficient cap and damages the surface.

Using W as an annealing cap reduces R_{cont} significantly from 3400 to 18 $\Omega.\mu^2$. Though much lower, the contact resistivity is still too high to be of use in an RF device based on the HBT scaling roadmap (Section 2.2).

However, using W as a cap during regrowth as well as during anneal yields R_{cont} of 5.5 $\Omega.\mu m^2$, which is close to the reported value of R_{cont} without any high temperature processing. Based on literature values, this indicates a carbon doping under the W contact of $9*10^{19} cm^{-3}$.

Thus, using a W capping layer as a regrowth and annealing cap yields carbon activation of 90%, and contact resistivity of 5.5 $\Omega.\mu m^2$. More importantly, this is sufficient for RF HBTs at the 100 nm emitter width.

5.5 Buried W as Regrowth Mask

Tungsten was chosen as a regrowth mask for three reasons. It is known that W contact resistivity to highly doped p-InGaAs is 3 $\Omega.\mu m^2$. W has a high boiling point and thus can be heated to 600°C without contaminating the MOCVD chamber. Finally, it can be selectively wet etched using AZ300MiF to expose the regrowth windows without damaging the InGaAs base surface. This section

demonstrates a process flow where W base contacts are deposited on the extrinsic base, and the emitter regrowth windows are etched in afterwards.

Figure 5.7 shows cross-sectional SEM images of where regrowth windows have been etched into a blanket W/SiO_2 stack. The W undercut after being etched in AZ300MiF suggests that W was successfully wet etched in the regrowth windows. The fabrication process after regrowth remains the same as before, except that the blanket W base contact is already there.

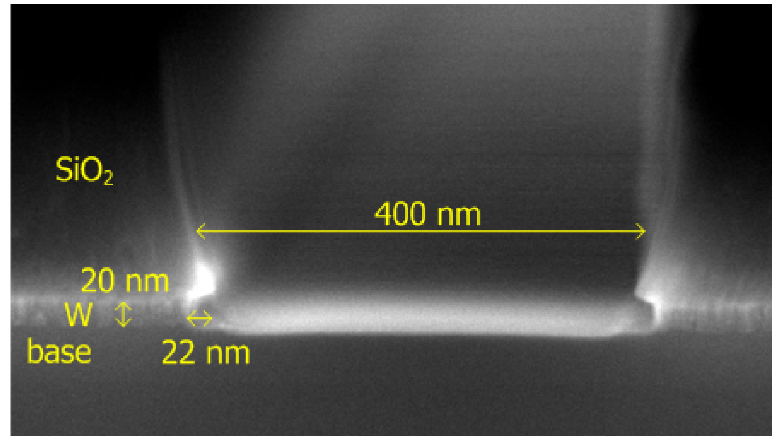

Figure 5.7: Cross-sectional SEM of a regrowth window after the buried W has been wet-etched using AZ300MiF. The undercut is visible at the trench corner. The extrinsic base is then digitally etched and the emitter is regrown.

Emitter semiconductor was regrown on HBT epi using the above process. Figure 5.8 shows a cross-sectional SEM of a sample post regrowth. There is nucleation in select areas in the growth window, but most of the regrowth window shows no growth. This suggests presence of a residual layer on the p-InGaAs that is inhibiting growth. Furthermore, the p-InGaAs at the lateral W boundary has been etched away.

An additional CF_4/O_2 descum was performed prior to regrowth, as a means of

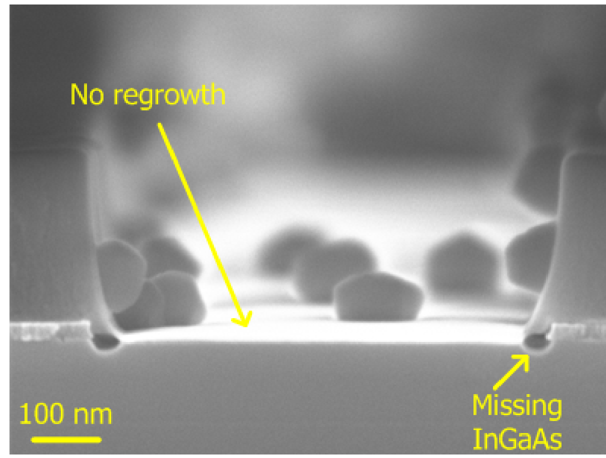

Figure 5.8: Cross-sectional SEM image of regrowth trench post regrowth. There is growth nucleation in select areas of the window only. This suggests presence of a residual layer at the surface that is inhibiting growth.

etching the unknown residual layer away. Figure 5.9 shows that this has removed the residue, but the resulting regrowth morphology is rough. Furthermore, the p-InGaAs under the W layer has voids in it.

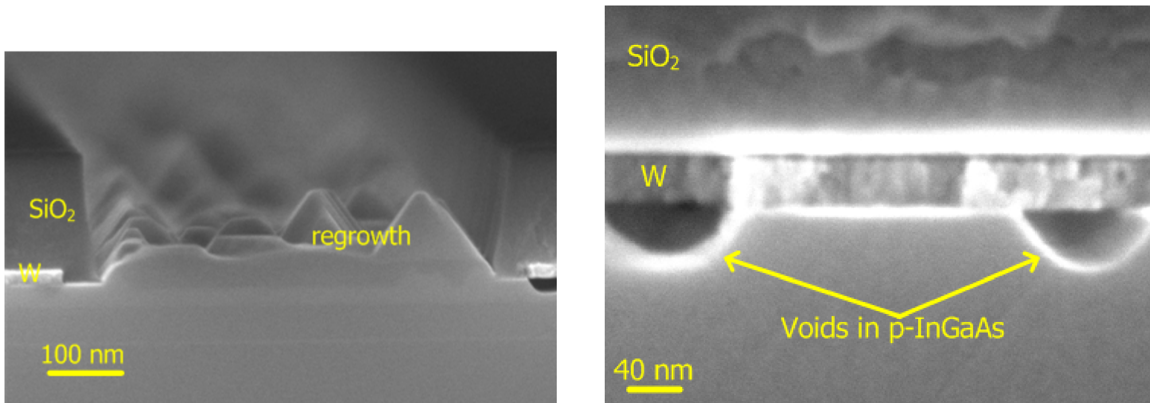

Figure 5.9: Cross-sectional SEM image of buried W regrowth after additional CF_4/O_2 descum. The regrowth morphology is rough and there is voiding in the InGaAs base.

The W film was deposited via e-beam evaporation, which is known to have high stress [6] and thus a columnar structure. It is suspected that local cracks

in the W film provide a path for the InGaAs components to degas out, leaving behind voids. W as a buried regrowth mask is desirable for a regrowth HBT, but inability to regrow high quality emitter semiconductor and voiding of the InGaAs base make it an unfeasible option.

5.6 HBT 70R4 - InP Protective Cap

Section 5.4 proves that protecting the p-InGaAs base surface during regrowth and anneal is crucial for producing working emitter regrown HBTs. W as a cap is not feasible due to poor regrowth morphology and InGaAs voids, and an alternative solution is required. An alternative is to protect the InGaAs base by using an InP cap. The process and results are discussed in this section.

5.6.1 Device Structure and Process Feature

HBT 70 utilizes a 6 nm extrinsic InGaAs base that is doped 12-10.6*$10^{19} cm^{-3}$, and a 24 nm intrinsic base doped from 10.6-5*$10^{19} cm^{-3}$ from emitter to collector. The design employs a 100 nm collector structure (setback, superlattice, InP collector) with doping concentration of 5*$10^{16} cm^{-3}$. The detailed epitaxial structure is listed in table 5.4. The emitter structure listed is regrown using MOCVD. Note that the extrinsic base is highlighted in yellow and is not below the emitter-base junction, but to the side.

As with HBT 68, HBT 70 was designed for RF HBTs at the 100 nm emitter width node and there is no doping step between the intrinsic and extrinsic base.

The process flow in HBT 70R4 was designed to use an InP cap to protect

Layer	Semiconductor	Thickness (Å)	Doping (cm^{-3})
Emitter cap	$In_{0.53}Ga_{0.47}As$	100	8×10^{19}:Si
Emitter	InP	50	5×10^{19}:Si
Emitter	InP	150	3×10^{18}:Si
Extrinsic Base	$In_{0.53}Ga_{0.47}As$	60	$12 - 10.6 \times 10^{19}$:C
Intrinsic Base	$In_{0.53}Ga_{0.47}As$	240	$10.6 - 5 \times 10^{19}$:C
Setback	$In_{0.53}Ga_{0.47}As$	135	5×10^{16}:Si
B-C grade	-	165	5×10^{16}:Si
δ-doping	InP	30	3.6×10^{18}:Si
Collector	InP	670	5×10^{16}:Si
Sub-collector	InP	75	2×10^{19}:Si
Sub-collector	$In_{0.53}Ga_{0.47}As$	75	4×10^{19}:Si
Sub-collector	InP	3000	1×10^{19}:Si
Etch stop	$In_{0.53}Ga_{0.47}As$	35	undoped
Substrate	InP	-	undoped

Table 5.4: Epitaxial structure of HBT 70. The emitter-base junction is formed at the Emitter-Intrinsic base interface, and the extrinsic base lies on either side of this junction, on top of the intrinsic base.

p-InGaAs during regrowth. Figure 5.10 shows the process flow.

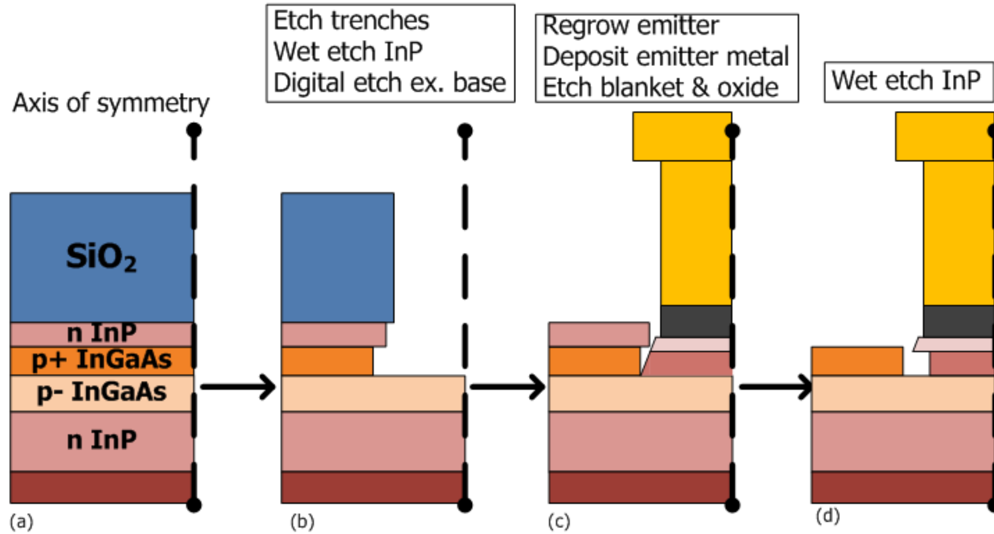

Figure 5.10: Process flow for emitter regrowth HBT LAD that incorporates an InP cap above the base for minimizing surface damage before base contact metal deposition. The process after (d) is identical to Figure 5.1, except that the W/Ti/Au base metal is deposited prior to ALD oxide and anneal.

The original epitaxial design of HBT 70 includes a InGaAs emitter cap and

InP emitter. The emitter cap was wet etched away and a blanket oxide regrowth mask was sputtered. Regrowth windows were etched and the InP was selectively wet etched in the windows to expose the extrinsic base. Emitter semiconductor was regrown after digitally etching the extrinsic base to expose the intrinsic base region. Once the emitter metal is lifted off and the oxide mask removed, an ALD oxide cap is deposited and the sample annealed to diffuse the hydrogen out. The oxide and InP cap is selectively wet etched away. Note that this also undercuts the regrown InP emitter. An undercut of 20-30 nm is expected on each side for a 7s InP wet etch in $H_3PO_4 : HCl$ 4:1. This is acceptable for a LAD with a minimum emitter width of 500 nm.

The subsequent base contact, base mesa, collector contact, isolation, and probe pad lift off steps are identical to the steps listed in section 5.2.

5.6.2 TEM Analysis

Figure 5.11 shows a cross sectional TEM of a 600 nm wide emitter. The emitter metal (W/Ti/Au) is misaligned with respect to the regrowth window by 200 nm. Thus, the base metal to the right is closer to the emitter-base junction.

Figure 5.12 shows a closeup of the red box in Figure 5.11. Small islands of the regrowth are visible instead of the expected uniform layer. The sample was imaged using SEM post regrowth to ensure normal growth, thus the regrown semiconductor has been etched in subsequent processing steps.

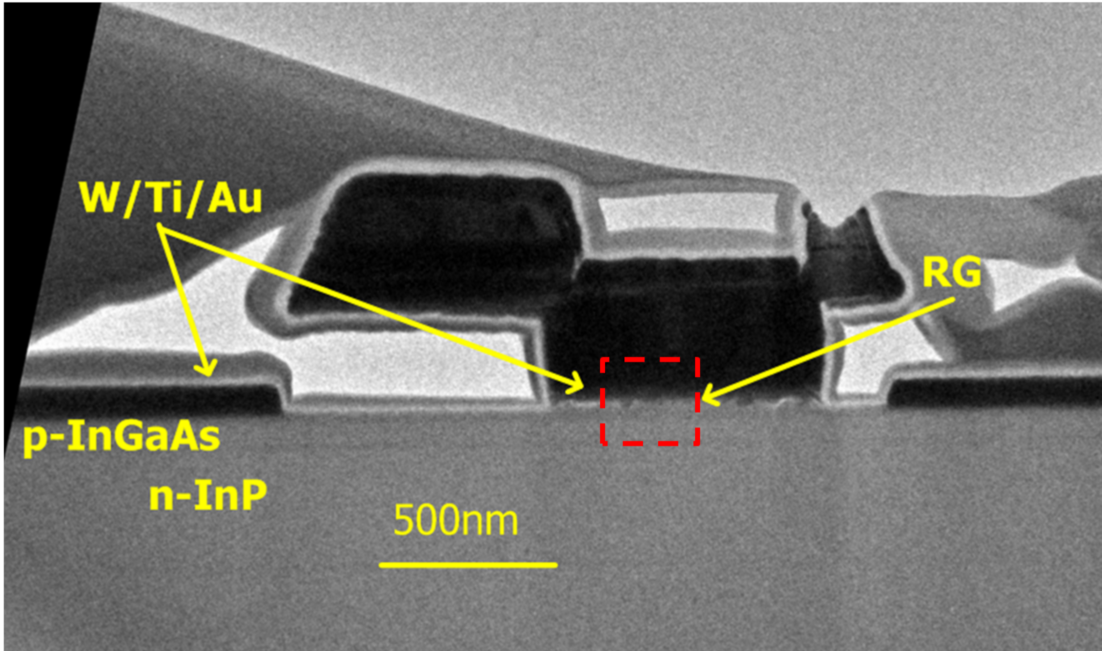

Figure 5.11: Cross-sectional TEM image of HBT70R4.

5.6.3 Issues and Improvements

Wet etch tests on InP regrown in sub-micron trenches shows that its etch rate is orders of magnitude higher than that of bulk MBE grown InP. The wet etch for removing the InP cap also undercut the entire regrown InP. Consequently, the emitter base junction in all devices was either highly resistive due to missing emitter semiconductor, or shorted out due to the emitter metal contacting the base. The base contact resistivity with Pt/Ti/Au metal was measured to be 326 $\Omega.\mu m^2$. A base sheet resistivity of 7000 $\Omega/\square$ was measured, several times higher than the 1400 $\Omega/\square$ measured prior to regrowth. It is suspected that InP forms a barrier for H^+ ions in the valence band and prevents them from diffusing out.

The process flow can be improved by using a 3 nm InP cap that can be digitally etched prior to base metal deposition. This would protect the regrown emitter

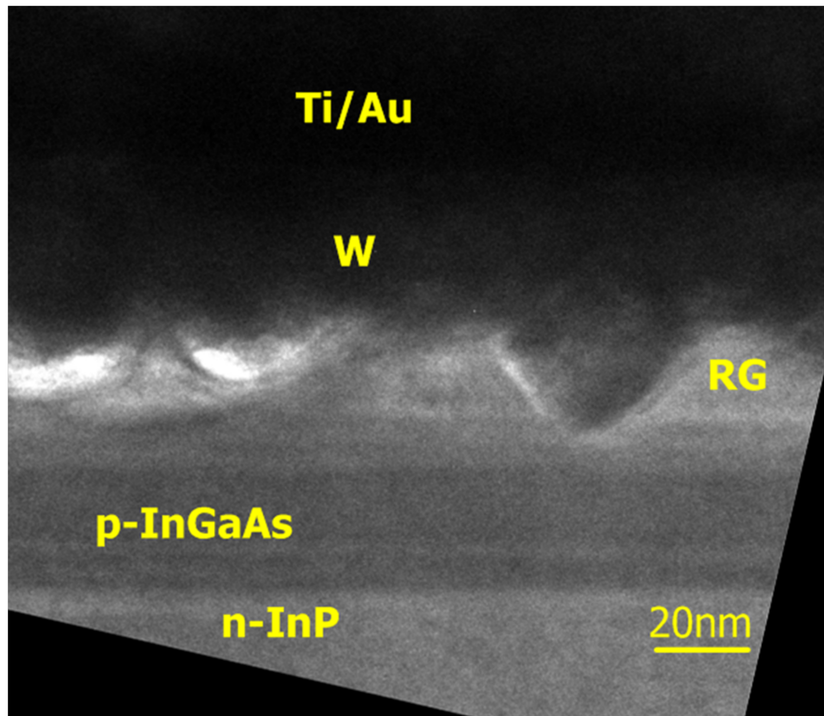

Figure 5.12: Cross-sectional TEM image of the emitter regrowth in HBT70R4. The emitter semiconductor has been etched away during the InP cap wet etch.

semiconductor. A W/Ti/Au base metal can be used and the anneal performed after base metallization. This would remove the InP barrier and allow H^+ ions to diffuse out.

Unfortunately, an epitaxial design with 3 nm InP cap above the extrinsic base was unavailable at the time of this experiment and thus could not be explored. An alternate process for protecting the base surface during anneal is shown in the following section.

5.7 HBT 74 Q4 - W Annealing Cap

Since using a thinner InP regrowth cap and a W annealing cap was not an option due to epi unavailability. An oxide regrowth cap and W annealing cap was explored as a way of reducing base contact resistivity, sheet resistance, and measuring working HBTs with regrown emitter semiconductor. An additional sample (HBT 74Q1) was fabricated simultaneously using the original epi structure i.e. no emitter regrowth or anneal was performed on this sample. This section discusses the process flow and results. DC characteristics of 74Q4 and 74Q1 are presented as a means of comparing a regrown-emitter with a traditional non-regrowth device.

5.7.1 Device Structure and Process Feature

HBT70 utilizes a 4nm extrinsic InGaAs base that is doped 12-11*$10^{19} cm^{-3}$, and a 16nm intrinsic base doped from 11-7*$10^{19} cm^{-3}$ from emitter to collector. The design employs a 70nm collector structure (setback, superlattice, InP collector) with doping concentration of 1*$10^{17} cm^{-3}$. The detailed epitaxial structure is listed in table 5.5. The emitter structure listed is regrown using MOCVD. Note that the extrinsic base is highlighted in yellow and is not below the emitter-base junction, but to the side.

As before, HBT74 was designed for RF HBTs at the 100nm emitter width node and there is no doping step between the intrinsic and extrinsic base.

The process flow in HBT74Q4 was designed to use an oxide cap to protect p-InGaAs during regrowth and a W cap during anneal similar to Sample in Figure

Layer	Semiconductor	Thickness (Å)	Doping (cm^{-3})
Emitter cap	$In_{0.53}Ga_{0.47}As$	100	8×10^{19}:Si
Emitter	InP	150	5×10^{19}:Si
Emitter	InP	150	3×10^{18}:Si
Extrinsic Base	$In_{0.53}Ga_{0.47}As$	40	$12 - 11 \times 10^{19}$:C
Intrinsic Base	$In_{0.53}Ga_{0.47}As$	160	$11 - 7 \times 10^{19}$:C
Setback	$In_{0.53}Ga_{0.47}As$	50	1×10^{17}:Si
B-C grade	-	120	1×10^{17}:Si
δ-doping	InP	30	6×10^{18}:Si
Collector	InP	500	1×10^{17}:Si
Sub-collector	InP	75	2×10^{19}:Si
Sub-collector	$In_{0.53}Ga_{0.47}As$	75	4×10^{19}:Si
Sub-collector	InP	3000	1×10^{19}:Si
Etch stop	$In_{0.53}Ga_{0.47}As$	35	undoped
Substrate	InP	-	undoped

Table 5.5: Epitaxial structure of HBT74. The emitter-base junction is formed at the Emitter-Intrinsic base interface, and the extrinsic base lies on either side of this junction, on top of the intrinsic base.

5.6.

The original epitaxial design of HBT74 includes an InGaAs emitter cap and InP emitter. The emitter was wet etched away and a blanket oxide regrowth mask was sputtered. Regrowth windows were etched, extrinsic base digitally etched and the emitter semiconductor was regrown. A blanket W base contact was deposited after removing the oxide regrowth mask. Ti/Au base metal was lifted off, ALD oxide cap deposited and the sample was annealed to reactivate the p-InGaAs carbon doping.

The subsequent base mesa, collector contact, isolation, and probe pad lift off steps are identical to the steps listed in section 5.2.

5.7.2 TEM Analysis

Figure 5.13 shows a cross sectional TEM of a 450nm wide emitter. The W/Ti/Au base metal is visible.

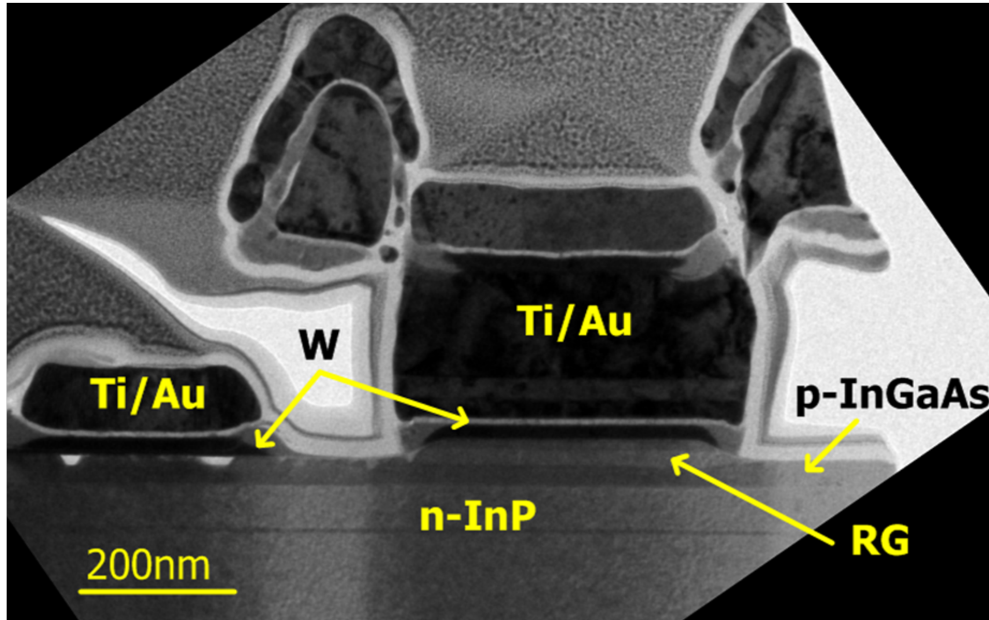

Figure 5.13: Cross-sectional TEM image of HBT74Q4.

Figure 5.14 shows a closeup of the base metal and base mesa. The W base contact was partially etched during Ti/Au as 1165 photoresist etches W. Voids in the p-InGaAs are visible under W/Ti/Au. However, no pitting is visible in areas where only W is present.

It is known that in GaAs, there is diffusion of Ga ions into AuGe contacts at temperatures above 260°C [7]. It is suspected that the W is an inadequate diffusion barrier for Au and Ga during the anneal, similar to section 5.5.

To test the hypothesis, the oxide mask was etched and blanket W evaporated on two HBT samples after emitter regrowth. Ti/Au was blanket evaporated on

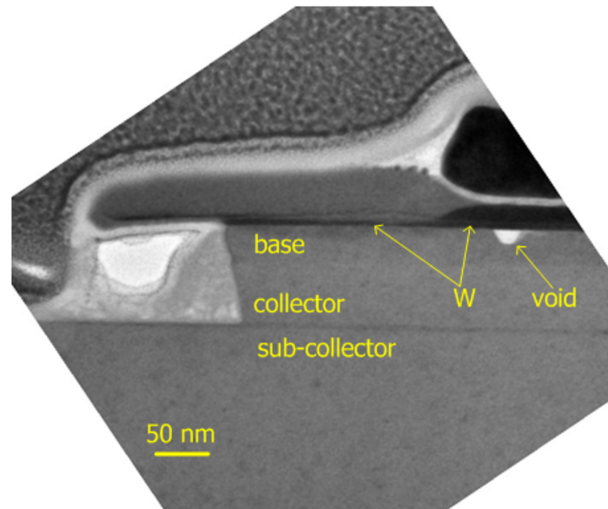

Figure 5.14: Cross-sectional TEM image of the base mesa region of HBT74Q4. There is voiding in the base where W/Ti/Au is present on the surface.

one sample only, and both samples were annealed using an ALD oxide cap. Figure 5.15 shows cross-sectional SEM images of both samples.

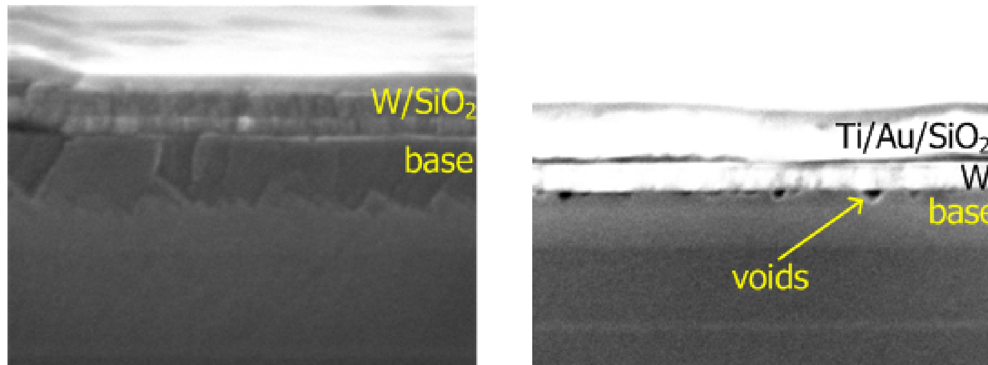

Figure 5.15: Cross-sectional SEM image of the base region after annealing with a W/SiO_2 cap (left) and a W/Ti/Au/SiO_2 cap(right). The p-InGaAs shows voids if Ti/Au is present.

Voids in the InGaAs base are visible in the sample where W/Ti/Au contacts were deposited. These voids are identical to those seen in HBT 74Q4, and extend till the InAlAs/InGaAs superlattice.

Since annealing with a W cap does not lead to void formation, the HBT process can be modified to anneal the sample before lifting off Ti/Au base metal. This approach is discussed further in section 5.8.

5.7.3 Transistor DC Characteristics

This section presents DC characteristics of a 0.8*4 μm^2 emitter device on HBT 74Q4, and compares it with a device of identical dimensions on HBT 74Q1. The base-collector dimension on both devices is 2.4*7 μm^2.

Figure 5.16 shows the emitter-base diode characteristics of both devices. Both diodes show comparable series resistance. Emitter-base parallel resistance R_{par} on 74Q1 has a large variation across multiple devices, suggesting a process induced shunt path from emitter to base metal. This makes it difficult to compare diode ideality factors. The emitter-base diode in 74Q1 also shows resonant tunneling at low bias due to tunneling of carriers between the emitter-base conduction and valence bands respectively.

Figure 5.17 shows the base-collector diode characteristics of both devices. Both diodes show comparable parallel resistance. Base-collector series resistance R_{series} on 74Q1 is large on all devices; sub-collector surface contamination prior to contact metal deposition is suspected.

Figure 5.18 shows gummel curves for both devices with the base-collector shorted and reverse-biased. 74Q4 exhibits maximum β of 28 at $V_{\text{BE}} = 1.67$ whereas maximum β for 74Q1 is 13 at $V_{\text{BE}} = 1.0$. It is possible that the higher β in 74Q4 is due to higher $R_{\text{BE,series}}$ and lower $R_{\text{BC,series}}$ as compared to 74Q1. Thus, it is unclear if a higher β in the regrown-emitter HBT is due to lower $I_{\text{B,Auger}}$ in the

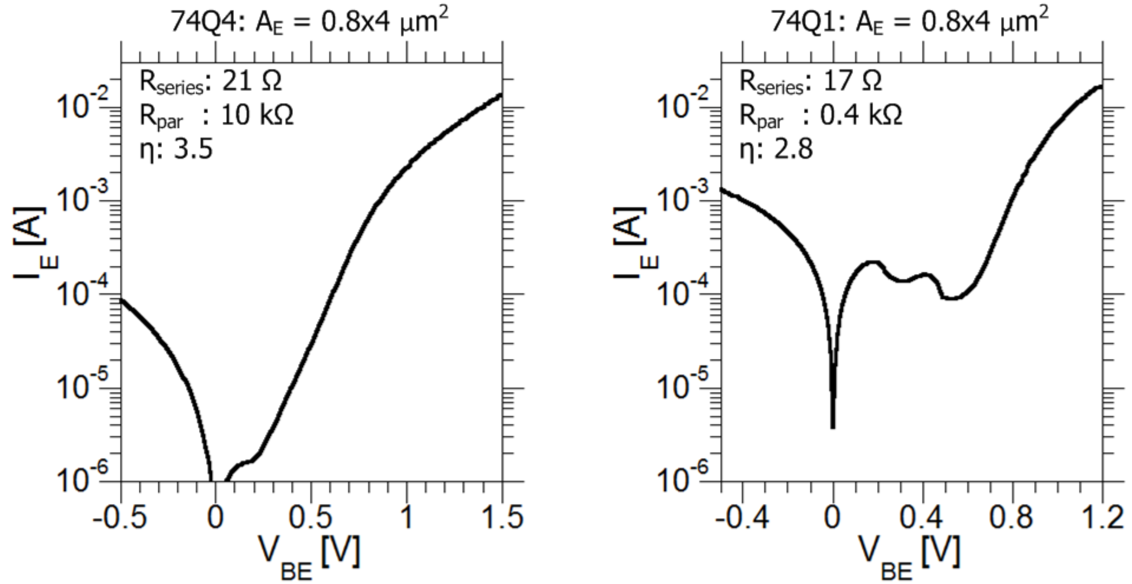

Figure 5.16: HBT 74Q4 and HBT 74Q1 emitter-base diode characteristics. HBT 74Q1 devices show large variation in R_{par}. Shunt between emitter-base metal is suspected.

intrinsic base and lower $I_{\text{B,diff}}$ due to presence of extrinsic-intrinsic base conduction band barrier. Resonant tunneling behaviour at low base-emitter bias can be seen in 74Q1.

Figure 5.19 shows common-emitter curves for both devices. The drop in collector current for 74Q1 is due to a drop in the tunneling current at the base-emitter junction.

Figure 5.20 plots the inverse β of devices measured on 74Q4as a function of their respective perimeter over area. As expected, β shows a decrease as the emitter width is decreased and β_{bulk} of 96 is extracted at infinite emitter width.

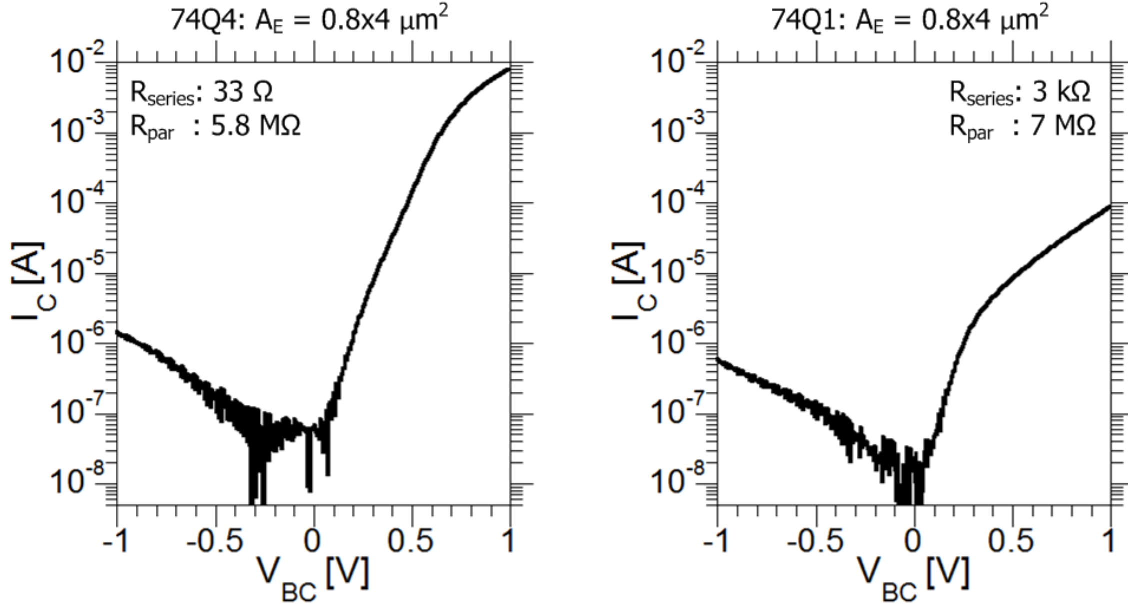

Figure 5.17: HBT 74Q4 and HBT 74Q1 base-collector diode characteristics. HBT74Q1 has high R_{series}. Sub-collector surface contamination prior to contact metal deposition is suspected.

5.8 W Base Contact Yield

While W as an annealing cap and base contact yields working HBTs, the yield for such a process flow is extremely low. W has an etch rate of ≈60 nm/min in photoresist stripper (1165) and is thus attacked during Ti/Au base metal lift-off and subsequent lift-off steps as well. W also etches in photoresist developer (AZ300MiF) at ≈4 nm/min and is exposed to it during every lithography step. These undercut the W metal contact and provides a diffusion path for the above Ti/Au metal layers into the base semiconductor. Thus, a majority of devices fabricated using this process flow yield shorted base-collector diodes.

It is not possible to expose the W contact during Ti/Au base metal lift-off as the W must be exposed. The underside of the W contact is also exposed after

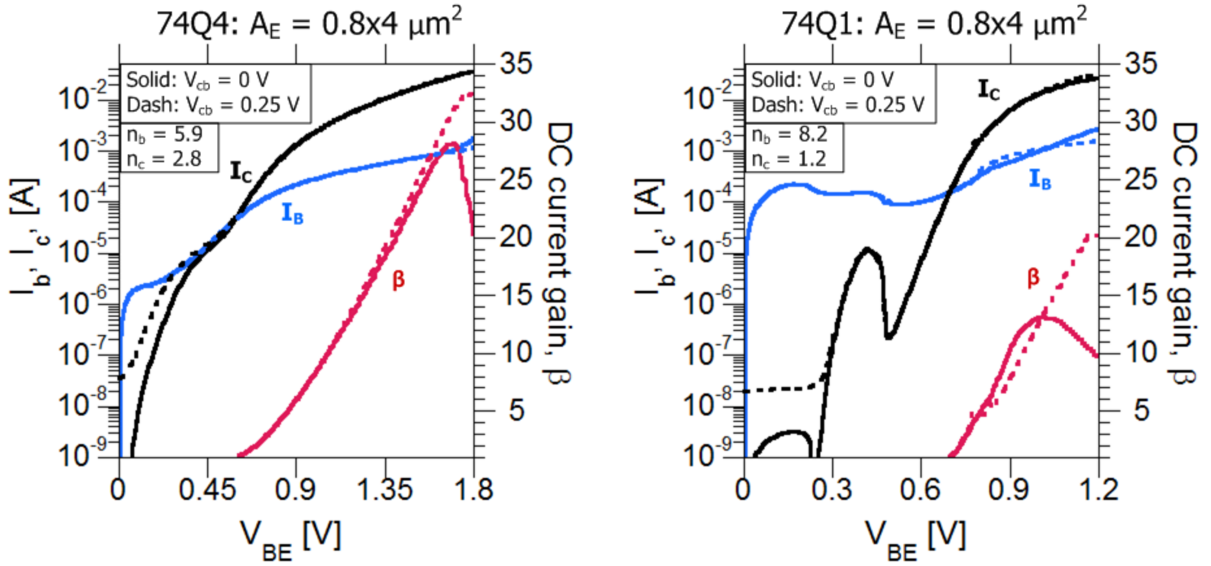

Figure 5.18: HBT74Q4 and HBT74Q1 gummel curves. The regrown-emitter HBT (74Q4) shows higher β of 28 as compared to 13 for 74Q1, at V_{CB}=0. It is unclear if this is due to higher $R_{BE,series}$ and lower $R_{BC,series}$.

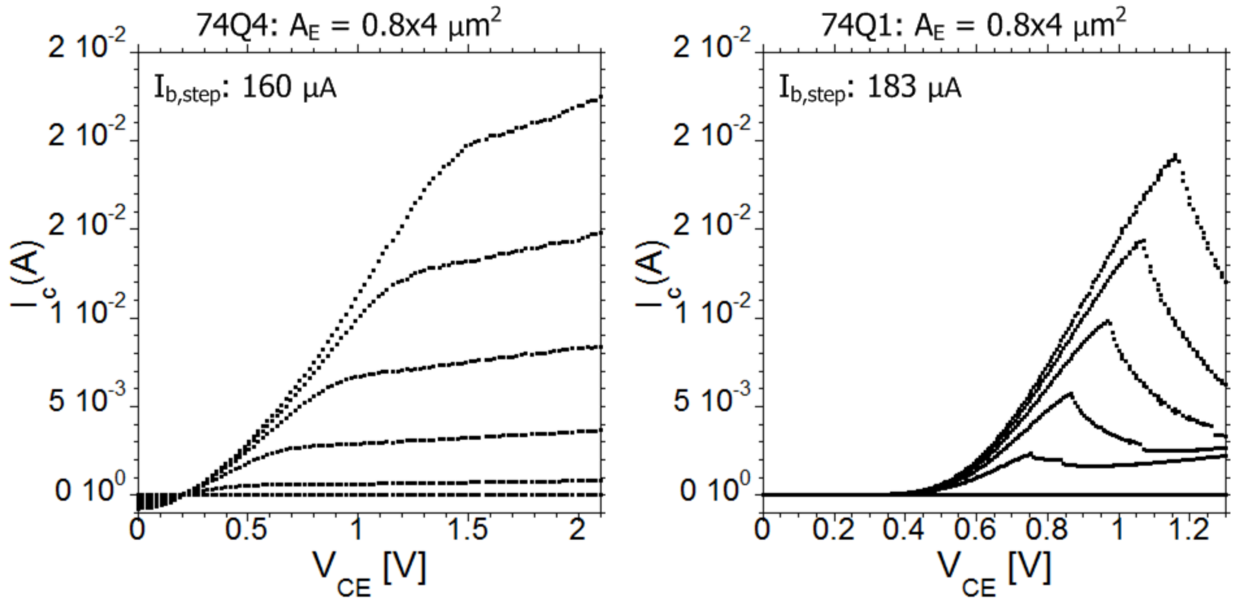

Figure 5.19: HBT 74Q4 and HBT 74Q1 common-emitter characteristics..

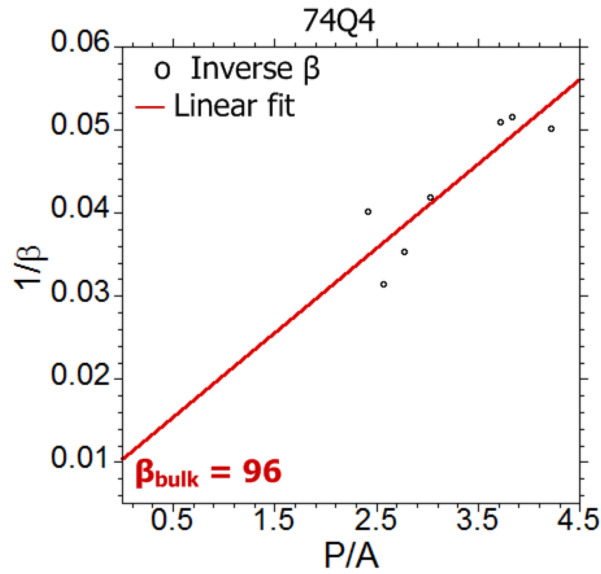

Figure 5.20: Inverse DC current gain ($1/\beta$) vs HBT emitter periphery to area ration ($P_{\mathrm{jE}}/A_{\mathrm{jE}}$ of HBT 74Q4.

the base mesa undercut and cannot be protected till the collector contact metal is lifted-off. Furthermore, base contact widths need to be scaled for RF HBTs which would result in a larger portion of the base contact being undercut.

An alternate process flow or contact metal is required for improving yield. Section 6.2.1 explores this in further detail.

References

[1] Noriyuki Watanabe, Shoji Yamahata, Takashi Kobayashi, Hydrogen removal by annealing from C-doped InGaAs grown on InP by metalorganic chemical vapor deposition, Journal of Crystal Growth, Volume 200, Issues 34, April 1999, Pages 599-602, ISSN 0022-0248

[2] L. J. van der Pauw, ”A Method of Measuring Specific Resistivity and Hall Effect of Discs of Arbitrary Shapes,”. Philips Res. Repts. 13, 1-9 (1958).

[3] Ultralow resistance, nonalloyed Ohmic contacts to n-InGaAs Baraskar, Ashish K. and Wistey, Mark A. and Jain, Vibhor and Singisetti, Uttam and Burek, Greg and Thibeault, Brian J. and Lee, Yong Ju and Gossard, Arthur C. and Rodwell, Mark J. W., Journal of Vacuum Science and Technology B, 27, 2036-2039 (2009)

[4] A. Baraskar, (Development of Ultra-Low Resistance Ohmic Contacts for InGaAs/InP HBTs.. PhD thesis. University of California, Santa Barbara, Santa. Barbara, Ca, U.S.A., 2011.

[5] Xing, H.; Jena, D.; Rodwell, M.J.W.; Mishra, U.K., ”Explanation of anomalously high current gain observed in GaN based bipolar transistors,” in Electron Device Letters, IEEE , vol.24, no.1, pp.4-6, Jan. 2003

[6] V. Jain, InP DHBTs in a Refractory Emitter Process for THz Electronics.. Ph.D. Thesis, University of California, Santa Barbara, Santa. Barbara, Ca, U.S.A., 2011.

[7] The Alloying of Gold and Gold Alloy Ohmic Contact Metallizations with Gallium Arsenide. Miller, DC, J. Electrochem. Soc. 1980 127(2): 467-475

Chapter 6

Conclusion

6.1 Accomplishments

6.1.1 Improving RF HBT Design and Process

The yield in RF HBTs has been improved by developing and incorporating a low temperature sputtered SiN layer post planarization (Section 3.1). This anchors the high aspect ratio emitter metal and prevents shearing due to BCB expansion in subsequent steps as the sample is heated.

An Iridium base contact process was developed and integrated into the RF HBT process flow. Lower base contact resistivity to p-InGaAs has previously been reported using Ir [1], and it has the added advantage of not sinking in to the semiconductor [2]. An Al_2O_3/SiN composite sidewall was developed for protecting the W/TiW emitter metal during blanket Ir etch in SF_6/Ar. Initial results were successful on test structures. The high power SF_6/Ar etch has low selectivity between Ir and the Al_2O_3/SiN composite sidewall. Thus, the etch

must be calibrated to prevent the emitter metal from being attacked. Tool drift from sample to sample was observed which resulted in the emitter metal being etched on RF HBT runs (Figure 3.3). HfO_2 and ZrO_2 ALD film etch selectivity to SF_6/Ar should be explored as sidewall dielectrics.

HBT epitaxial design was optimized to support maximum emitter current density J_{E} >40mA/μm^2. HBT cutoff frequencies can be increased by increasing emitter current density and thus reducing charging delays in the emitter-base and base-collector junctions. The HBT epi must be designed for a specific collector current density $J_{\mathrm{C,Kirk}}$. Due to collector current spreading, this is empirically found to be half of J_{E} [3]. Recent HBT designs show emitter starvation before Kirk limit is reached [2] and thus the HBT epi structure must be redesigned. The doping in the emitter space charge region has been increased, and its thickness decreased in order to increase the base-emitter voltage at which base-pushout occurs at the emitter-base junction [4].

The base epi design was optimized to reduce Auger recombination while maintaining high doping at the emitter-base junction for low base contact resistivity. Reducing base access resistance R_{bb} is crucial for increasing unity power gain cutoff frequency f_{max} in HBTs. Base doping must be increased to reduce lateral base resistance $R_{\mathrm{b,gap}}, R_{\mathrm{b,spread}}, R_{\mathrm{b,sh}}$ and base contact resistivity $R_{\mathrm{b,cont.}}$ [5]. However, Auger recombination in the base has a quadratic relation to the base doping and must be accounted for in modern RF HBTs where the base doping is $>$ 1x10$^{20}cm^{-3}$ [6]. The base epi design must reduce Auger recombination as well as R_{bb}. Previous base designs with a pulse doping for lower $R_{\mathrm{b,cont.}}$ [3] were modified to a dual doping grade with the minimum doping in the top grade being

$> 1 * 10^{20} cm^{-3}$ to ensure low contact resistivity. The dual grade introduces a quasi-electric field in the heavily doped regions as well, thus reducing base transit time and Auger recombination.

6.1.2 Process Development For $W_{\mathrm{E}} < 100nm$

A new process flow for scaling HBT emitter width (w_{E}) below 100 nm by using ALD metal deposition is proposed and developed. Increasing HBT $f_{\mathrm{t}}, f_{\mathrm{max}}$ requires a decrease in device dimensions and access resistances, and an increase in J_{E}. Reducing w_{E} decreases emitter-base junction capacitance C_{je}, and emitter-base diffusion capacitance C_{diff}. The existing UCSB W/TiW dual refractory emitter metal stack enables w_{E} of 100 nm, but cannot scale further. A new process flow has been developed where a high aspect ratio trench is etched into a sacrificial Si film and is then filled with metal via ALD to form the emitter metal. Si is used as the trench material since high aspect ratio trench processes in Si have been demonstrated [8]. The process requires the trench width and sidewall profile to be vertical for complete ALD metal fill in.

Emitters of $w_{\mathrm{E}} < 70$ nm have been successfully fabricated on test structures using ALD TiN. TiN emitter HBTs suffer from open base-emitter junctions due to interficial oxide formation on TiN. ALD Pt emitters could not be successfully integrated into an HBT process flow as Pt etches in the blanket Si etch after emitter metal deposition. ALD Ru is a viable alternative as it has high electrical conductivity, low contact resistivity to n-InGaAs, can withstand high current density without suffering from electromigration, and does not etch in the blanket Si etch. The UCSB cleanroom has recently acquired an ALD tool capable of

depositing Ru thin films, which enables this.

6.1.3 MOCVD Selective Emitter Regrowth of HBT LADs

A process flow for selective regrowth of the emitter semiconductor has been developed and Large Area Devices (LADs) fabricated. Theoretical calculations for regrowth designs are presented which show an expected increase in DC current gain β and cutoff frequencies. New epi designs are presented for regrowth structures.

β of RF HBTs decreases with decreasing emitter width due to an increase in $\frac{I_{\mathrm{B,edge}}}{I_{\mathrm{B}}}$ and $\frac{I_{\mathrm{B,Auger}}}{I_{\mathrm{B}}}$. A regrown emitter structure allows for a thin, lightly doped intrinsic base which reduces Auger recombination and base transit time to increase β and f_{t} respectively. The extrinsic base can be heavily doped to decrease $R_{\mathrm{b,cont.}}$ and thus increase f_{max}. The extrinsic base also forms a barrier for electrons diffusing towards the base contact which increases β.

MOCVD introduces H^+ at high temperatures which passivates carbon dopants in the p-InGaAs base. H^+ can be removed and the carbon reactivated by annealing the samples in N_2 at 500°C for 10 min. This damages the p-InGaAs surface and leads to prohibitively high base contact resistivity and sheet resistance. InP and W based caps as a means of minimizing surface damage during regrowth and anneal are presented. While in-situ grown InP is an effective regrowth cap, it must be thin enough to be etched away via digital etch and not attack the regrown InP emitter. W is an effective annealing cap, but insufficient as a regrowth cap due to poor growth morphology and InGaAs void formation.

HBT LADs with MOCVD emitter regrowth have been fabricated using SiO_2

and W as a regrowth and anneal cap respectively. They are compared with non-regrowth LADs that were fabricated simultaneously. Maximum β of 28 and 13 was measured on regrowth and non-regrowth devices respectively, for emitters of area 0.8x4 μm^2. Regrowth emitter-base diodes show higher series resistance, thus it is unclear if a higher β in the regrown-emitter HBT is due to lower $I_{\mathrm{B,Auger}}$ in the intrinsic base and lower $I_{\mathrm{B,diff}}$ due to presence of extrinsic-intrinsic base conduction band barrier. β_{bulk} of 96 is extracted for regrown emitter devices.

The current process suffers from low yield due to lateral undercut of W base contact in subsequent process steps. Yield can be improved by using alternate refractory metal contacts such as Ru.

6.2 Future Work

6.2.1 Alternate Base Contact Technologies

Blanket W base contacts as annealing caps have yielded working HBT devices with low $R_{\mathrm{b,cont.}}$ and $R_{\mathrm{b,sh}}$. W acts as a barrier that prevents the InGaAs base elements from diffusing out during the carbon reactivation anneal. However, W is easily etched in subsequent process step chemistries which significantly lowers device yield.

Ruthenium is a promising alternative to W. Low contact resistivity to p-InGaAs using Ru as a contact metal has been demonstrated [1]. It is a refractory metal that does not diffuse at annealing temperatures of >500°C which also makes it an excellent diffusion barrier against InGaAs elements. Moreover, Ru is inert to most chemicals just like the other metals of the Platinum group.

Using Ru as a blanket base metal contact and annealing cap would significantly improve device yield. The blanket metal can be dry etched in the field using Cl_2/O_2 plasma, prior to the base mesa wet etch.
Ru integration into regrowth HBT process flow might present challenges in process steps that require wet etches. Ru is a known versatile catalyst and it's unknown if its presence would lead to any side-effects.

It is also possible to incorporate Pt/Ru blanket base metal contacts that are used in RF HBTs. They retain all the desirable properties of Ru contacts except that the Pt reacts and sinks into the semiconductor. While RF HBTs show a metal sinking depth of ≈3nm [2], the sinking depth after a 500°C anneal is unknown.

6.2.2 Pulse InP Regrowth Cap

Using an in-situ InP cap for protecting the base surface during regrowth is desirable as the p-InGaAs is not exposed till refractory base contact deposition. The base metal can then be used as an annealing cap. A thick InP cap requires a wet etch which also attacks the regrown InP emitter (Section 5.6.3). However, a pulse InP cap (3nm) can be grown insitu, and then digitally etched without attacking the InP emitter. This was not possible as existing RF HBT epi was used to test the MOCVD emitter regrowth process. However, an epi designed for regrowth can incorporate this feature which significantly reduces base surface damage. No side-effects to this integration are expected.

6.2.3 Epitaxial Design For Emitter Regrowth

As mentioned in 5.3, the HBT epi used for MOCVD emitter regrowth was initially designed for RF HBTs at the 100 nm emitter node. The emitter semiconductor was blanket wet etched away before deposition of the oxide regrowth mask for emitter regrowth. This approach increased base surface damage due to the oxide regrowth cap. The extrinsic base thickness was arbitrarily designed based on digital etch thickness and it could not be made thicker without increasing intrinsic base sheet resistance. Moreover, there was no doping step between the intrinsic and extrinsic base that would create a diffusion barrier. The doping grade in the base however generates a quasi-electric field that also inhibits electron diffusion to the base contacts.

The focus of this work was to show feasibility of fabricating HBTs using MOCVD selective emitter regrowth. HBT epi must be designed explicitly for regrowth to demonstrate an increase in β and cutoff frequencies. Key new features of a regrowth structure include a pulse InP cap above the base, doping step at the extrinsic-intrinsic base boundary, thicker heavily doped extrinsic base, and thinner lightly doped intrinsic base. The pulse InP cap reduces surface damage and is discussed in 6.2.2. The doping step in the base induces a diffusion barrier for electrons diffusing towards the base contact metal. A thicker and highly doped extrinsic base allows for base metal sinking without affecting $R_{\mathrm{b,cont}}$. Moreover, the extrinsic base surface can now be digitally etched to remove damaged layers before depositing metal contacts. Since the entire extrinsic base is heavily doped, low $R_{\mathrm{b,cont}}$ is maintained. A sample epi design is shown in Table 6.1.

Layer	Semiconductor	Thickness (Å)	Doping (cm^{-3})
Regrown Emitter cap	$In_{0.53}Ga_{0.47}As$	100	8×10^{19}:Si
Regrown Emitter	InP	150	5×10^{19}:Si
Regrown Emitter	InP	150	3×10^{18}:Si
Extrinsic Base cap	InP	30	14×10^{19}:C
Extrinsic Base	$In_{0.53}Ga_{0.47}As$	80	14×10^{19}:C
Intrinsic Base	$In_{0.53}Ga_{0.47}As$	120	$9 - 5 \times 10^{19}$:C
Setback	$In_{0.53}Ga_{0.47}As$	50	1×10^{17}:Si
B-C grade	-	120	1×10^{17}:Si
δ-doping	InP	30	6×10^{18}:Si
Collector	InP	500	1×10^{17}:Si
Sub-collector	InP	75	2×10^{19}:Si
Sub-collector	$In_{0.53}Ga_{0.47}As$	75	4×10^{19}:Si
Sub-collector	InP	3000	1×10^{19}:Si
Etch stop	$In_{0.53}Ga_{0.47}As$	35	undoped
Substrate	InP	-	undoped

Table 6.1: Proposed epitaxial structure of RF HBT with emitter regrowth. The emitter-base junction is formed at the emitter-intrinsic base interface, and the extrinsic base lies on either side of this junction, on top of the intrinsic base.

6.2.4 Scaling HBTs for RF Performance

LADs were fabricated for rapid prototyping and troubleshooting of the regrowth process flow. This was crucial for evaluating the feasibility of a MOCVD emitter regrowth based HBT technology.

It has been shown that working HBTs can be fabricated using MOCVD emitter regrowth, but it is yet to be demonstrated if they yield higher β and cutoff frequency when compared with traditional HBT structures. Comparing device performance of regrowth and non-regrowth devices at $w_{\mathrm{E}} \leq$100 nm is crucial for establishing the advantages of emitter regrowth over traditional HBT devices. Regrown emitter HBTs with self-aligned emitter metal can be fabricated using the ALD emitter technology presented in 4.6. Device scaling requires a redesign of the epi structure as discussed in sections 6.2.2, and 6.2.3.

References

[1] A. Baraskar, (Development of Ultra-Low Resistance Ohmic Contacts for InGaAs/InP HBTs.. PhD thesis. University of California, Santa Barbara, Santa. Barbara, Ca, U.S.A., 2011.

[2] J. Rode, IC Fabrication Technology for Highly Scaled THz DHBTs.. Ph.D. Thesis, University of California, Santa Barbara, Santa. Barbara, Ca, U.S.A., 2015.

[3] V. Jain, InP DHBTs in a Refractory Emitter Process for THz Electronics.. Ph.D. Thesis, University of California, Santa Barbara, Santa. Barbara, Ca, U.S.A., 2011.

[4] Jain, V.; Rodwell, Mark J.W., "Transconductance Degradation in Near-THz InP Double-Heterojunction Bipolar Transistors," in Electron Device Letters, IEEE , vol.32, no.8, pp.1068-1070, Aug. 2011. doi: 10.1109/LED.2011.2157451

[5] Rodwell, Mark J.W.; Urteaga, M.; Mathew, T.; Scott, D.; Mensa, Dino; Lee, Q.; Guthrie, J.; Betser, Y.; Martin, S.C.; Smith, R.P.; Jaganathan, S.; Krishnan, S.; Long, S.I.; Pullela, R.; Agarwal, B.; Bhattacharya, U.; Samoska, L.; Dahlstrom, M., "Submicron scaling of HBTs," in Electron Devices, IEEE Transactions on , vol.48, no.11, pp.2606-2624, Nov 2001

[6] H. Chiang, Design and Fabrication of Sub-100nm Base-Emitter Junctions of THz InP DHBTs.. Ph.D. Thesis, University of California, Santa Barbara, Santa Barbara, Ca, U.S.A., 2014...

[7] . Lateral carrier diffusion and current gain in terahertz InGaAs/InP double-heterojunction bipolar transistors. Chiang, Han-Wei and Rode, Johann C. and Choudhary, Prateek and Rodwell, Mark J. W., Journal of Applied Physics, 115, 034513 (2014)

[8] Sub-50 nm high aspect ratio silicon pillars, ridges, and trenches fabricated using ultrahigh resolution electron beam lithography and reactive ion etching. Fischer, P. B. and Chou, S. Y., Applied Physics Letters, 62, 1414-1416 (1993)

Appendix A

HBT 64 Equivalent Circuit Model

This section shows the epitaxial structure (Table A.1) and equivalent circuit model (Figure A.1) for HBT 64C that was fabricated at UCSB [1] [2]. The device has an emitter area $A_{\mathrm{E}} = 0.22 \times 2.9 \mu m$, and a peak $f_{\mathrm{t}}/f_{\mathrm{max}}$ of 480/910 GHz measured at V_{CE}=1.85 V, J_{E}= 18 mA/μm^2, and $V_{\mathrm{CB}} = 0.98$ V.

Layer	Semiconductor	Thickness (Å)	Doping (cm^{-3})
Emitter cap	$In_{0.53}Ga_{0.47}As$	100	8×10^{19}:Si
Emitter	InP	150	5×10^{19}:Si
Emitter	InP	150	5×10^{18}:Si
Base	$In_{0.53}Ga_{0.47}As$	200	$11 - 7 \times 10^{19}$:C
Setback	$In_{0.53}Ga_{0.47}As$	135	5×10^{16}:Si
B-C grade	-	165	5×10^{16}:Si
δ-doping	InP	30	3.6×10^{18}:Si
Collector	InP	670	5×10^{16}:Si
Sub-collector	InP	75	2×10^{19}:Si
Sub-collector	$In_{0.53}Ga_{0.47}As$	75	4×10^{19}:Si
Sub-collector	InP	3000	1×10^{19}:Si
Etch stop	$In_{0.53}Ga_{0.47}As$	35	undoped
Substrate	InP	-	undoped

Table A.1: Epitaxial structure of HBT 64.

RC values /μm^2 from A.1 were used as a reference for estimating gains in $f_{\mathrm{t}}/f_{\mathrm{max}}$ in regrown-emitter HBTs for multiple base designs (Section 4.4.

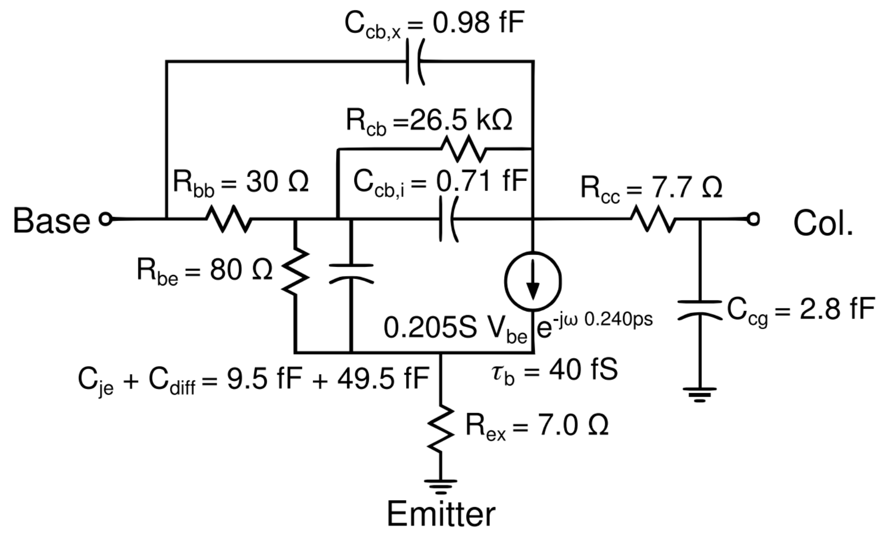

Figure A.1: Equivalent circuit model of HBT 64C. $A_{\mathrm{E}} = 0.22 \times 2.9\ \mu m^2$

References

[1] J. Rode, IC Fabrication Technology for Highly Scaled THz DHBTs.. Ph.D. Thesis, University of California, Santa Barbara, Santa. Barbara, Ca, U.S.A., 2015.

[2] Rode, J.C.; Chiang, H.-W.; Choudhary, P.; Jain, V.; Thibeault, B.J.; Mitchell, W.J.; Rodwell, M.J.W.; Urteaga, M.; Loubychev, D.; Snyder, A.; Wu, Y.; Fastenau, J.M.; Liu, A.W.K., "An InGaAs/InP DHBT With Simultaneous f_t/f_{max} 404/901 GHz and 4.3 V Breakdown Voltage," in Electron Devices Society, IEEE Journal of the , vol.3, no.1, pp.54-57, Jan. 2015

Appendix B

UCSB W/TiW Emitter Metal Process

This sections lists the process flow for the blanket sputtered W/TiW dry etch emitter process developed [1] [2] and optimized [3] [4] at UCSB, for InP/InGaAs HBTs of emitter width ≥100 nm. Figure B.1 shows the process flow.

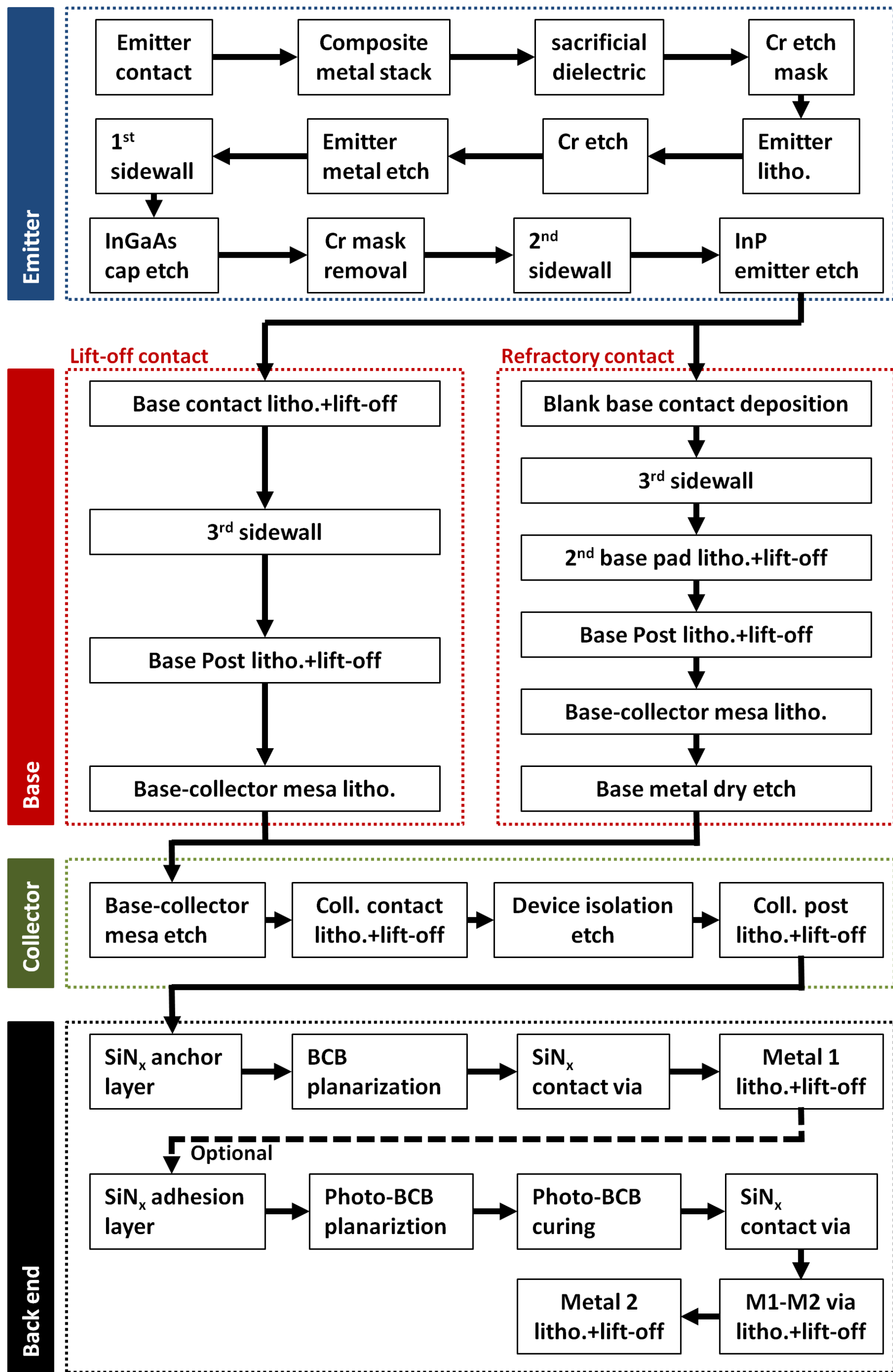

Figure B.1: Flow chart for HBT fabrication with blanket W/TiW emitter process [3]

References

[1] V. Jain, InP DHBTs in a Refractory Emitter Process for THz Electronics.. Ph.D. Thesis, University of California, Santa Barbara, Santa. Barbara, Ca, U.S.A., 2011.

[2] E. Lobisser, Scaling Mesa InP DHBTs to Record Bandwidths.. Ph.D. Thesis, University of California, Santa Barbara, Santa. Barbara, Ca, U.S.A., 2011.

[3] H. Chiang, Design and Fabrication of Sub-100nm Base-Emitter Junctions of THz InP DHBTs.. Ph.D. Thesis, University of California, Santa Barbara, Santa Barbara, Ca, U.S.A., 2014

[4] J. Rode, IC Fabrication Technology for Highly Scaled THz DHBTs.. Ph.D. Thesis, University of California, Santa Barbara, Santa. Barbara, Ca, U.S.A., 2015.